Determination of Capacities of Eccentric Stiffeners Part 1: Experimental Studies

JAVIER ALVAREZ RODILLA and KEITH KOWALKOWSKI

ABSTRACT

Forty column specimens were experimentally tested with an effort to identify the effective stiffener capacities of eccentric stiffeners when used within moment connections of beams connecting to column flanges. Three test methods were performed described as (1) single tension with load pulling away from the column specimen, (2) single compression with load applied toward the column specimen, and (3) double compression with load applied toward the column specimen and with a reaction plate directly opposite from the applied load. The sizes were selected with a range of slenderness ratios for the web and flange and to study multiple concentrated load limit states using AISC *Specification* Section J10 (AISC, 2016b). For each column size and test method, four column specimens were tested: (1) without stiffeners, (2) with stiffeners concentric with the applied load, (3) with stiffeners at a low eccentricity of 2 in. or 3 in., and (4) with stiffeners at a high eccentricity of 4 in. or 6 in.

For column specimens tested without stiffeners and for compression tests, the maximum loads compared favorably to those predicted for web local crippling and were significantly higher than those predicted for web compression buckling (double compression tests) and web local yielding. For single tension tests, the maximum load always exceeded that predicted for the limit states of flange bending and web local yielding.

KEYWORDS: eccentric stiffeners, moment connections, concentrated loads, flange bending, web compression buckling, web local crippling, web local yielding.

INTRODUCTION

A comprehensive research project was performed at Lawrence Technological University (LTU) to evaluate the influence of stiffener eccentricity on the effective resistance of column members when subjected to concentrated loads that develop from moment connections. The study can be extended for the design of stiffeners for other scenarios when wide-flange beams are subjected to concentrated loads. Forty column specimens were experimentally tested under concentrated loads. The concentrated load simulated either an attached component in tension or an attached component in compression. The column specimens were notably smaller than column sizes that are used in practice due to limitations in the maximum loads that could be obtained by hydraulic actuators. However, the results of the experimental investigations were later utilized to calibrate/verify finite element models. Finite element models were then developed for more "practical" column sizes. This paper discusses the experimental investigations only, while the discussion of the finite element models is presented in Part 2: Analytical Studies (Alvarez Rodilla and Kowalkowski, 2021).

When concentrated loads are applied to column flanges at moment connections, capacities for different "limit states" are calculated to determine the resistance of the column section to the concentrated loads. Different limit states are considered if (1) a single compression force is applied to one flange; (2) a single tension force is applied to one flange; and (3) a double compression force is applied to both flanges simultaneously and the force on each side is directly opposite to each other, creating a through force. Tension or compression force refers to whether the component connected, such as a plate or beam flange, is subjected to a tensile or compressive axial force. Columns may also be subjected to a tension force on both flanges simultaneously or subjected to a compression force on one flange and a tension force on the other flange. However, there are no specific limit states associated with these two combined loading conditions, and individual forces on one flange can be treated as either single tension or single compression forces. Therefore, the three conditions analyzed in this research were single tension, single compression, and double compression. The limit states that define resistance of a steel member to concentrated loads and those applicable for the design of transverse stiffeners are summarized as follows (AISC, 2016b):

- Web local yielding—Limit state applies for all loading

Javier Alvarez Rodilla, EIT, Graduate Research Scholar, Lawrence Technological University, Southfield, Mich. E-mail: jalvarezr@ltu.edu

Keith Kowalkowski, PhD, PE, SE, Associate Professor, Lawrence Technological University, Southfield, Mich. E-mail: kkowalkow@ltu.edu (corresponding)

Paper No. 2019-16R(1)

conditions, tension or compression, and at each loaded location on the flanges.

- Flange bending—Limit state applies when a concentrated tension force is applied to the flange and across the width of the flange (usually the case for moment connections).
- Web local crippling—Limit state applies when a single- or double-concentrated compression force is applied to the flange(s).
- Web compression buckling—Limit state applies when a double compression force is applied to both flanges simultaneously, causing a through-compression force.

In the event that the calculated applied force (demand) from the moment connection exceeds the capacity per the preceding limit states, stiffener plates and/or doubler plates are utilized to reinforce the column section. Usually, the use of stiffener plates is preferred, but in some cases, interferences exist that disallow the stiffener plates to be concentric with the applied force. Instead, the stiffeners are detailed and utilized at an eccentricity with respect to the location of the concentrated force.

Limited experimental studies have been performed to evaluate the influence of stiffener eccentricity and the effective resistance of column sections to concentrated loads. This paper evaluates the "effective stiffener capacity," which is defined as the difference between test capacities for column specimens with stiffeners, both concentric and eccentric, and test capacities for the corresponding column specimens without stiffeners and subjected to the same loading condition.

BACKGROUND

When concentrated loads are applied perpendicular to a column flange, several concentrated load limit states are checked to avoid local failure mechanisms per Sections J10.1, J10.2, J10.3, and J10.5 of the AISC *Specification for Structural Steel Buildings* (AISC, 2016b), hereafter referred to as the AISC *Specification*. If the capacity of any of these limit states is less than the computed concentrated force, AISC permits the use of full-depth transverse stiffeners to partially resist the concentrated force. The lowest applicable capacity for the concentrated load limit states is used to define the member capacity. The required stiffener capacity is equal to the applied concentrated load minus the member capacity. In accordance with AISC *Specification* Section J10.8, stiffeners are designed as part of the connections and considered as tension or compression members.

Eccentric stiffeners refer to that fabricated in the column section at an offset from the beam flange or flange plate. Examples of concentric and eccentric stiffener conditions are shown in Figure 1. Figure 1(a) demonstrates a condition where stiffeners are concentric, while Figure 1(b) shows an eccentric stiffener scenario where one beam flange is offset from the stiffener.

Figure 1 shows one example of the utilization of eccentric stiffeners, but in general, they may be required due to the presence of multiple connections framing into the joint or other cases that would create interferences within the column boundaries. Common cases that occur in practice when multiple plates are theoretically required at slightly different elevations include:

- When beams are moment connected to both column flanges but are of different depths and calculations mandate, stiffeners are required for the concentrated loads being applied to both flanges (as in Figure 1).
- When beams are moment connected to both column flanges but the top of steel elevation is different on both sides and calculations mandate, stiffeners are required for the concentrated loads being applied on both sides.
- When the location of a stiffener for a moment connection to a column flange would interfere with a flange plate designed as part of a connection where a beam frames into a column web.

In all three cases, concentric stiffeners may not be feasible due to clearance for welding that must occur at each stiffener. In addition, it may not be necessary to have each stiffener if other stiffeners are close to the proximity of the concentrated load; this "acceptable" eccentricity is one of the key focuses of this research project.

Although the AISC *Specification* provides some guidance for the design of transverse stiffeners, there is no assistance associated with tolerances or design with eccentric stiffeners. The only source available from AISC for the design of eccentric column stiffeners or alternate methods to reinforce columns is AISC Design Guide 13, *Stiffening of Wide-Flange Columns at Moment Connections: Wind and Seismic Applications* (Carter, 1999). More specifically, Design Guide 13, Section 5.1, discusses options for column stiffening for beams of differing depth and/or top of steel. The Design Guide shows multiple options if the beam flanges on opposite sides of the columns are at different elevations, such as the use of partial depth stiffeners or sloping stiffeners. A final option discussed in the Design Guide is the use of one transverse stiffener that is aligned with one beam flange and not the other or to provide one transverse stiffener in between the two beam flanges. In either case, this creates a design eccentricity e as shown in Figure 2.

Research performed by Graham et al. (1959) showed that transverse stiffeners with a 2-in. eccentricity provides 65% of the strength of an identical transverse stiffener that is noneccentric. In addition, it was recommended, "…for design purposes, it would probably be advisable to neglect

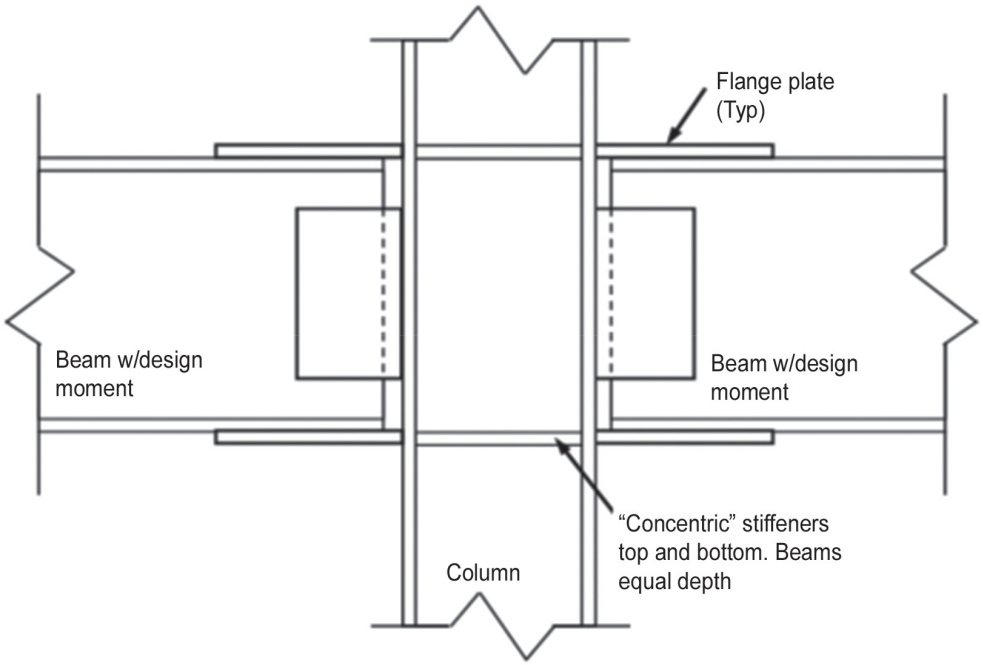

(a) Concentric stiffener condition

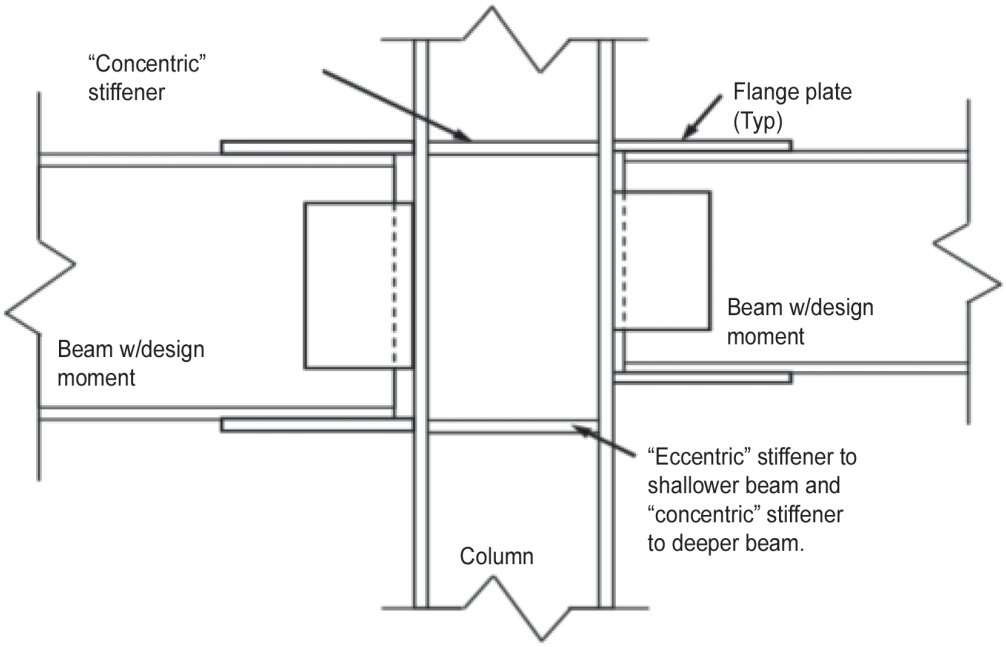

(b) Eccentric stiffener condition

Fig. 1. Example of concentric stiffeners vs. eccentric stiffeners.

the resistance of stiffeners having eccentricity greater than 2 in. The required transverse stiffener area, width and thickness can be established by the same criteria as for concentric stiffeners, provided that the strength is reduced linearly from 100 percent at zero eccentricity to 65 percent at 2 in. eccentricity."

Further research on concentrated loads in wide-flange sections was performed by Sherbourne and Murthy (1978). This research focused on analyzing the stability of column webs in beam-column moment connections. Sherbourne and Murthy carried out analytical tests on wide-flange sections with concentric and eccentric stiffeners. Eccentric stiffeners were placed at 25% and 50% of half the column depth. The results showed that the relative load capacity of eccentric stiffeners decreased dramatically compared to the specimens with concentric stiffeners in any event, regardless of the column's flange or web thicknesses. For the first test series with stiffeners at lower eccentricities, the effectiveness of the stiffeners ranged between 50% and 75% of that for concentric stiffeners. Sherbourne and Murthy also found that the web thickness has a direct influence on the buckling load and behavior.

Norwood (2018) performed analytical research on wide-flange sections similar to the experimental tests carried out by Graham et al. (1959). Similar to previous research, Norwood found that increasing the level of eccentricity between the flange and the transverse stiffener results in a decrease in resistance to concentrated forces. The results showed that eccentric stiffeners were more effective in comparison to the recommendations given by Graham et al.

The limitation of a 2-in. eccentricity has been problematic in design. Further, verbal communication with representatives of the steel industry indicates that fabricators and designers have utilized stiffeners at higher eccentricities, regardless of the lack of design standards for such cases. The results presented in this research project are intended to provide further clarity and expand the recommendations presented in Carter (1999). The project investigates eccentricities higher than 2 in. and, more importantly, evaluates a wider range of column sizes and loading conditions in comparison to the work performed by Graham et al. (1959).

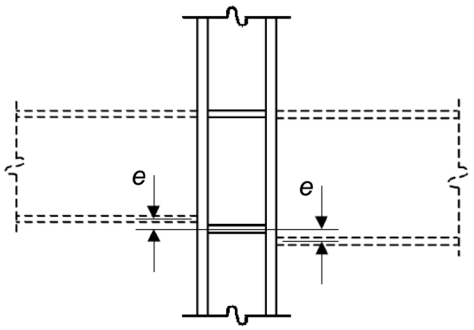

Fig. 2. Stiffener option at eccentricity e *per AISC Design Guide 13 (Carter, 1999).*

EXPERIMENTAL RESEARCH PROJECT

Forty "column" specimens (the test setup is described later) were subjected to concentrated loads at mid-length (center of beam with respect to longitudinal axis). Four different cross-section sizes were tested: W10×19, W10×39, W12×26, and W16×31. For single compression tests, all four sizes were tested. For double compression tests and single tension tests, three of the four sizes were tested (all except W10×19 for single tension and W10×39 for double compression). For each test type and each section size, the following four tests were performed and will be further referred to as the "test group":

1. One test was performed without any stiffeners at mid-length to establish a baseline capacity prior to the addition of any stiffeners.
2. One test was performed with stiffeners directly concentric with the concentrated load and, therefore, with an eccentricity of 0 in.
3. One test was performed with stiffeners at a high eccentricity from the concentrated load. For the W16×31 column specimens, high eccentricity was equal to 6 in.; for other column specimens, the high eccentricity was equal to 4 in.
4. One test was performed with stiffeners at a low eccentricity from the concentrated load. For the W16×31 column specimens, the low eccentricity was equal to 3 in.; for other column specimens, the low eccentricity was equal to 2 in.

It is important to note why the "high eccentricity" and "low eccentricity" magnitudes are different for some column specimens. Initially, an objective was to identify the effective stiffener capacities of eccentric stiffeners as a percentage of the effective stiffener capacity of concentric stiffeners up to a maximum eccentricity of 6 in. Initial tests on W16×31 column specimens demonstrated no difference in the maximum load without stiffeners and when stiffeners were used at a high eccentricity of 6 in. and therefore, the low and high eccentricities were changed to 2 in. and 4 in., respectively, prior to installing stiffeners into other column sections.

TEST MATRIX

Table 1 shows an abbreviated experimental test matrix. Three factors were considered in selecting the column specimen sizes for the experimental test matrix:

Table 1. Test Matrix for Experimental Column Specimens				
Member	Test Method	$b_f/2t_f$	h/t_w	Predicted Failure Mode without Stiffeners Using Nominal Capacities
W16×31	Single compression	6.28	51.6	Web local yielding
W12×26	Single compression	8.54	47.2	Web local yielding
W10×39	Single compression	7.53	25.0	Web local yielding
W10×19	Single compression	5.09	35.4	Web local yielding
W16×31	Double compression	6.28	51.6	Web compression buckling
W12×26	Double compression	8.54	47.2	Web compression buckling
W10×19	Double compression	5.09	35.4	Web compression buckling
W16×31	Single tension	6.28	51.6	Flange bending
W12×26	Single tension	8.54	47.2	Flange bending
W10×39	Single tension	7.53	25.0	Flange bending

1. Member sizes were selected for single compression testing, double compression testing, and single tension testing such that the capacity of the hydraulic actuator would not be exceeded prior to failure, with and without stiffeners.
2. A proportioning study was performed to relate the geometry of smaller shapes to the geometry of larger shapes utilizing the slenderness ratios of the flange and web. Three different ranges were considered for the flange slenderness (defined as the $b_f/2t_f$ ratio), and three different ranges were considered for the web slenderness (defined as the h/t_w ratio). The ranges included approximately the same number of wide-flange members. More information can be found in Kowalkowski and Alvarez Rodilla (2019).
3. Member sizes were selected to have a variation in the predicted limit state that defines capacity under concentrated loads. These limit states include web local yielding, web compression buckling, and flange bending (AISC, 2016b). Nominal capacities were used for this study as shown in Table 1.

The nomenclature used for each column specimen, as shown with the results presented later, includes the column specimen size, the test method, and the stiffener condition. For the test method, DC refers to double compression, SC refers to single compression, and ST refers to single tension. For the stiffener condition, NA indicates a test without stiffeners. E2 refers to a column specimen with stiffeners at an eccentricity of 2 in. A similar designation is utilized for other magnitudes of eccentricity.

TEST SETUP

All experimental testing was performed in the Structural Testing Center at Lawrence Technological University in Southfield, Michigan, using a high-capacity load frame and hydraulic actuator. The hydraulic actuator had a capacity of 220 kips for a downward force (compression) and a capacity of 145 kips for an upward force (tension). Therefore, the capacity for tension was lower than the capacity for compression. This fact was unknown until the experimental testing stage progressed, which led to some tension specimens unexpectedly reaching the actuator capacity without any mode of failure.

Photographs of the experimental test setups are provided in this section. Full schematics are provided with dimensioning, plate, and weld sizes in Kowalkowski and Alvarez Rodilla (2019).

Figure 3 shows a photograph of the test setup used for single compression tests. The column specimens were simply supported at 5 ft, and load was applied using a ¾-in. loading plate fabricated from ASTM A36 steel. Lateral supports were utilized at each end to avoid lateral translation of the top flange and twisting of the column specimen. Figure 3 identifies the location of paint/spackle used for digital image correlation (DIC). This instrumentation will be discussed later in this paper.

The double compression setup was the same as the single compression setup but with an additional ¾-in. reaction plate located directly below the column specimen and in line with the applied load. The reaction plate was part of a fixture, similar to the fixture that is attached to the hydraulic actuator. The reaction plate and fixture were supported

on a built-up support frame that was supported by the concrete floor. Figure 4 shows a photograph of the test setup used for the double compression tests.

The test setup for single tension specimens included a specially designed reaction frame that was attached to the existing steel frame as shown in Figure 5. The reaction frame consisted of W10×68 posts, W10×68 spreader beams, HSS bracing, plates and bolts. The test setup was designed to allow force to be applied upward without fabricating new post-tensioning holes in the concrete strong floor. Unlike the compression tests, the loading plate was welded to the top flange of the column specimen. This detail is discussed more in the next section. The loading plate was bolted to two vertical plates simulating double shear in the bolts. The bottom flanges of the column specimens were laterally supported to prevent lateral translation and twisting of the column specimens under loading. Additional details of the test setups are provided in Kowalkowski and Alvarez Rodilla (2019).

COLUMN SPECIMENS

Column specimens were 6 ft long and fabricated from ASTM A992 steel. Uniaxial tension tests were performed according to the requirements of ASTM E8/E8M-09 (ASTM, 2009) on coupons fabricated from the column specimens, which confirmed that the yield stress was approximately 55 ksi for all column specimen sizes. All coupons were taken from the web and/or flange of the column specimen, away from mid-length.

Near mid-length and when applicable, stiffeners were located on both sides of the web with a total depth equal to the depth between column flanges minus 1/16 in. For W10×39, W12×26, and W16×31 column specimens, all stiffeners were 3/8 in. and welded using 1/4-in. fillet welds. For W10×19 column specimens, all stiffeners were 1/4 in. and welded using 3/16-in. fillet welds. The depth of the stiffeners extended to the edges of the flange to the nearest 1/16 in. At the fillet radius between web and flange, 1/2-in. corner clips were fabricated. For all stiffeners at mid-length, welding was performed using flux-core arc welding (FCAW). The stiffener plates were specified to be A36 steel. However, when delivered, it was revealed that some stiffeners met the specifications for A36 and A572 Gr. 50 and were, therefore, dual certified.

Bearing stiffeners were used for most tests at the supports to ensure concentrated load failure mechanisms were not developed at the support reactions. The stiffeners were of the same dimensions as the mid-length stiffeners. The bearing stiffeners were fillet welded to both flanges and web of the cross-section; however, FCAW was not used. For

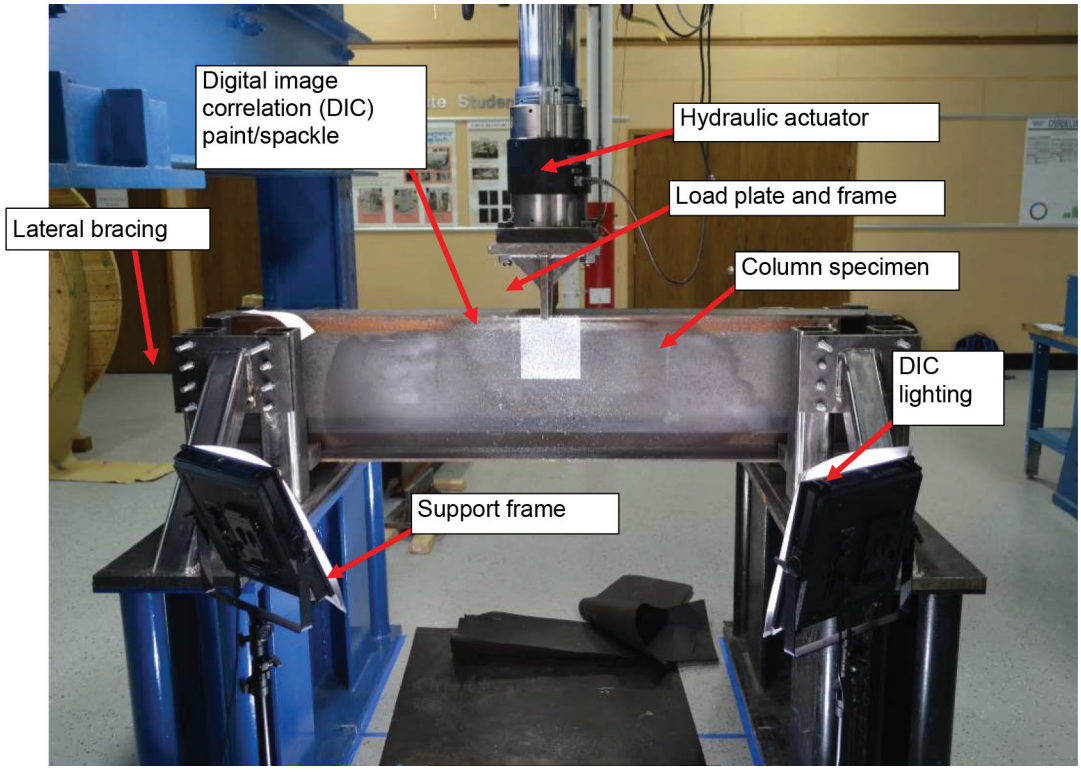

Fig. 3. Single compression test setup.

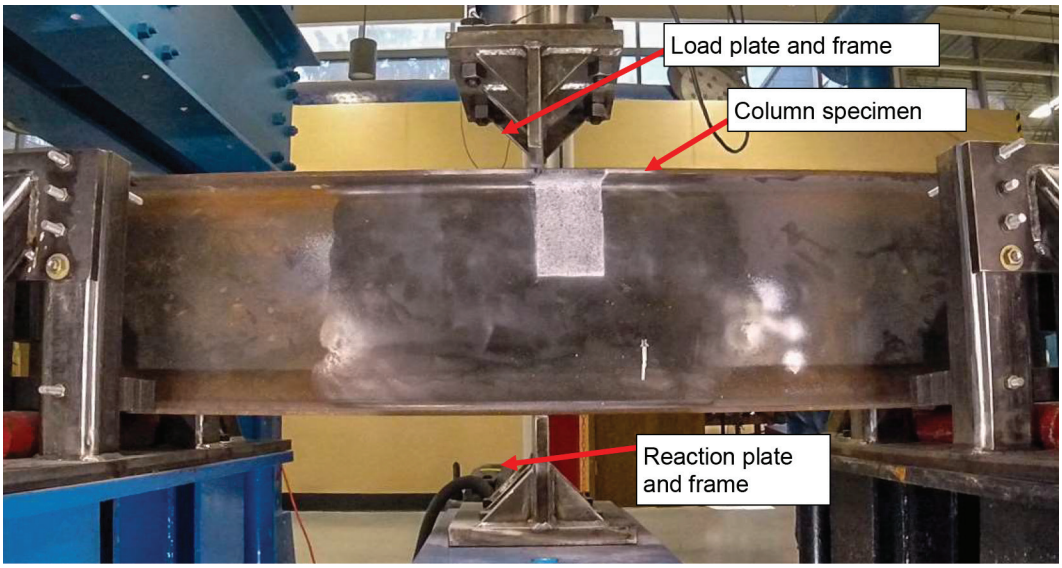

Fig. 4. Double compression test setup.

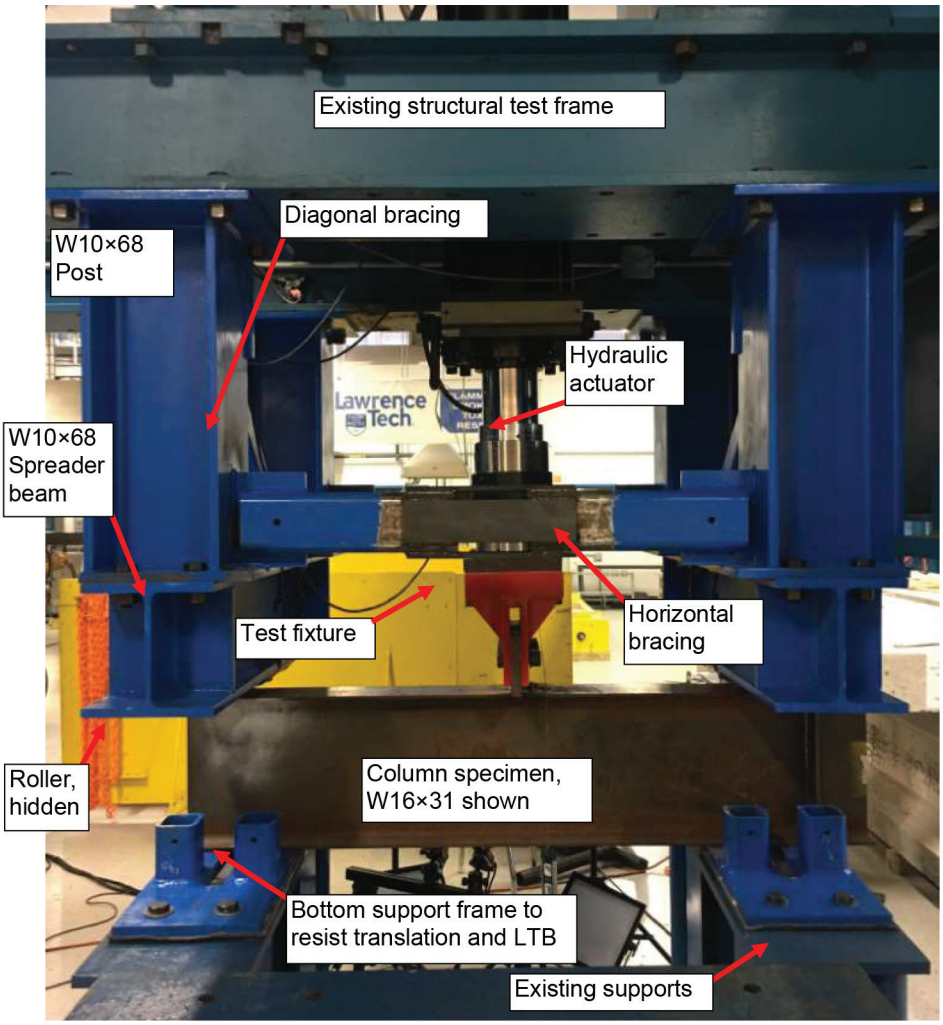

Fig. 5. Single tension test setup.

double compression tests, no bearing stiffeners were used because all the load was assumed to pass through the web to bottom support reaction.

Column specimens for single tension tests were welded to a ⅞-in. loading plate made from A36 steel, which was bolted to two plates of the test setup as discussed in the previous section. The loading plates were attached to the column specimens using ⅜-in. fillet welds on both sides using the FCAW process. Figure 6 shows a photograph of the W10×39 ST-E2 column specimen prior to testing.

INTRUMENTATION AND EXPERIMENTAL PROCEDURE

The hydraulic actuator was equipped with a load cell that measured the applied load during testing. In addition, the actuator stroke displacement was tracked and recorded. Additional instrumentation to capture strain and displacements under the applied load was used. Digital image correlation (DIC), which is an optical method that employs tracking and image registration techniques for accurate two-dimensional and three-dimensional measurements of changes in images, was used as the primary source of instrumentation. DIC is capable of developing a three-dimensional strain and displacement state and was utilized to evaluate local deformations and stresses, along with the mode of failure. A localized area of the column's web and flange and the interior stiffener face, if applicable, were prepped for DIC as discussed in Kowalkowski and Alvarez Rodilla (2019). Figure 3 identified the localized area on a column specimen without stiffeners that was painted/spackled for DIC.

Figure 7 demonstrates DIC results for the W12×26 SC-E4 column specimen at a load of 78 kips. The load of 78 kips corresponds to the maximum load obtained for the equivalent column section without stiffeners. In this example, strain is shown for the *y*-direction, which corresponds to the direction of the applied load. The blue and green represent areas of high negative (compression) strain. Figure 7 shows that for this specimen, the concentrated load is spread into the column section in a very localized area under the applied load away from the eccentric stiffener. This negligible influence of eccentric stiffeners in resisting concentrated loads was a common trend in specimens with eccentric stiffeners as described in later sections.

All tests, tension or compression, were performed in displacement control with a loading rate of 0.05 in./min. For most compression tests, the experiment was considered complete when a maximum load was obtained and the load started to decrease significantly with an increase in vertical displacement. A decrease in load indicated that a buckling failure mechanism had occurred. Common failure modes in compression tests are best described as web local crippling and stiffener buckling. The test was allowed to continue until a failure mechanism was visibly apparent.

The test procedure for the single tension tests was similar to the test procedure used for the compression tests. The column specimens were attached to the top test fixture using bolts, and the column specimen had to be raised into contact with the top rollers (see Figure 5) prior to initiating the test. The single tension tests were considered complete when one of the two events occurred: (1) the actuator capacity was reached or (2) the weld between the loading plate and column specimen failed. Weld failure generally occurred for column specimens without stiffeners and when eccentric stiffeners were used. During one single tension test, rupture occurred in the web of the column specimen directly beneath the loading plate. For all three column specimen sizes, the capacity of the actuator was reached when concentric stiffeners were used. In addition, for all W10×39 column specimens, the capacity of the hydraulic actuator was reached prior to another failure occurring. Reasons for why the actuator capacity was not sufficient in these tests are described in Kowalkowski and Alvarez Rodilla (2019). This result was not desired, but the DIC results were utilized to evaluate experimental behavior for different stiffener conditions prior to reaching the capacity of the hydraulic actuator.

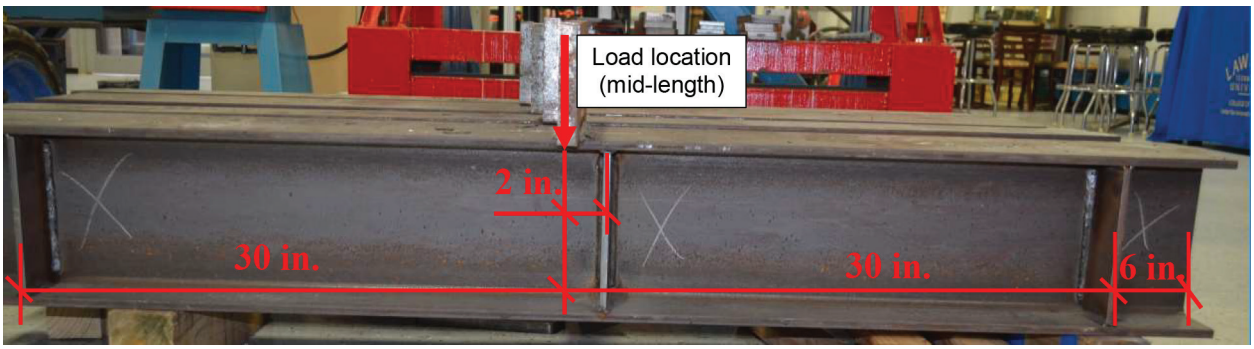

Fig. 6. Photograph of W10×39-ST-E2 (eccentricity = 2 in.) prior to testing.

ANTICIPATED FAILURE MECHANISMS

Table 1 listed the anticipated failure mechanisms or limit states for column specimens when no stiffeners were used near the location of the concentrated loads. In this research, it is crucial to understand how the stiffeners either share loading or stiffen the web, preventing the web's ability to buckle or cripple. Therefore, for each test method, a particular limit state was evaluated, and column sizes were selected to ensure that the particular limit state controlled for the applicable test method. When nominal strengths are calculated (i.e., without ϕ or Ω factors per LRFD or ASD, respectively), the limit state of web local crippling never controls for any standard wide-flange member when load is applied away from the end of the member. As shown later in this report, most columns subjected to either single compression or double compression reached their actual capacity when web local crippling occurred. However, web yielding was identified during the tests. After initial yielding, the load continues to increase until a buckling limit state is reached; after which the load starts to decrease rapidly.

Strengths were calculated using AISC *Specification* Section J10 (AISC, 2016b) using an expected yield strength of 55 ksi from the AISC *Seismic Provisions for Structural Steel Buildings* (AISC, 2016a). Flange bending is given by Equation 1 and is only applicable in design for single tension tests. Web local yielding is given by Equation 2 and is applicable for all test methods. Web local crippling is given by Equation 3 and is applicable for all compression tests. Web compression buckling is given by Equation 4 and is applicable only for double compression tests. For Equations 1–4, the first equation number corresponds to the respective equation in the AISC *Specification* (AISC, 2016b).

$$R_n = 6.25F_{yf}t_f^2 \quad \text{(from AISC } Spec. \text{ Eq. J10-1)} \quad (1)$$

$$R_n = 1.0(5k + l_b)F_y t_w \quad \text{(from AISC } Spec. \text{ Eq. J10-2)} \quad (2)$$

$$R_n = 0.80t_w^2\left[1 + 3\left(\frac{l_b}{d}\right)\left(\frac{t_w}{t_f}\right)^{1.5}\right]\sqrt{\frac{EF_y t_f}{t_w}} \quad \text{(from AISC } Spec. \text{ Eq. J10-4)} \quad (3)$$

$$R_n = \frac{24t_w^3\sqrt{EF_y}}{h} \quad \text{(from AISC } Spec. \text{ Eq. J10-8)} \quad (4)$$

where

F_y = expected yield strength = 55 ksi
d = overall depth of section, in.
h = depth of web between fillets = $d - 2k$, in.
l_b = bearing length, in this research is equal to thickness of loading plate, in.
k = depth from face of flange to edge of fillet, in.
t_f = thickness of flange, in.
t_w = thickness of web, in.

EXPERIMENTAL RESULTS

The discussion of the experimental results is separated by test method. Detailed discussion focuses on W12×26 column specimens for compression tests and W16×31 column specimens for the single tension tests. The results of all experimental testing are best described and represented utilizing the results of these column specimen sizes and the corresponding test methods. All experimental results for all column specimens are provided in Kowalkowski and Alvarez Rodilla (2019). For each test, load-displacement relationships were plotted and the four tests of the "test

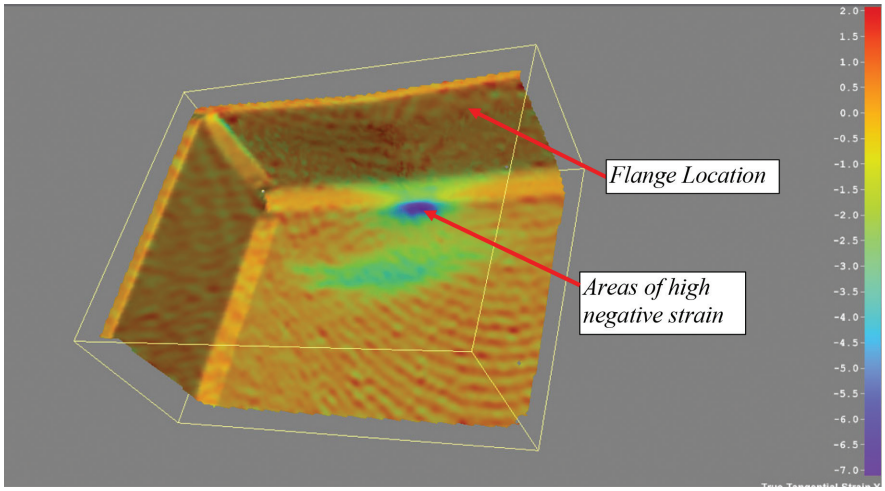

Fig. 7. DIC results; vertical strain for W12×26 SC-E4 column specimen at 78.2 kips.

group" were plotted together (one without stiffeners, one with concentric stiffeners, and two with eccentric stiffeners) to further evaluate the influence of eccentric stiffeners. The hydraulic actuator's load cell measurement for load and the actuator's stoke displacement were used to develop the load-displacement relationships. When applicable, theoretical (or nominal) capacities associated with concentrated load limit states are shown on the figures for the wide-flange section in question. These are represented with horizontal lines labeled FB for flange bending, WLY for web local yielding, WCR for web local crippling, and WCB for web compression buckling. Per the AISC *Specification* (2016b), flange bending only needs to be considered in design when a tension load is applied to the column flange and, therefore, would not to be considered in design for a compression load. However, the calculated limit state capacity is shown on all load-displacement results since significant bending was witnessed during all compression tests, which influenced the nonlinear behavior of the load-displacement results.

All primary results for single compression, double compression, and single tension tests are summarized in Tables 2, 3, and 4, respectively. The results in the table include the "test capacity," which is the maximum load recorded during the test, and the "effective stiffener capacity." The effective stiffener capacity is equal to the capacity of the test with stiffeners minus the result of the corresponding test without stiffeners. Negative effective stiffener capacities indicate a particular test with eccentric stiffeners that reached a lower capacity than the corresponding test without stiffeners. In these cases, it is assumed that the stiffeners had no influence on the concentrated load capacity of the column specimen, and differences are due to inconsistencies between material properties of multiple column specimens and/or imperfections in the column specimen and loading/boundary conditions when multiple tests are performed.

In Tables 2, 3, and 4, theoretical (nominal) capacities per the concentrated load limit states applicable for the test method are listed. The theoretical stiffener capacity is provided assuming the stiffeners are concentric and that the capacity is controlled by a yielding limit state at the top of the stiffener. The "theoretical capacity" varies for each type of test depending on the stiffener condition. For columns without stiffeners, the theoretical capacity represents the capacity of the lowest computed concentrated load limit state associated with the test method. For columns with concentric stiffeners, the theoretical capacity represents the lowest computed limit state in addition to the concentric stiffener capacity. For column specimens with eccentric stiffeners, the corresponding theoretical capacity is uncertain and related to the fundamental objectives of the research program and, therefore, noted as TBD in the tables.

Single Compression Test Results

Sixteen experimental column specimens were tested in single compression. This includes four wide-flange sizes and four tests per size. A summary of the primary results and theoretical capacities from the single compression tests is provided in Table 2.

Observations from the results presented in Table 2 are as follows:

- For all tests without stiffeners and with concentric stiffeners, the maximum load exceeded the theoretical capacity with one exception, W10×39 SC-E0. As described in Kowalkowski and Alvarez Rodilla (2019), this column specimen, aided with the addition of concentric stiffeners, reached a limit state associated with shear and flexural yielding in lieu of that directly influenced by local deformations from the concentrated load.
- The maximum loads obtained for all specimens with eccentric stiffeners were similar to the results of the corresponding specimens without stiffeners. There were no clear trends in the results. However, the "low eccentricity" condition always resulted in a higher capacity than the "high eccentricity" condition.
- The maximum loads for columns without stiffeners were close to the theoretical values computed for web local crippling with the exception of the W10×19 column specimen. For this case, lateral-torsional buckling was also witnessed during the test as discussed in Kowalkowski and Alvarez Rodilla (2019).
- For column specimens with concentric stiffeners, there was a significant increase in capacity in comparison to the condition without stiffeners. In addition, the effective stiffener capacity results compared well with the theoretical stiffener capacities.

Behavior of Single Compression Tests

Figure 8 shows the load-displacement relationships for the W12×26 SC column specimens and emphasizes differences in experimental behavior for different stiffener conditions. As mentioned, calculated concentrated load limit states (WCR, WLY, FB) are also shown as horizontal lines in Figure 8. Because this represents a single compression test, WLY would be the controlling limit state in design as demonstrated in Table 2.

Figure 8 indicates that the load capacity and elastic stiffness of column specimens with eccentric stiffeners are very similar to the result without stiffeners. Note that the definition of "elastic stiffness" used in this comparison is associated with the load versus actuator displacement and includes flexural, shear, and local deformations that occur in the loading plate as well as deformations that occur in

Table 2. Single Compression Theoretical Capacities and Test Results							
Column Specimen	Eccentricity (in.)	WLY (kips)	WCR (kips)	Stiffener (kips)	Theoretical Capacity (kips)	Test Capacity (kips)	Effective Stiffener Capacity (kips)
W16×31 SC-NA	NA	75.0	103	62.5	75	112	—
W16×31 SC-E6	6				TBD	99.3	–13.1
W16×31 SC-E3	3				TBD	111	–1.2
W16×31 SC-E0	0				138	177	64.4
W12×26 SC-NA	NA	52.5	74.7	76.9	52.5	78.2	—
W12×26 SC-E4	4				TBD	79.2	1.00
W12×26 SC-E2	2				TBD	87.1	8.90
W12×26 SC-E0	0				129	148	70.1
W10×19 SC-NA	NA	58.1	88.2	27.0	58.1	69.6	—
W10×19 SC-E4	4				TBD	57.4	–12.2
W10×19 SC-E2	2				TBD	70.6	1.00
W10×19 SC-E0	0				85.1	103	33.7
W10×39 SC-NA	NA	102	144	97.6	102.2	131	—
W10×39 SC-E4	4				TBD	133	1.90
W10×39 SC-E2	2				TBD	142	11.3
W10×39 SC-E0	0				200	198	67.1

the column specimen near the concentrated load. Because the flexural and shear properties of the cross section do not change, it is assumed that the primary differences in the elastic stiffness are associated with changes in local deformations that occur near the concentrated loads. The maximum load of the column specimen with a low eccentricity of 2 in. increased slightly in comparison to the condition without stiffener. However, for the concentric stiffener condition, the load increased substantially in comparison to the other conditions, and the elastic stiffness of the load-displacement relationship moderately increased. These observations demonstrate how ineffective the eccentric stiffeners were in comparison to concentric stiffeners for these column specimens and other test groups (W16×31 SC, W10×19 SC, and W10×39 SC) revealed similar conclusions.

Even though the load capacity did not increase substantially for columns tested with stiffeners at a low eccentricity, the stiffeners did assist in the post-buckling (or crippling) behavior of the column specimen, which is why a higher load was maintained for higher displacements. For the columns without stiffeners, the load decreased more rapidly after crippling occurred.

The results in Figure 8 show that three of the columns failed at a capacity close to the theoretical capacity for web local crippling (74.7 kips), which was the mode of failure identified from visual inspection of these column specimens. When the results are looked at in more detail, nonlinear behavior does initiate near the capacity associated with the limit state of web local yielding. However, the column specimens reach much higher loads after the calculated value for this limit state, and significant nonlinear behavior is not witnessed in the load-displacement relationship until web crippling initiates.

In addition to the load-displacement results, visual observations revealed that the column specimens with eccentric stiffeners behaved similar to the column specimens without stiffeners. In all three cases, yielding was first seen in the column web beneath the loading plate and continued through the web by means of strain lines radiating from the mentioned point until the column reached its maximum load and suddenly failed by web local crippling. Figure 9 shows the condition of W12×26 SC-NA after testing and provides a good representation of the deformed state of all three aforementioned column specimens after testing. Figure 9 also visually demonstrates that web local crippling was the failure mechanism of the column specimen and identifies the horizontal and vertical strain lines that appeared on the web.

As shown in Figure 8, the W12×26 SC-E0 column specimen (eccentricity = 0 in.) had a slightly higher elastic stiffness and a significantly higher load capacity than the other column specimens. Yielding was first identified at a much higher load as well. Large horizontal and vertical strain lines in the web were identified at a load of 130

kips. Yielding at the bottom flange by means of large strain lines and mill scale peeling off was also identified during the test, suggesting that significant flexural deformations were able to occur with the addition of concentric stiffeners. The total capacity of W12×26 SC-E0 was 148 kips, and the capacity of W12×26 SC-NA was 79 kips, resulting in an effective stiffener capacity of 69 kips. Figure 10 shows a close-up elevation of the column specimen after testing. The front stiffener buckled locally near the top flange and close to the concentrated load. Significant yielding was clearly observed in the stiffener prior to buckling, and therefore, the failure mode is best described as inelastic stiffener buckling. Figure 10 also shows local flange buckling and patterns of strain lines in the web and mill scale peeling off.

Double Compression Test Results

Twelve experimental column specimens were tested in double compression. This includes three wide-flange sizes and four tests per size. A W10×39 column specimen was not considered for double compression tests because preliminary finite element models revealed the capacity with stiffeners would exceed the actuator capacity. For W16×31 column specimens tested in double compression only, stiffeners near the concentrated load were only placed on one side, again due to limitations in capacity of the hydraulic actuator. A summary of the primary results from the double compression tests is provided in Table 3.

For most double compression tests, more local deformations were found near the top flange as opposed to the bottom flange. This suggests that the load was not fully transferred through the web and to the bottom reaction plate as designed. Instead, as load is applied and local deformations occur, the column specimens rotate slightly in-plane at the ends, suggesting that some of the load is transferred to the end supports. This behavior suggests that there are uncertainties associated with comparing the theoretical capacity for web compression buckling to the test capacity in Table 3. However, due to the location of the reaction plate in comparison to the end supports, as well as the condition of the reaction plate after testing, it is interpreted that most of the force was transferred through the column specimen. General observations from the results presented in Table 3 are as follows:

- The concentrated load limit state strengths calculated using AISC *Specification* Section J10 (AISC, 2016b) indicate that web compression buckling should have controlled for all column sizes when stiffeners are not present. In all cases, the maximum load of the column specimen was much higher than the predicted value. In addition, all maximum loads were higher than the theoretical capacity for web local yielding. The maximum loads for specimens without concentric stiffeners related better to the capacity predicted by web local crippling, which was the observed failure mode associated with most tests.

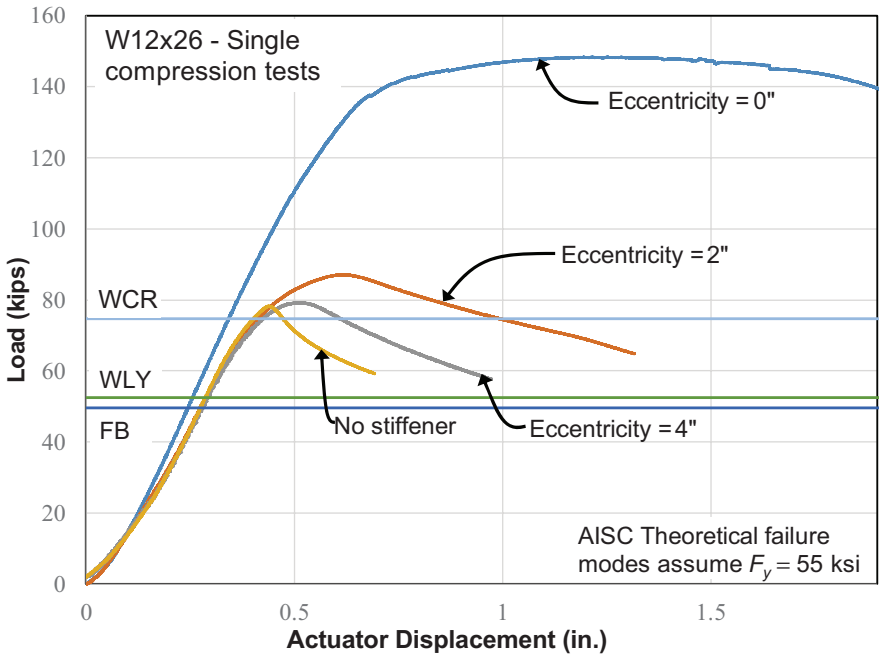

Fig. 8. Load-displacement results of W12×26 SC column specimens.

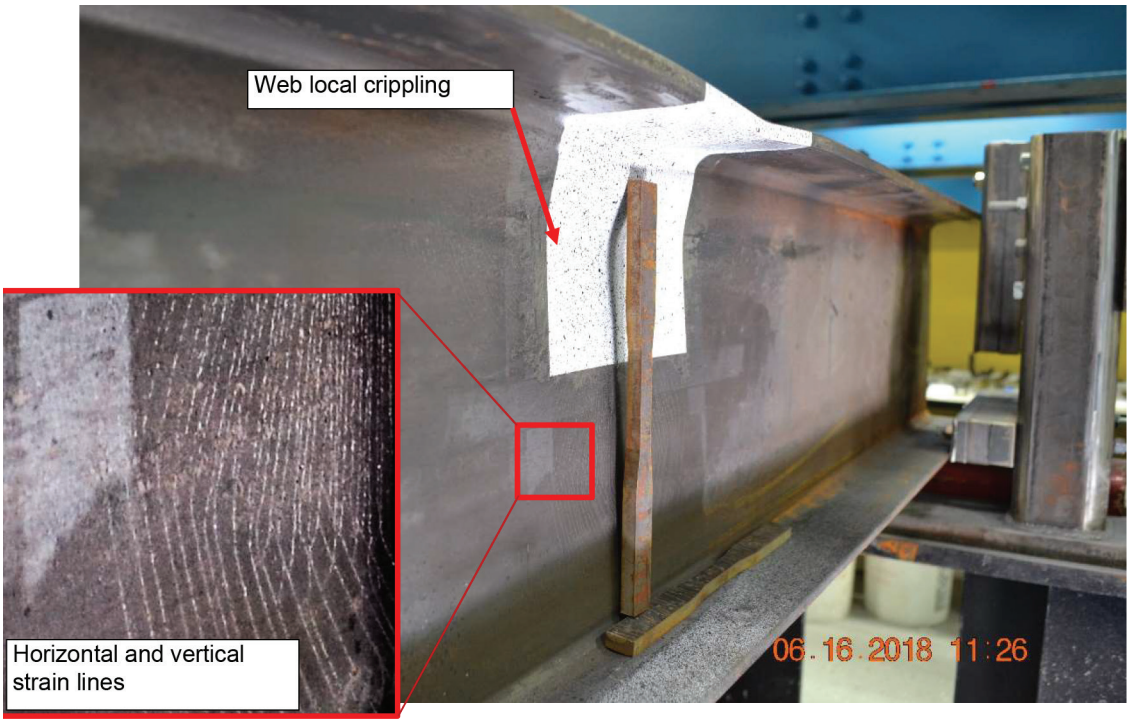

Fig. 9. W12×26 SC-NA after testing emphasizing web crippling and strain lines.

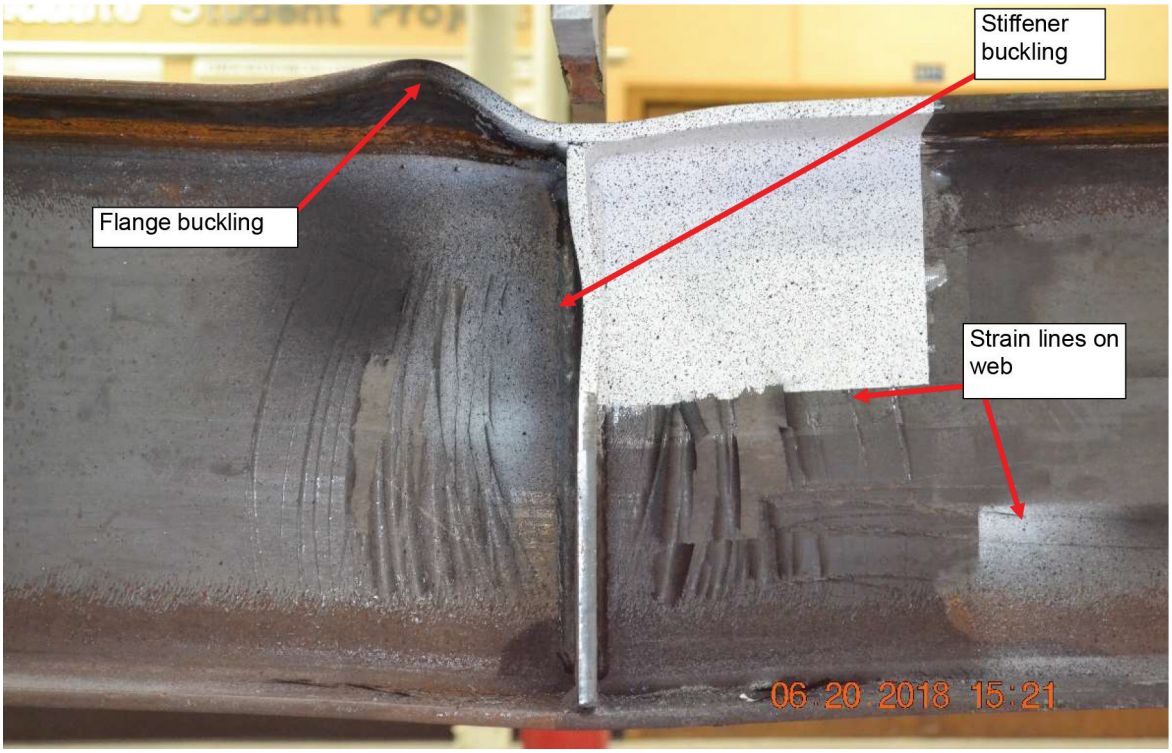

Fig. 10. Close-up view of front side of W12×26 SC-E0 after testing.

Table 3. Double Compression Theoretical Capacities and Test Results								
Column Specimen	Eccentricity (in.)	WLY (kips)	WCB (kips)	WCR (kips)	Stiffener (kips)	Theoretical Capacity (kips)	Test Capacity (kips)	Effective Stiffener Capacity (kips)
W16×31 DC-NA	NA	75.0	44.3	103	31.1	44.3	120	—
W16×31 DC-E6	6					TBD	117	–2.30
W16×31 DC-E3	3					TBD	121	1.40
W16×31 DC-E0	0					75.4	163	43.5
W12×26 DC-NA	NA	52.5	34	74.7	76.9	34	86.4	—
W12×26 DC-E4	4					TBD	90.6	4.20
W12×26 DC-E2	2					TBD	111	24.5
W12×26 DC-E0	0					111	220*	+134
W10×19 DC-NA	NA	58.1	53.7	88.2	27.0	53.7	78.5	—
W10×19 DC-E4	4					TBD	84.4	5.90
W10×19 DC-E2	2					TBD	88.0	9.50
W10×19 DC-E0	0					80.7	180	102
* Reached actuator capacity of 220 kips without failure								

- The maximum loads obtained for specimens with eccentric stiffeners were usually close to the maximum loads obtained for the corresponding specimens without stiffeners. The low eccentricity condition always resulted in a higher capacity than the high eccentricity condition. For the W12×26 test set, there was a significant increase in maximum load when the low eccentricity condition was tested. However, the effective stiffener capacity of 24.5 kips was still much lower than the effective stiffener capacity for the column specimen with concentric stiffeners, which is unknown (actuator capacity was reached) but at least 134 kips. The 24.5 kips is also significantly lower than the calculated effective stiffener capacity of 76.9 kips from Table 3. For column specimens with concentric stiffeners, there was a significant increase in capacity in comparison to the condition without stiffeners. The increase in capacity was more pronounced in comparison to the single compression tests. In addition, the effective stiffener capacities were much higher than the computed theoretical values. The double compression tests primarily fail by the concentrated load effect, and the stiffeners have a greater relative influence in bracing the web against buckling.
- For the W16×31 column specimen with one concentric stiffener, the theoretical effective stiffener capacity was noticeably less than the actual effective stiffener capacity obtained from testing. When two concentric stiffeners were used with the W12×26 and W10×19 column specimens, the theoretical effective stiffener capacity was more substantially less than the actual effective stiffener capacity obtained from testing.

Behavior of Double Compression Tests

Figure 11 shows the load-displacement relationships for the W12×26 DC column specimens and emphasizes differences in experimental behavior for different stiffener conditions. As mentioned, calculated concentrated load limit states (WCR, WCB, WLY, FB) are also shown as horizontal lines in Figure 11. Because this represents a double compression test, WCB would be the controlling limit state in design as demonstrated in Table 3.

As shown in Figure 11, the experimental results of W12×26 DC-NA and W12×26 DC-E4 were very similar. Thus, for the high-eccentricity condition, the stiffeners have a minimal influence in resisting the concentrated loads. For both of these column specimens, yielding first began in the column web beneath the top loading plate. Strain lines in horizontal and vertical patterns were seen on the web under the load. Yielding continued through the web until the column reached its maximum load and suddenly failed by web crippling near the top loading plate. From visual observations, the experimental behavior of W12×26 DC-E2 was similar. However, the stiffeners were more engaged in sharing the concentrated load, and the column specimen was able to reach a much higher displacement prior to a noticeable decrease in load. After significant yielding occurred in the web and flanges, eventually the column web failed by crippling. At the conclusion of the test, substantial flange

bending in both the top and bottom flanges was noticed as shown in Figure 12.

The experimental behavior of the W12×26 DC-E0 column specimen was significantly different from the behavior of the other column specimens in the test group. As shown in Figure 11, the test reached the maximum capacity of the hydraulic actuator of 220 kips, which was already much higher than that anticipated from theoretical calculations using the AISC *Specification* (AISC, 2016b). Yielding was identified in the stiffeners during the test by means of mill scale peeling off. Strain lines were then identified in the web and in both the top and bottom flanges. The authors believe from visual observation, from the DIC results, and the load displacement results, that the column specimen was nearing the actual load capacity. Figure 13 shows the column specimen after testing.

Single Tension Test Results

Twelve experimental column specimens were tested in single tension. This includes three wide-flange sizes and four tests per size. A summary of all the primary results from the single tension tests is provided in Table 4.

All four W10×39 column specimens reached the capacity of the hydraulic actuator. All column specimens with concentric stiffeners reached the maximum capacity of the hydraulic actuator. With the exception of W12×26 ST-E2 (discussed later), all other column specimens failed at the weld from the loading plate to the top flange of the column specimens. The failure of the weld was due to excessive flange bending causing nonuniform and, therefore, localized stresses in the weld. Observations from the results presented in Table 4 and from additional evidence of experimental behavior are as follows:

- The concentrated load limit state strengths determined using AISC *Specification* Section J10 (AISC, 2016b) are significantly lower than the maximum loads obtained for the column specimens. As discussed more in Part 2: Analytical Studies (Alvarez Rodilla and Kowalkowski, 2021), this conclusion is influenced by the weld size of ⅜ in. from the loading plate to the top flange of the column specimens, which is relatively thick for these column specimens. Part 2: Analytical Studies demonstrates how the thickness of the weld influences the flange bending capacity results in more detail.
- Although the maximum loads always exceeded the calculated capacity for flange bending, bending of the flange creates nonuniform stresses in the weld. When concentric stiffeners are used, this negates bending of the flange, and the welds are capable of resisting a much higher load because more uniform stresses are present.
- From the W16×31 ST test set, eccentric stiffeners have a minimal influence on the concentrated load capacity of the column specimen. However, the low eccentricity condition resulted in a slightly higher capacity than the high eccentricity condition.

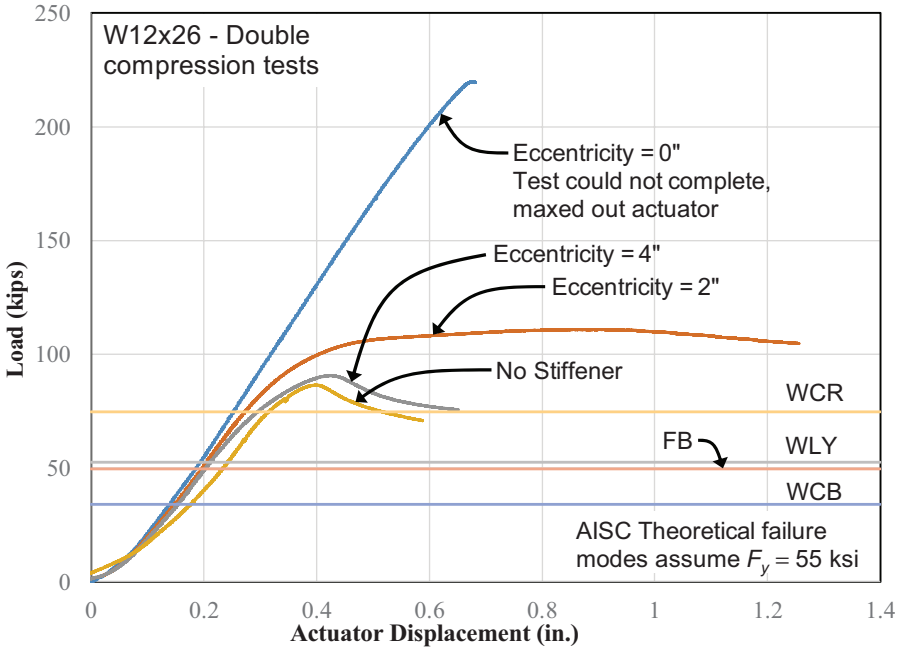

Fig. 11. Load-displacement results of W12×26 DC column specimens.

- A low-tone "bang" was heard while testing W12×26 ST-NA. The intensity of this bang was not nearly as high as expected after performing the tests on W16×31 ST members and further tests on W12×26 ST specimens. From the behavior witnessed, it appeared this test failed prematurely. For the purposes of this work, it is alleged that the capacity of W12×26 ST-NA would have been very similar to W12×26 ST-E4 if this did not occur. However, there is a notable increase in capacity when the low eccentricity condition was tested, which is similar to the comparisons for the double compression tests performed on this column size.
- For column specimens with concentric stiffeners, there is a significant increase in capacity in comparison to the condition without stiffeners, and it is assumed that if the specimens were tested to their true capacity, similar relationships would be obtained as found for the compression studies.

Behavior of Single Tension Tests

For column specimen W12×26 ST-E2, yielding began in the web below the applied load. Strain lines parallel to the direction of the applied load were identified in the web. The column specimen reached its capacity when failure occurred in the weld between the top flange and the inside face of the stiffener. Then, the crack propagated from the weld into the web and below the concentrated load. A few tension tests performed by Graham et al. (1959) also failed by web fracture just below the fillet, but it appeared

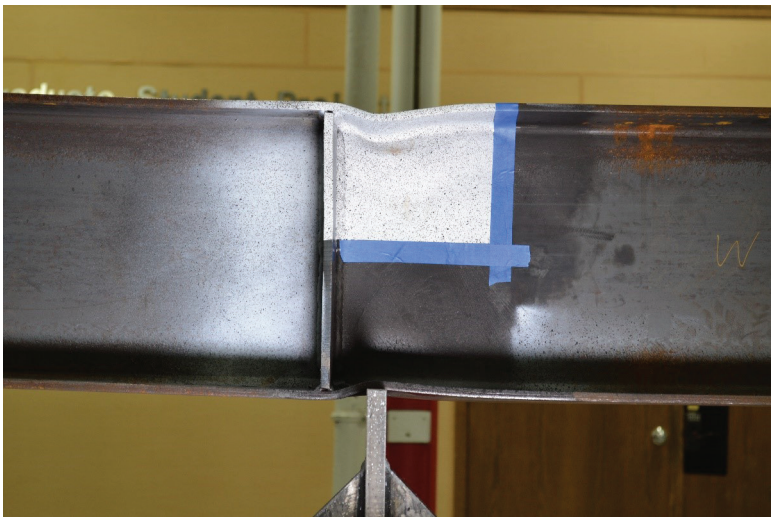

Fig. 12. Elevation view of W12×26 DC-E2 after testing.

Fig. 13. Elevation view of W12×26 DC-E0 after testing.

Table 4. Single Tension Theoretical Capacities and Test Results							
Column Specimen	Eccentricity (in.)	WLY (kips)	FB (kips)	Stiffener (kips)	Theoretical Capacity (kips)	Test Capacity (kips)	Effective Stiffener Capacity (kips)
W16×31 ST-NA	NA	76.9	66.6	62.5	66.6	127	—
W16×31 ST-E6	6				TBD	126	–1.50
W16×31 ST-E3	3				TBD	129	2.00
W163×1 ST-E0	0				160	144*	+17.0
W12×26 ST-NA	NA	54.1	49.6	76.9	49.6	79.2	±
W12×26 ST-E4	4				TBD	115	35.9
W12×26 ST-E2	2				TBD	134	54.5
W12×26 ST-E0	0				123	144*	+65.0
W10×39 ST-NA	NA	104	96.6	97.6	96.6	144*	—
W10×39 ST-E4	4				TBD	144*	NA
W10×39 ST-E2	2				TBD	144*	NA
W10×39 ST-E0	0				194	144*	NA
* Reached actuator capacity							

from visual observations that failure initiated in the stiffener weld, and therefore, the behavior is different. Fracture through the web of column specimen W12×26 ST-E2 is shown in Figure 14.

Figure 15 shows the load-displacement relationships for the W16×31 ST column specimens and emphasizes differences in experimental behavior for different stiffener conditions. As mentioned, calculated concentrated load limit states (WLY, FB) are also shown as horizontal lines in Figure 15. For this column specimen and for all column specimens subjected to single tension, FB would be the controlling limit state in design as demonstrated in Table 4. Three of the four column specimens reached a maximum load between 125 and 129 kips. The maximum load for the column specimen with stiffeners at a high eccentricity was slightly less than for the column specimen without stiffeners. The test capacity for the column specimen with stiffeners at a low eccentricity was slightly higher than for the column specimen without stiffeners. However, all three capacities were very similar, and in general, eccentric stiffeners have negligible influence on the maximum loads for this column size and these magnitudes of eccentricity.

Figure 15 indicates that all four column specimens had a similar elastic stiffness. The test with concentric stiffeners had the highest elastic stiffness and maintained elastic behavior until the actuator capacity was reached. For specimens without concentric stiffeners, nonlinear behavior does initiate near the limit state of web local yielding (WLY). However, the column specimens reach a much higher capacity than that computed for this limit state and for flange bending (FB).

All three of the column specimens without stiffeners eventually failed by rupture of the welds between the loading plate and the top flange of the column. The weld failure occurred as a loud and sudden bang with limited warning. Weld failure was influenced by excessive flange bending, which creates higher stresses in localized areas of the weld. The outside tips of the flange move more vertically with the loading plate because the localized stiffness of the flange is smaller near the tips. At the center of the weld, the flange is less prone to move with the plate because the web on the backside of the flange resists it. Therefore, higher stresses develop near the center of the welds along the length.

Visual inspection of the tests and the load-displacement behavior show that eccentric stiffeners do not effectively resist flange bending, and therefore, uneven stresses still develop in the welds. A photograph of W16×31 ST-E6 that shows the weld failure and emphasizes the large, localized deformations that occur is provided in Figure 16.

Figure 17 shows an elevation of W16×31 ST-E6 after testing and identifies inelastic deformations that occurred in the web and flange. Figure 17 also identifies the approximate "width" of flange bending (FB width). Yielding occurs in the flange within this width where significant out-of-plane deformations occur in the flange. For this column specimen, the eccentric stiffeners were not found within this effective width and, therefore, did not resist the flange bending effect.

The column specimen W16×31 ST-E0 with concentric stiffeners reached the maximum capacity of the actuator at 144 kips. There were no signs of yielding or other significant deformations when the actuator capacity was reached,

and it is likely that the load capacity comparisons in single tension would be similar to the results in single compression. The primary difference in the concentric stiffener condition is that load is transferred directly to the stiffeners, which stiffen the flange from bending. The entire weld will therefore develop more uniform deformations across the width of the flange upon loading. The maximum capacity of the connection would likely be closer to the nominal capacity of the welds themselves, which is computed as 185 kips using AISC *Specification* Section J2 (AISC, 2016b).

CONCLUSIONS

The following are the primary conclusions from all of the experimental investigations considering single compression, double compression, and single tension test results. The conclusions are based on the smaller column sizes that were tested experimentally. Note that the research is further evaluated in Part 2: Analytical Studies (Alvarez Rodilla and Kowalkowski, 2021), which provides more in-depth analysis of larger column specimens.

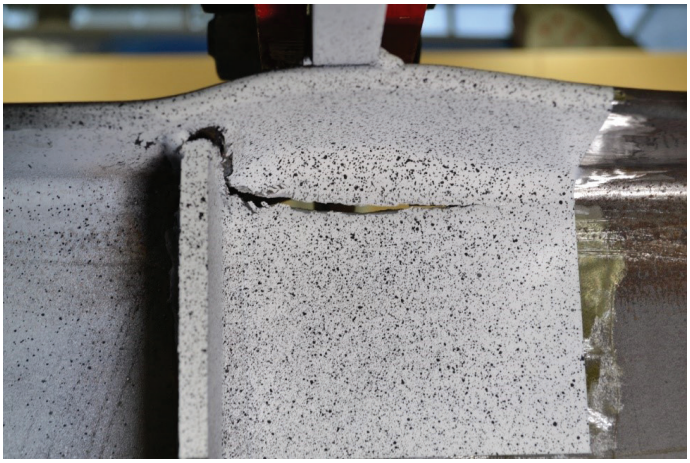

Fig. 14. W12×26 ST-E2 after testing with weld and web fracture.

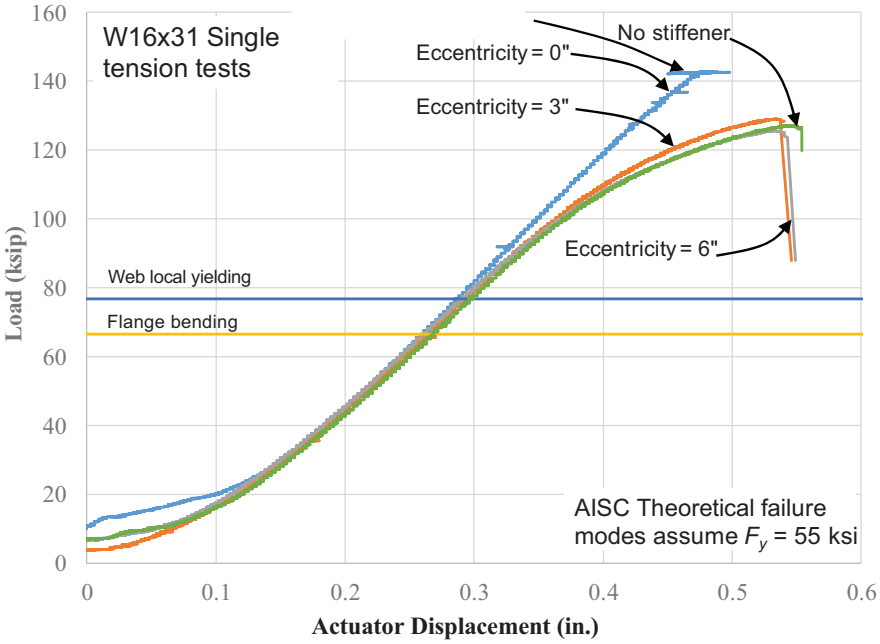

Fig. 15. Load-displacement results of W16×31 ST column specimens.

- All single and double compression tests without concentric stiffeners reached a maximum load when web local crippling occurred, causing a sudden decrease in load. The maximum load generally compared favorably to that calculated for this limit state using the AISC *Specification* (AISC, 2016b) (the theoretically governing limit state was computed as web local yielding for single compression and web compression buckling for double compression).
- For compression tests with concentric stiffeners, the maximum load was generally obtained when inelastic stiffener buckling occurred. The maximum load for single compression results was also influenced by inelastic flexural and shear stresses in the cross section from moment and shear, respectively.

Fig. 16. Weld fracture of W16×31 ST-E6 after testing (side 1).

- For single tension tests, when the actuator capacity was not reached, failure generally occurred in the weld from the loading plate to the top flange of the column specimen due to nonuniform weld stresses between the loading plate and top flange.
- For all test methods, when column specimens are tested without stiffeners, the maximum load is much higher than that predicted by the limit state of web local yielding. However, from visual inspection and load-displacement results, yielding of the web does occur prior to reaching the load carrying capacity.
- For single tension tests without stiffeners, the maximum loads obtained significantly exceeded the capacity calculated for the limit state of flange bending.
- For double compression tests without stiffener, the maximum loads obtained significantly exceeded the capacity calculated for the limit state of web compression buckling.
- In all tests, the effective stiffener capacity for column specimens with eccentric stiffeners was between 0% and 18% (not using negative effective stiffener capacities) of the effective stiffener capacity for column specimens with concentric stiffeners.
- Information in AISC Design Guide 13 (Carter, 1999), which suggests that the capacity of eccentric stiffeners is 65% of that of concentric stiffeners at an eccentricity of 2 in., is not adequate for these smaller column sizes.

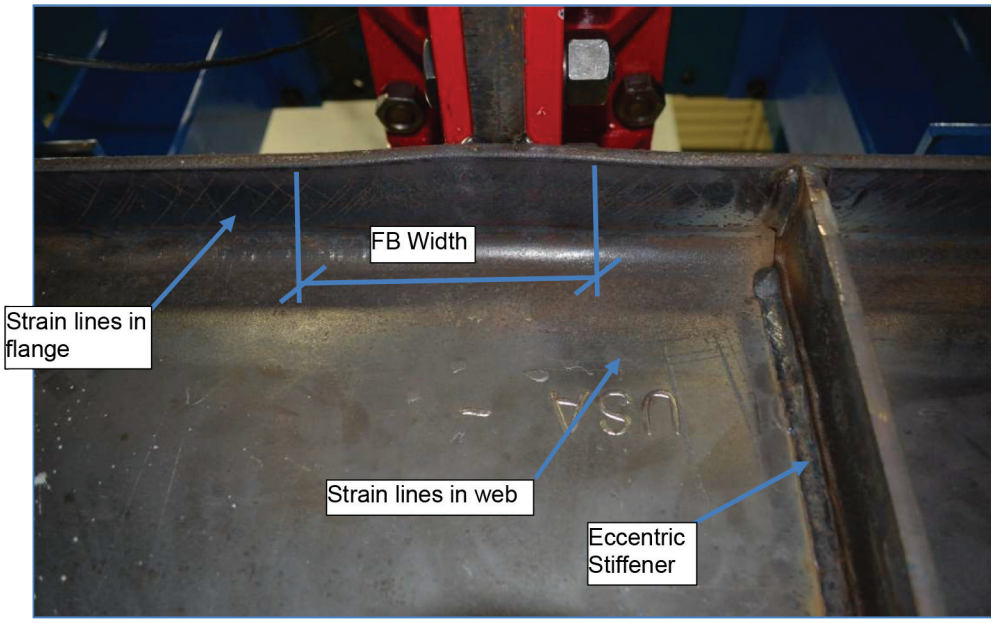

Fig. 17. Elevation view of W16×31 ST-E6 after testing.

LIMITATIONS

A limitation of the experimental studies presented in this paper is that only small wide-flange sections were considered due to limitations in capacity of the hydraulic actuator. Limited valuable test results were obtained for the single tension loading condition since one weld failed prematurely and several other tests reached the capacity of the hydraulic actuator. Larger column sizes were modeled analytically and provide further clarity on the influence of eccentric stiffeners as presented in Kowalkowski and Alvarez Rodilla (2019) and in Part 2: Analytical Studies (Alvarez Rodilla and Kowalkowski, 2021). Testing of larger column specimens was necessary to complete the scope of the project and to come up with recommendations that can be applied in design. All final recommendations are presented in Part 2: Analytical Studies.

Comparisons between the experimental results and theoretical capacities were made assuming a yield stress of 55 ksi for the experimental beam specimens. Tension tests were performed on tension coupons with the yield stress ranging from 52 to 59 ksi. However, an accurate yield stress could not be designated for every beam specimen.

ACKNOWLEDGMENTS

This research was sponsored by the American Institute of Steel Construction and conducted by using the laboratory facilities of Lawrence Technological University (LTU). The data compilation and report preparation were supported by the Department of Civil and Architectural Engineering and LTU and all DIC data was processed in collaboration with the Department of Mechanical, Robotics and Industrial Engineering at LTU.

REFERENCES

AISC (2016a), *Seismic Provisions for Structural Steel Buildings*, ANSI/AISC 341-16, American Institute of Steel Construction, Chicago, Ill.

AISC (2016b), *Specification for Structural Steel Buildings*, ANSI/AISC 360-16, American Institute of Steel Construction, Chicago, Ill.

Alvarez Rodilla, J. and Kowalkowski, K.J. (2021), "Determination of Capacities of Eccentric Stiffeners Part 2: Analytical Studies," *Engineering Journal*, AISC, Vol. 58, No. 2, pp. 99–122.

ASTM (2009), *Standard Test Methods for Tension Testing of Metallic Materials*, ASTM E8/E8M-09, ASTM International, West Conshohocken, Pa.

Carter, C.J. (1999), *Stiffening of Wide-Flange Columns at Moment Connections: Wind and Seismic Applications*, Design Guide 13, AISC, Chicago, Ill.

Graham, J.D., Sherbourne, A.N., and Khabbaz, R.N. (1959), "Welded Interior Beam-to-Column Connections," Report for AISC, Chicago, Ill.

Kowalkowski, K.J. and Alvarez Rodilla, J. (2019), "Analysis and Design of Eccentric Stiffeners Part of Moment Connections to Column Flanges," Final Report for AISC, Chicago, Ill.

Norwood, J. (2018), "Effect of Continuity Plate Eccentricity on the Performance of Welded Beam-to-Column Connections," Master's Thesis, Department of Civil Engineering, University of Arkansas.

Sherbourne, A.N. and Murthy, D.N.S. (1978), "Computer Simulation of Column Webs in Structural Steel Connections," *Computers and Structures*, Vol. 8, May, pp. 479–490.

Determination of Capacities of Eccentric Stiffeners Part 2: Analytical Studies

JAVIER ALVAREZ RODILLA and KEITH KOWALKOWSKI

ABSTRACT

Analytical investigations were performed on column specimens with an effort to evaluate the effective stiffener capacity of eccentric stiffeners when used within moment connections of beams connecting to column flanges. First, analytical models were developed for the experimental column specimens presented in the companion paper Part 1: Experimental Studies (Alvarez Rodilla and Kowalkowski, 2021). These models were utilized to calibrate the finite element methodology and to develop consistent comparisons between the experimental and analytical results.

Finite element models were then developed for larger column sizes more regularly used in practice. In all, 148 models were developed to represent W14×68, W14×120, W14×176, W14×233, W24×131, and W24×229 column specimens. The column models utilized a similar setup to experiments and were subjected to three different loading conditions described as (1) single tension with load pulling away from the column specimen; (2) single compression with load applied toward the column specimen; and (3) double compression with loads applied on both flanges, directly opposite of each other. Parameters also included the unsupported length and stiffener thickness for single compression, the stiffener thickness for double compression, and the weld size/loading plate thickness for single tension. For all test methods and each set of parameters, a group of four column specimens consisted of (1) one modeled without stiffeners, (2) one modeled with concentric stiffeners, (3) one modeled with stiffeners at an eccentricity of 2 in., and (4) one modeled with stiffeners at an eccentricity of 4 in.

The results of the finite element models demonstrate that eccentric stiffeners in practical column sections are more effective in resisting the concentrated load in comparison to smaller column sections. In addition, there were direct trends observed between the magnitude of eccentricity and the elastic stiffness and maximum loads. Utilizing the results, recommendations for determining the effective stiffener capacity of eccentric stiffeners are presented. The recommendations are dependent on the ratio of eccentricity versus flange thickness, or the e/t_f ratio. The research showed that stiffeners at any eccentricity are not effective for a flange thickness less than ½ in. The testing and modeling performed as part of this project studied stiffeners with a maximum eccentricity of 4 in., and therefore, recommendations are limited to this maximum eccentricity.

The analytical investigations also evaluated the limit states associated with concentrated loads with respect to resistance of the column specimen and determined that maximum loads compare well with the limit state of web local crippling and exceeded the limit states of web local yielding and web compression buckling for double compression tests. The results also demonstrate that for an applied tension force, the influence of flange bending should be integrated into the calculations associated with the weld strength in lieu of being evaluated as an independent limit state.

KEYWORDS: steel columns, eccentric stiffeners, moment connections, concentrated loads, flange bending, web compression buckling, web local crippling, web local yielding.

INTRODUCTION AND BACKGROUND

A comprehensive research project was performed at Lawrence Technological University (LTU) to evaluate the influence of stiffener eccentricity on the effective resistance of column members when subjected to concentrated loads as part of moment connections. The study can be extended for the design of stiffeners for other scenarios when wide-flange beams are subjected to concentrated loads. Funding for the research project came from the American Institute of Steel Construction (AISC). For the project, 40 experimental column specimens were tested under concentrated loads without stiffeners, with concentric stiffeners, and with stiffeners at an eccentricity up to 6 in. from the concentrated load. The experimental column specimens were limited to lighter cross sections (W10×19, W10×39, W12×26, and W16×31) due to limitations in the lab facility.

Analytical finite element models were developed to represent the experimental column specimens to calibrate/verify the finite element methodology. Analytical models were developed for larger column sections used more routinely in practice, with additional parameters considered. These column specimens will be referred to as "practical" column specimens herein. This paper discusses the

Javier Alvarez Rodilla, EIT, Graduate Research Scholar, Lawrence Technological University, Southfield, Mich. E-mail: jalvarezr@ltu.edu

Keith Kowalkowski, PhD, PE, SE, Associate Professor, Lawrence Technological University, Southfield, Mich. E-mail: kkowalkow@ltu.edu (corresponding)

Paper No. 2019-16R(2)

analytical studies that followed the experimental investigations. The experimental investigations are presented in the companion paper, Part 1: Experimental Studies (Alvarez Rodilla and Kowalkowski, 2021).

Specifically, this paper describes the methodology used to develop the finite element models. It also shows comparisons between the experimental and analytical results and presents the primary results of the models for practical column specimens. The primary results show relationships between stiffener eccentricity and the effective stiffener capacity. Lastly, the results are compared with the AISC (AISC, 2016) limit states associated with concentrated loads.

The companion paper to this [Part 1: Experimental Studies (Alvarez Rodilla and Kowalkowski, 2021)] provides a thorough overview of background information related to the objectives of the research with a truncated overview provided in this paper. Graham et al. (1959) performed experimental investigations on steel members subjected to concentrated loads with concentric stiffeners and eccentric stiffeners. The primary results of the research showed that transverse stiffeners with a 2-in. eccentricity provide 65% of the strength of an identical concentric transverse stiffener. In addition, it was recommended, "…for design purposes, it would probably be advisable to neglect the resistance of stiffeners having eccentricity greater than 2 in. The required transverse stiffener area, width and thickness can be established by the same criteria as for concentric stiffeners, provided that the strength is reduced linearly from 100 percent at zero eccentricity to 65 percent at 2 in. eccentricity."

Sherbourne and Murthy (1978) performed analytical investigations to study concentrated loads applied to wide-flange sections. The research focused on analyzing the stability of column webs in beam-column moment connections. The author carried out analytical tests on wide-flange sections with concentric and eccentric stiffeners. Eccentric stiffeners were placed at an eccentricity of 25% and 50% of half the column depth. The results showed that the maximum load obtained for the eccentric stiffener cases decreased dramatically compared to the cases with concentric stiffeners, regardless of the column's flange and/or web thickness. At the lower eccentricity, the effectiveness of the stiffeners ranged between 50 and 75% of that for concentric stiffeners. Sherbourne and Murthy also found that the web thickness has a direct influence on the buckling load and behavior of the column.

Norwood (2018) performed analytical research on wide flange sections modeled similar to the experimental tests carried out by Graham et al. (1959) using the finite element method and program ABAQUS (2014). Norwood found that increasing the level of stiffener eccentricity results in a decrease in resistance to concentrated forces. However, the results showed that stiffeners at a 2-in. eccentricity were more effective than the 65% factor provided by Graham et al. The models consisted of four-noded linear shell elements with reduced integration as well as a cyclic nonlinear kinematic material hardening based on the plastic strain behavior of A572 Gr. 50 steel. As discussed in the next section, the material properties utilized were similar to those used for the finite element models presented in this paper. However, the choice of element type and the analysis method are notably dissimilar.

OVERVIEW OF FINITE ELEMENT MODELS

Model Parts and Element Types

Finite element models included the column specimens themselves, stiffeners at or near mid-length, bearing stiffeners near the supports, and loading plates. Loading plates include the top loading plate for all test methods and the bottom reaction plates for double compression tests. Figure 1 provides a screenshot showing an isometric view of the finite element model of a W14×68 double compression column specimen with concentric stiffeners (or mid-length and in line with applied load). This finite element model does not have bearing stiffeners. However, for single tension and single compression models, bearing stiffeners were modeled in the same way as mid-length stiffeners.

Models of steel plates utilized either solid elements or shell elements. Models for wide flange column specimens utilized solid elements due to the presence and significance of the fillet region of the column specimens. Solid elements were also used for modeling the loading plates and welds. Initially, type C3D8I elements were used for calibration of the models, which are eight-node, three-dimensional continuum elements with three degrees of freedom per node and enhanced by incompatible modes to improve bending behavior (ABAQUS, 2014). However, for some practical column specimens, the finite element models had issues converging to a solution due to severe distortions of the elements. Therefore, in all models of practical column specimens, the column specimens and loading plates were modeled with type C3D8R elements, which is an eight-node linear brick, reduced integration with hourglass control element (ABAQUS, 2014). Studies in Kowalkowski and Alvarez Rodilla (2019) showed negligible differences in the results of column specimens modeled using both types of elements. High local deformations near the application of the concentrated load required finer meshes to be used in these areas. Conversely, coarser meshes were utilized away from the concentrated loads and near supports where local deformations are less significant. Mesh sensitivity studies were performed prior to initiating the experimental investigations. As shown in this paper, because the analytical

results compare favorably to experimental results with respect to maximum loads, it is assumed that the element mesh was adequate.

Stiffeners were modeled utilizing four-node linear shell elements of type S4 (ABAQUS, 2014). These elements are general-purpose shell elements and have six deformation degrees of freedom per node.

For all compression tests, the loading plates were modeled by direct attachment to the column specimens by sharing the nodes. Modeling of welds between the loading plates and the top flange of the column specimen was deemed critical for all tension models. Welds were modeled with C3D8 elements (ABAQUS, 2014). These elements are three-dimensional continuum elements with three degrees of freedom per node. The elements were arranged together in a triangular pattern with a slight gap at the apex. In order to provide compatibility between the welds and the connecting flange and plate, each node on the welds that connect to the plate elements was constrained (slaved) to a node on the plate elements, therefore ensuring the displacements in all three directions (DOF 1, 2, and 3 as shown in Figure 4) were the same. A screenshot of a finite element model at the weld location is shown in Figure 2.

Material Properties

Calibration of finite element models for the experimental column specimens utilized material properties determined from uniaxial tension tests performed per ASTM E8/E8M-09 (ASTM, 2009) on samples fabricated from the webs and flanges of the column specimens. Practical column specimen models utilized minimum material properties defined in the AISC *Steel Construction Manual* (AISC, 2017) for ASTM A992 steel. These properties include a minimum yield stress of 50 ksi, a minimum ultimate stress of 65 ksi,

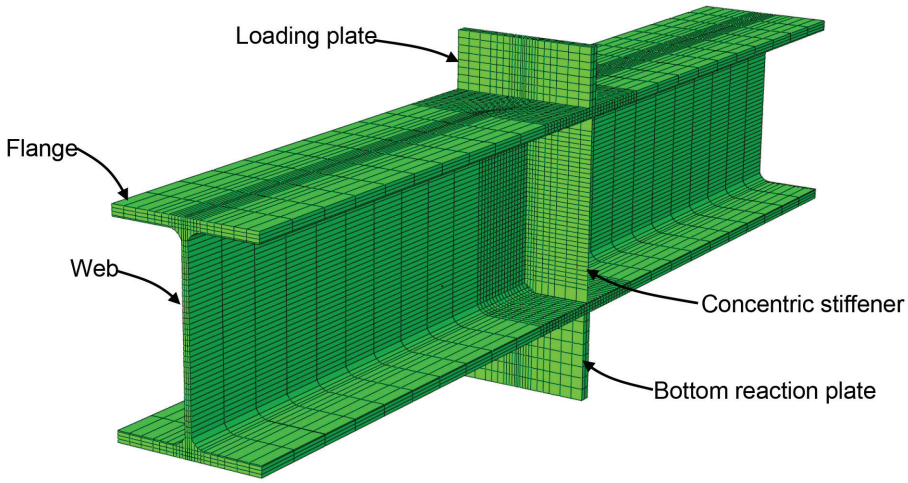

Fig. 1. Isometric view of finite element model of W14×68 double compression specimen.

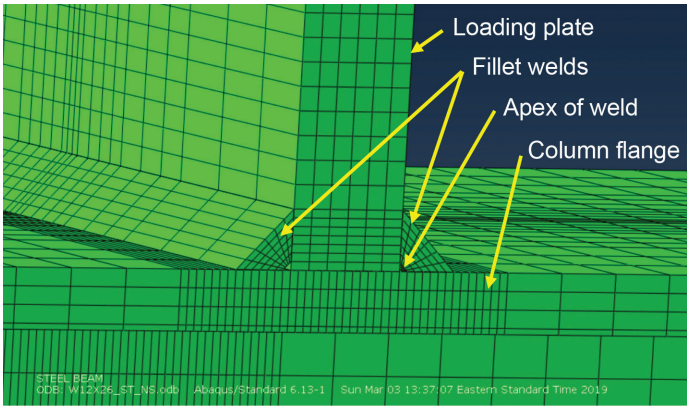

Fig. 2. Finite element model of a single tension test at the weld.

and an elastic modulus of 29,000 ksi. Results from uniaxial tension tests performed on samples fabricated from the column specimens formed the basis of stress-strain relationships used in modeling. Figure 3 demonstrates how the engineering stress-strain curves derived from samples taken from the column specimens were modified to develop similar engineering stress-strain curves with the minimum properties specified for A992 steel.

During the experimental investigations, uniaxial tension tests on samples fabricated from stiffener material revealed that some of the material met the requirements for both ASTM A36 and ASTM A572 material and was thus dual-certified material. Due to uncertainties associated with the stiffener material and properties of stiffeners used in practice, all stiffeners were modeled with the same material properties as the column specimens in both the calibration studies and the practical column specimen studies. Some differences are anticipated in results if different material properties are used. However, in most analytical models with mid-length stiffeners, the stiffeners buckled, which is less dependent on the strength of the material and more dependent on the elastic modulus, which is relatively constant for various steel grades.

Loading plates in finite element models of practical column specimens were modeled as elastic only with an elastic modulus of 29,000 ksi. The elastic behavior allowed the loading plates to deform as the column specimen flanges and/or welds deformed but prevented them from developing significant inelastic deformations and thus controlling the failure mode associated with the finite element models.

Material properties of the weld were deemed critical for all single tension models. The basis of this assertion comes from the experimental studies showing the maximum load is generally governed by non-uniform stresses that develop in the welds. Several researchers have reported the yield and ultimate stress of weld materials. For instance, Bowman and Quinn (1994) and Kartal et al. (2007) presented weld material test results. The nonlinear stress-strain curve and the ultimate stress of the weld material (82.4 ksi) was based on the experimental results by Kartal et al. Additional information regarding the literature review on weld material properties and an idealization used in the analytical models for the nonlinear stress-strain curve is found in Kowalkowski and Alvarez Rodilla (2019).

Boundary Conditions and Loading

The connection between the stiffeners and the column section (shell-to-solid connection) was modeled by extending the elements of the stiffeners one-element thickness into the solid elements and connecting the nodes on the stiffeners to the intersecting nodes within the solid elements.

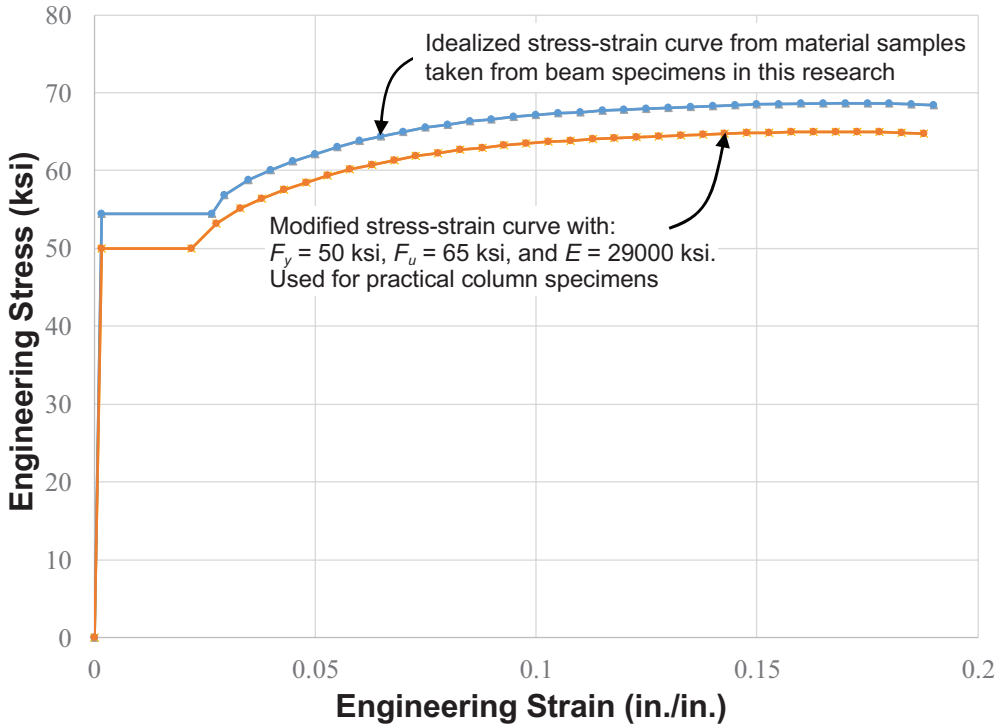

Fig. 3. Idealized stress-strain curves used for analytical studies.

To relate to the experimental tests presented in Part 1: Experimental Studies (Alvarez Rodilla and Kowalkowski, 2021), all column specimens were assumed to react against roller supports. For the compression models, the supports were located 6 in. from the ends and in contact with the bottom nodes of the bottom flanges. Roller supports were modeled in contact with the top flange in tension models. In the analytical models, the nodes along the width of the flange at these locations were fixed vertically (DOF 2, see Figure 4) to simulate the boundary conditions.

The center nodes on the loading plates and through the depth were fixed in the transverse direction (DOF 3) to avoid elastic buckling under higher loads. Loading was applied by specifying an incremental displacement using the *BOUNDARY option (ABAQUS, 2014). The center node on the top of the loading plate was modeled as the control node to specify the displacement. Other nodes on the top surface of the top plate were slaved to the control node in the vertical direction (DOF 2). The top of the top plate was also fixed in the other transverse direction (DOF 1). Figure 4 shows an isometric view of a finite element model of a W10×39 column specimen and graphics associated with the boundary conditions.

In the experimental investigations, the double compression tests revealed that fewer local deformations occurred near the bottom flange of the column specimen as opposed to the top flange of the column specimen, and the end of the column specimen rotated slightly about the *x*-axis of the cross section (DOF 1 per Figure 4) as local deformations progressed. These observations suggest the load did not completely transfer from the upper loading plate to the bottom reaction plate. Instead, some of the force transfers to the end supports. During the calibration phase with the experimental column specimens, the bottom of the bottom plate was fixed in all three directions (DOF 1, 2, and 3) because loading was only applied from the actuator on the top. However, for the practical column specimens, the bottom plate was constrained to have the same displacement as the top loading plate but in opposite directions, simulating a true through force and equal local deformations on each side of the column flange, similar to the condition in an actual moment connection with equal compression forces on either side of the column.

Analysis Procedure

Multiple analysis procedures were evaluated to simulate and analyze the deformations and stresses that develop in the finite element models. In all cases, loads were applied in increments to observe the load-displacement results and behavior. For all the single tension models, a general static analysis was performed using the *STATIC analysis procedure available in ABAQUS. For compression models, first, an eigenvalue analysis was carried out in ABAQUS to simulate a buckled shape. In the eigenvalue analysis, the finite element software identifies multiple buckling or mode shapes for the column specimen. The eigenvalue analysis in ABAQUS scales the maximum resultant displacement at any point to a maximum value of 1 (in this case, this would represent 1 in. because in. were assumed in the development of all models). Following the eigenvalue analysis, a geometric imperfection was specified in ABAQUS, which represents a small percentage of the buckled shape determined from the eigenvalue analysis. After specifying the

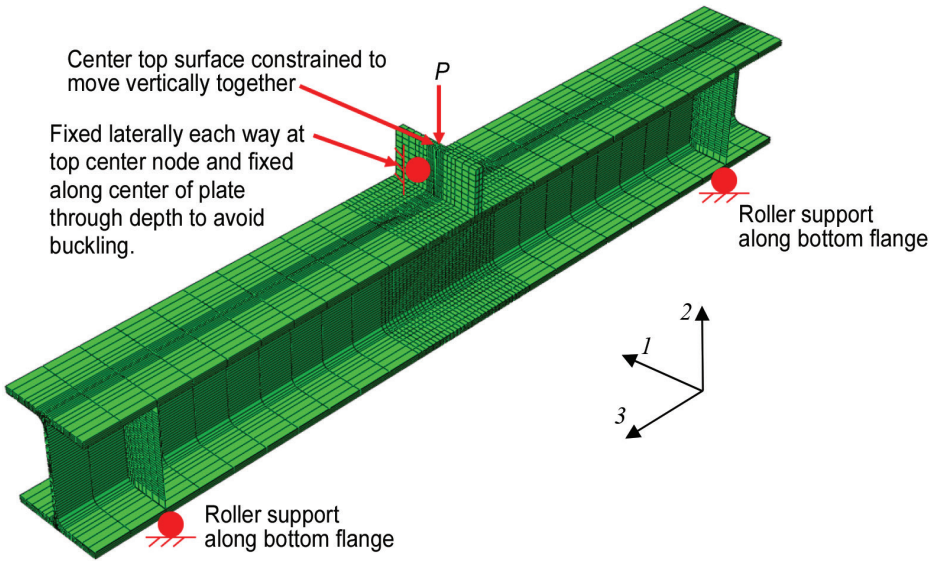

Fig. 4. Isometric view of finite element model showing boundary conditions.

Table 1. Analytical Test Matrix for Experimental Column Specimens	
Column Specimen Nomenclature	**Column Specimen Nomenclature**
W10×19 DC-E0	W12×26 SC-E0
W10×19 DC-NA	W12×26 SC-NA
W12×26 DC-E0	W12×26 SC-E4
W12×26 DC-NA	W12×26 ST-E0
W12×26 DC-E4	W12×26 ST-E4
W16×31 DC-NA	W16×31 ST-E0
W10×39 SC-E0	W16×31 ST-NA
W10×39 SC-NA	

imperfection, a static-stress analysis was performed using the *STATIC RIKS option. The *STATIC RIKS analysis is generally used to predict geometrically nonlinear collapse of a structure (ABAQUS, 2014). This allowed the models to buckle by modes of web local crippling, web compression buckling, and stiffener buckling and to study the post-buckling behavior. The analyses performed for each type of model is demonstrated in Figure 5.

CALIBRATION STUDIES FOR FINITE ELEMENT MODELS

Analytical investigations using the experimental column specimens were performed to calibrate the finite element modeling techniques. Finite element models were developed for all four experimental column specimen sizes (W16×31, W12×26, W10×19, and W10×39). Fifteen finite element models were used for this study. Table 1 shows the full analytical test matrix for the experimental column specimens. The nomenclature used for each column specimen includes the column specimen size, the test method, and the stiffener condition. For the test method, DC refers to double compression, SC refers to single compression and ST refers to single tension. For the stiffener condition, NA indicates a test without mid-length stiffeners, E0 refers to a column specimen with concentric stiffeners, and E4 refers to a column specimen with stiffeners at an eccentricity of 4 in.

The calibration studies identified that the analytical models for column specimens compared well with the experimental results when using a geometric imperfection during the *STATIC RIKS analysis (ABAQUS, 2014) for compression tests. Different magnitudes of geometric imperfections were evaluated in the calibration studies. Imperfections exist in any steel cross section as no member is fabricated perfectly. However, accurate measurements of such imperfection were not considered during the experimental phase of the project. A magnitude of imperfection

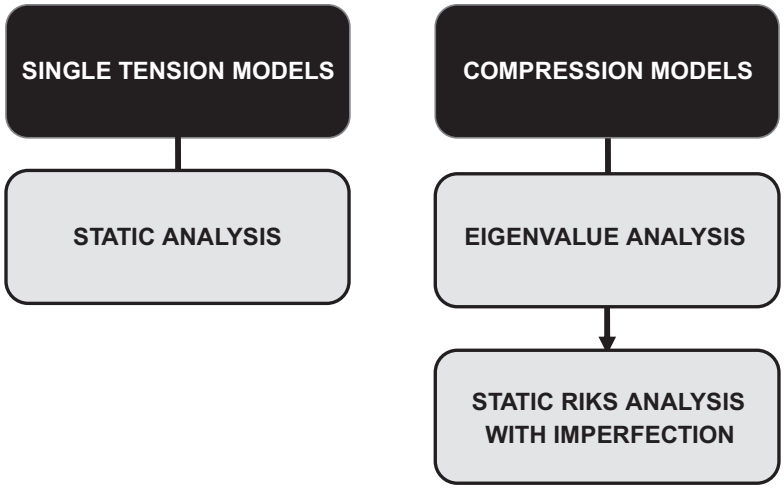

Fig. 5. Analysis procedure for different types of analytical models.

equal to 0.001% (maximum out-of-plane deformation = 0.00001 in.) of the displacement of the buckled shape from the eigenvalue analysis provided the best analytical results in comparison to the experimental results for most column specimens. For instance, Figure 6 shows the load-displacement results for finite element models of a W10×39 column specimen tested in single compression and without stiffeners (W10×29 SC-NA) and for various imperfections compared to the experimental results. There are discrepancies between the analytical and experimental results with respect to the elastic stiffness. The research team could not identify any flaws with the analytical models to account for this. The analytical results were compared to theoretical predictions in the elastic range only, and analytical and theoretical studies discussed in Kowalkowski and Alvarez Rodilla (2019) indicated that the finite element models are accurately predicting the elastic stiffness and displacement results. Therefore, discrepancies were due to flaws in the experimental stroke displacement of the actuator. The maximum loads and behavior when web crippling occurred compared favorably for all compression models when utilizing a 0.001% imperfection. Figure 6 thus helps support the justification for the use of a 0.001% imperfection in the model.

Studies were performed for all compression tests listed in Table 1 in a similar way to those done to generate Figure 6. The analytical results were in line with one of the primary conclusions discussed in Part 1: Experimental Studies (Alvarez Rodilla and Kowalkowski, 2021) in that, for these column sizes, eccentric stiffeners at an eccentricity of 4 in. have a small influence on the maximum load obtained for the column specimen and web crippling still occurred.

It was critical for the single tension tests to calibrate when weld fracture occurred in the elements utilized for modeling welds. Weld failure was assumed to occur when the von Mises stress exceeded the ultimate stress, specified as 82.4 ksi (discussed previously). Also, plastic strains were checked in the models and failure was defined as equivalent plastic strains exceeding 0.2 in./in. For all finite element models of single tension tests, the loads corresponding to when these two events occurred compared favorably to the maximum loads obtained in the experimental results when weld fracture occurred. In the analytical models of practical column specimens, failure was always assumed to occur when the von Mises stress exceeded the ultimate stress of 82.4 ksi. The equivalent plastic strain was not used.

ANALYTICAL TEST MATRIX FOR PRACTICAL COLUMN SPECIMENS

After validating the finite element methodology, the practical column specimens were modeled and evaluated. A summary of the analytical test matrix for the practical column specimens analyzed is provided in Table 2. The nomenclature in Table 2 represents an "analysis set" of four specimens. For each analysis set, (1) one model was analyzed with no stiffeners near the concentrated load, (2) one was analyzed with concentric stiffeners, (3) one was analyzed

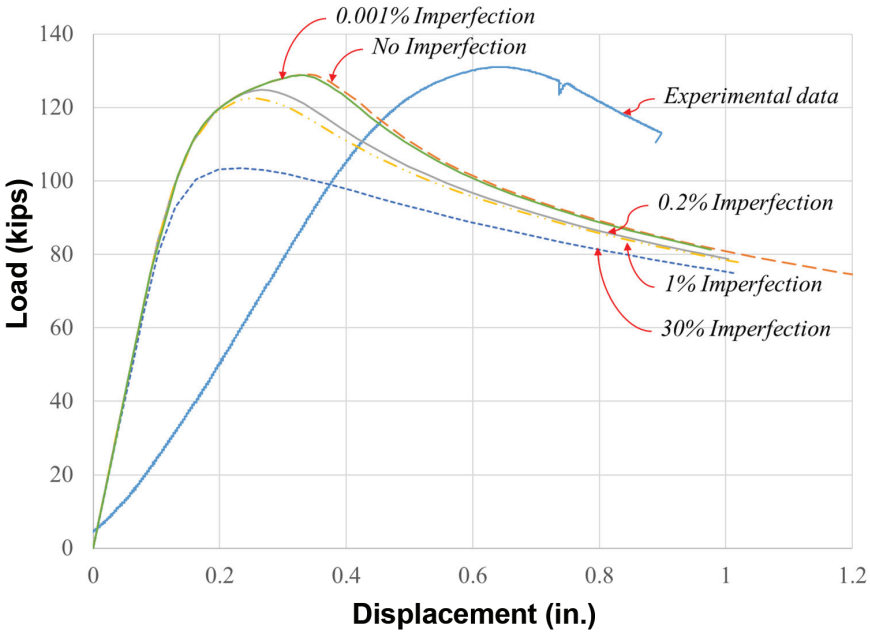

Fig. 6. Load-displacement comparison between experimental and analytical results for the W10×39 SC-NA column specimen.

Table 2. Analytical Test Matrix for Practical Column Sizes						
Nomenclature	**Test Method**	**Column Size**	**Stiffener t_s (in.)**	**Unsupported Length (ft)**	**Plate t (in.)**	**Weld (in.)**
W24×131 SC-⅜	Single Compression	W24×131	⅜	5	1	NA
W24×22 SC-⅜		W24×229	⅜	5	1	NA
W14×68 SC-⅜		W14×68	⅜	5	1	NA
W14×120 SC-⅜		W14×120	⅜	5	1	NA
W14×176 SC-⅜		W14×176	⅜	5	1	NA
W14×233 SC-⅜		W14×233	⅜	5	1	NA
W24×229 SC-¾		W24×229	¾	5	1	NA
W14×233 SC-¾		W14×233	¾	5	1	NA
W14×233 SC-¾(2)		W14×233	¾	**3.5**	1	NA
W24×131 DC-⅜	Double Compression	W24×131	⅜	NA	1	NA
W24×229 DC-⅜		W24×229	⅜	NA	1	NA
W14×68 DC-⅜		W14×68	⅜	NA	1	NA
W14×120 DC-⅜		W14×120	⅜	NA	1	NA
W14×176 DC-⅜		W14×176	⅜	NA	1	NA
W14×233 DC-⅜		W14×233	⅜	NA	1	NA
W24×131 DC-¾		W24×131	¾	NA	1	NA
W24×229 DC-¾		W24×229	¾	NA	1	NA
W14×68 DC-¾		W14×68	¾	NA	1	NA
W14×120 DC-¾		W14×120	¾	NA	1	NA
W14×176 DC-¾		W14×176	¾	NA	1	NA
W14×233 DC-¾		W14×233	¾	NA	1	NA
W24×131 ST-¼	Single Tension	W24×131	⅜	5	¾	¼
W24×229 ST-¼		W24×229	⅜	5	¾	¼
W14×68 ST-¼		W14×68	⅜	5	¾	¼
W14×120 ST-¼		W14×120	⅜	5	¾	¼
W14×176 ST-¼		W14×176	⅜	5	¾	¼
W14×233 ST-¼		W14×233	⅜	5	¾	¼
W24×131 ST-9⁄16		W24×131	⅜	5	1½	9⁄16
W24×22 ST-9⁄16		W24×229	⅜	5	1½	9⁄16
W14×68 ST-9⁄16		W14×68	⅜	5	1½	9⁄16
W14×120 ST-9⁄16		W14×120	⅜	5	1½	9⁄16
W14×176 ST-9⁄16		W14×176	⅜	5	1½	9⁄16
W14×233 ST-9⁄16		W14×233	⅜	5	1½	9⁄16
W24×131 ST-⅞		W24×131	⅜	5	2¼	⅞
W24×229 ST-⅞		W24×229	⅜	5	2¼	⅞
W14×68 ST-⅞		W14×68	⅜	5	2¼	⅞
W14×120 ST-⅞		W14×120	⅜	5	2¼	⅞
W14×176 ST-⅞		W14×176	⅜	5	2¼	⅞
W14×233 ST-⅞		W14×233	⅜	5	2¼	⅞

with stiffeners at a 2 in. eccentricity from the concentrated load, and (4) one was analyzed with stiffeners at a 4 in. eccentricity from the concentrated load. For each analysis set, Table 2 indicates the test type, the column size, the thickness of the stiffener, the unsupported length (one additional analysis set was performed with an unsupported length of 3.5 ft in lieu of 5 ft), the thickness of the loading plate(s), and the weld size used in the models for single tension tests.

The nomenclature of each analysis set includes the column size and the test method (SC for single compression, DC for double compression, and ST for single tension) along with an additional parameter, which depends on the test method. For the single tension tests, the additional parameter represents the weld thickness from the loading plate to the top flange of the column specimens. For double compression and single compression tests, the additional parameter represents the stiffener thickness. The nomenclature used for an individual model includes the nomenclature shown in Table 2 along with a representation of the stiffener eccentricity condition (NA for no stiffener, E0 for concentric stiffener, E2 for a 2-in. eccentricity, and E4 for a 4-in. eccentricity).

Table 2 shows the six practical column sizes selected for analytical investigations, including four W14 sizes. An increase in the flange thickness, decrease in the slenderness of the flange ($b_f/2t_f$), and decrease in the slenderness of the web (h/t_w) occur as the size (with respect to weight) of the W14 increases except for flange slenderness between the W14×120 and W14×68. This general trend in the W14 sections reflect an increase of "stockiness" for the specimens as their weight increases. Additionally, two W24 sections were modeled to represent shapes more commonly used in seismic areas or drift susceptible regions.

For the single tension tests, weld sizes of ¼ in., 9⁄16 in., and ⅞ in. were selected for the test matrix. Various weld sizes were analyzed since weld sizes proved to be an important testing parameter. Each weld size utilized a different loading plate thickness to ensure failure did not occur in the base metal before the weld.

Initially, the stiffener thickness was not thought of as a crucial parameter in the analytical studies because the primary focus of the research was to identify the change in effective capacity for eccentric stiffeners in lieu of concentric stiffeners, and it was believed that similar results would be obtained in identifying the percent changes, regardless of the stiffener thickness. There were no specific design loads, and therefore, the stiffeners were not designed using typical design equations. AISC *Specification* Section J10.8 (AISC, 2016) indicates that the thickness of the stiffener plate shall not be less than one-half the thickness of the loading plate. Because the loading plate was initially ¾ in. thick, a minimum stiffener thickness of ⅜ in. was initially selected for all models, which also matched the thickness of stiffeners used experimentally as described in Part 1: Experimental Studies (Alvarez Rodilla and Kowalkowski, 2021). However, results of some compression tests revealed that thin stiffeners might be more susceptible to buckling if concentric as opposed to eccentric. The results utilizing ⅜-in. stiffeners provided valuable results for some models but did not provide valuable results for all conditions, particularly when used in double compression tests for "stockier" members. An alternate stiffener size of ¾ in. was chosen to evaluate/validate the results and conclusions derived using ⅜-in. stiffeners.

ANALYTICAL FINITE ELEMENT BEHAVIOR

The following various screenshots from ABAQUS (2014) are provided to visualize observed model behavior herein.

Single Compression Models

All single compression column specimens *without stiffeners* reached their capacity when web crippling occurred within the web at a localized area under the applied load. Depending on the column size, significant yielding was also observed in the finite element model before crippling and contributed significantly to the mode of failure. Therefore, inelastic localized web crippling best describes the observed failure modes.

Generally, the maximum load for analytical column specimens *with concentric stiffeners* occurred when buckling took place in the stiffeners. In some cases, buckling of the stiffener was instantaneous and caused a sudden decrease in load (elastic stiffener buckling). Stiffener buckling for other column specimens occurred more gradually and after a significant amount of yielding occurred in the column specimen. The mode of stiffener buckling was dependent on the stiffener thickness and column size.

For modeled column specimens *with eccentric stiffeners*, the maximum load occurred when a combination of web local crippling and stiffener buckling/bending occurred. In some cases, significant yielding occurred in the stiffeners and the column specimen before reaching a maximum load and suggests that with practical column sizes, the stiffeners are more effective in sharing the concentrated load.

Figure 7 shows a screenshot of the W14×68 analytical model without stiffeners (W14×68 SC-NA) after web crippling occurred within the web. The contours represent the resultant magnitude of displacement at each point in the column specimen and demonstrate the out-of-plane displacement of the web with the vertical displacement of the loading plate. As soon as out-of-plane displacements occurred within the web, the load started to decrease gradually, indicating a buckling mode of failure occurred.

Figure 8 shows a screenshot of a W14×233 analytical model without stiffeners (W14×233 SC-NA) after web crippling occurred. Out-of-plane displacement is more concentrated toward the top flange for this column size. Also, the finite element model demonstrated more yielding prior to web crippling.

Figure 9 shows a finite element model for a W24×131 analytical model with concentric stiffeners (W24×131 SC-E0-⅜) and demonstrates that stiffener buckling eventually occurred directly under the concentrated load. The contours represent the von Mises stress magnitude at each point in the column specimen. Similarly, Figure 10 shows a finite element model of a W24×131 column specimen with stiffeners at an eccentricity of 4 in. (W24×131 SC-E4-⅜) and demonstrates how the stiffeners bend/buckle in combination with web local crippling.

Double Compression Tests

All double compression column specimens *without stiffeners* reached their capacity when sudden web compression buckling took place. The buckled shape of the web appeared as either one half-sine wave or two half-sine waves as shown in Figure 11 for a W14×68 column specimen (W14×68 DC-NA) and Figure 12 for a W14×120 column specimen (W14×120 DC-NA). Similar to single compression tests, for column sections with stockier webs, more yielding occurred before inelastic web compression buckling, and the out-of-plane deformation was not as significant as for members with thinner webs.

The maximum load for modeled column specimens *with concentric stiffeners* always took place when buckling occurred in the stiffeners. This buckling caused a sudden decrease in load for a given displacement. The results showed that with heavier (or stockier) column sections, ⅜-in. concentric stiffeners were more detrimental to the column specimen than the no-stiffener condition because buckling occurred suddenly before the web could properly distribute the load, as explained in more detail in Kowalkowski and Alvarez Rodilla (2019). Utilizing ¾-in. stiffeners always aided the capacity of the column specimen.

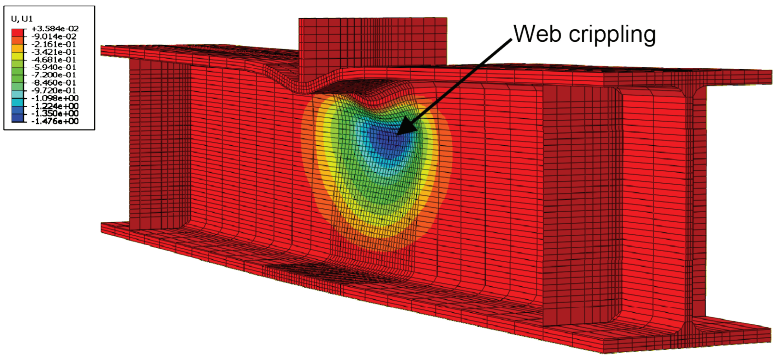

Fig. 7. Web local crippling that occurred in W14×68 SC-NA.

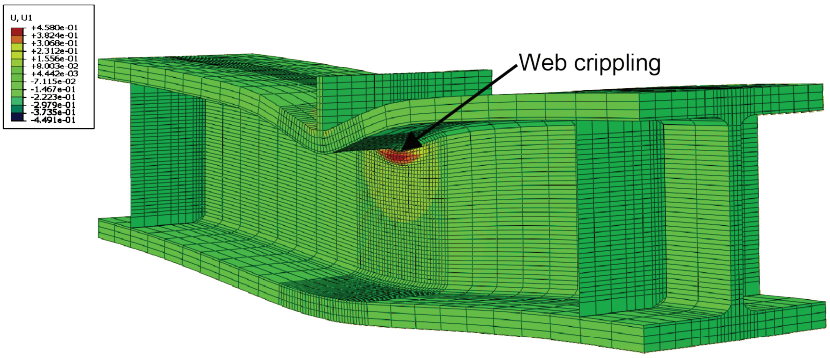

Fig. 8. Localized web local crippling that occurred in W14×233 SC-NA.

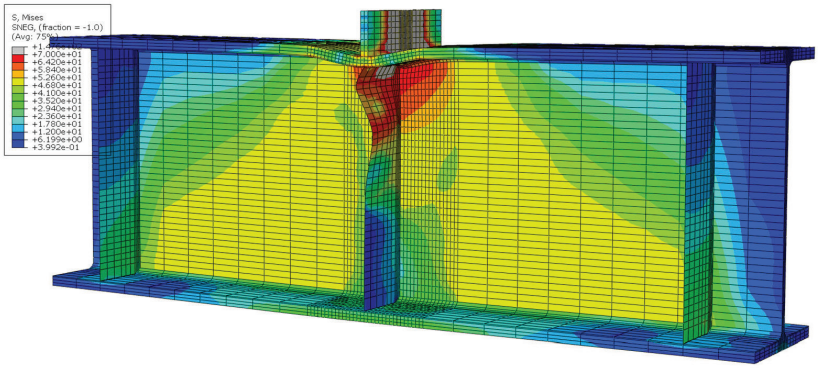

Fig. 9. Stiffener buckling that occurred for W24×131 SC-E0-⅜ (⅜-in. stiffeners).

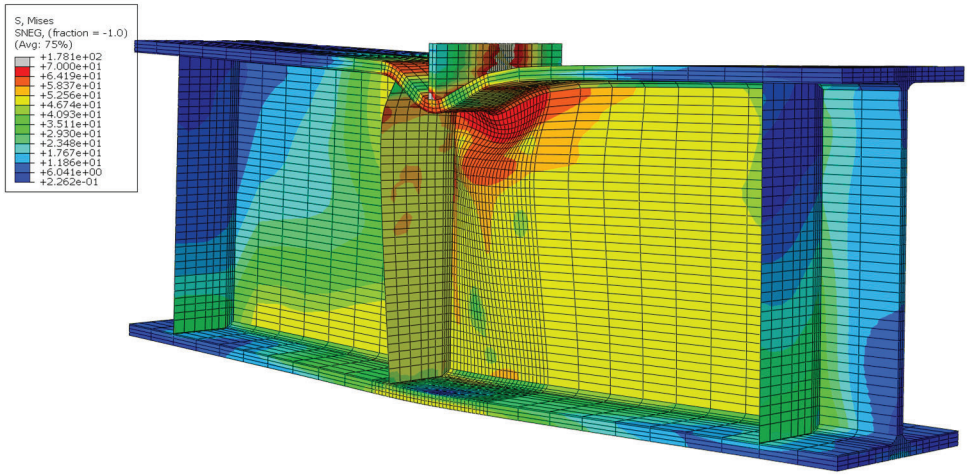

Fig. 10. Web local crippling combined with stiffener bending for W24×131 SC-E4-⅜.

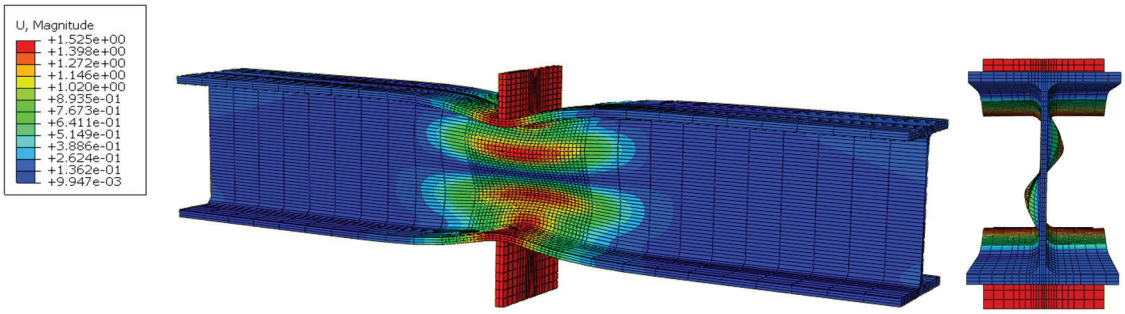

Fig. 11. Web compression buckling for column specimen W14×68 DC-NA.

Further, in some cases, yielding occurred in the stiffeners before stiffener buckling. Figure 13 shows a screenshot of a W14×131 model where the buckling of a ¾-in. concentric stiffener occurred.

For modeled column specimens *with eccentric stiffeners*, a combination of failure modes associated with the column specimen itself sometimes combined with bending of the stiffener generally controlled achieved capacity. In some cases, it appeared that eccentric stiffeners were more beneficial than concentric stiffeners since "sudden" buckling did not occur. Instead, the stiffeners started to develop curvature as deformations developed in the column specimen and still adequately braced the web from compression buckling. Figure 14 shows an example of a W24×131 column specimen modeled with ¾-in. stiffeners at an eccentricity of 4 in. (W24×131 DC-E4-¾). In this example, buckling of the web appeared to occur first as the limited load got transferred into the stiffeners at this eccentricity. As further deformations developed, more load was carried by the stiffeners until the stiffener buckled. This observed behavior is annotated on Figure 15, which shows the load-displacement results for all four modeled W24×131 column specimens together. As shown in Figure 15, the stiffeners at a 2-in. eccentricity were able to carry significant load prior to stiffener buckling. In this particular case, the maximum loads are very similar for the condition with concentric stiffeners and with stiffeners at a 2-in. eccentricity.

Single Tension Tests

The maximum load for the single tension finite element models was assumed to occur when the welds connecting the loading plate to the top flange reached the ultimate stress of 82.4 ksi at some location along the length of the weld. Calibration and verification of this process using experimental results and finite element models of the experimental column specimens is further described in Kowalkowski and Alvarez Rodilla (2019) and explained earlier in this paper. Each model was visually inspected in ABAQUS (2014) to identify when this occurs using the von Mises stresses distribution and setting the maximum limit to 82.4 ksi. Figure 16 shows a W24×131 column specimen

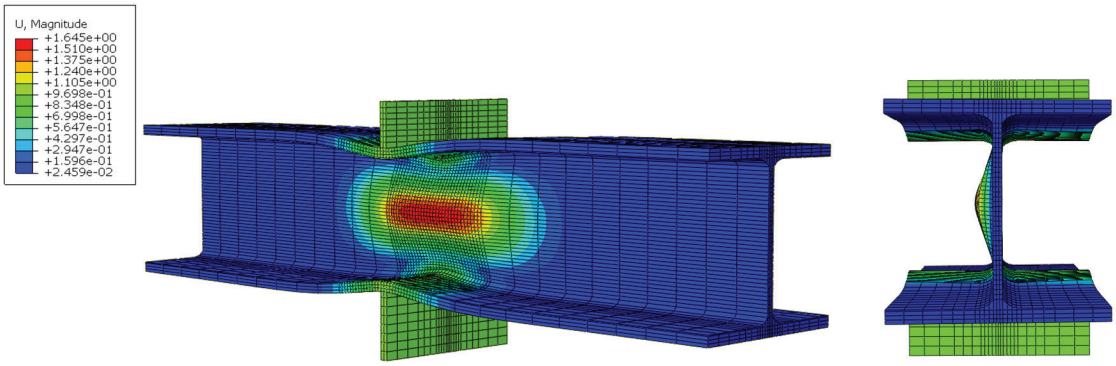

Fig. 12. Web compression buckling for column specimen W14×120 DC-NA.

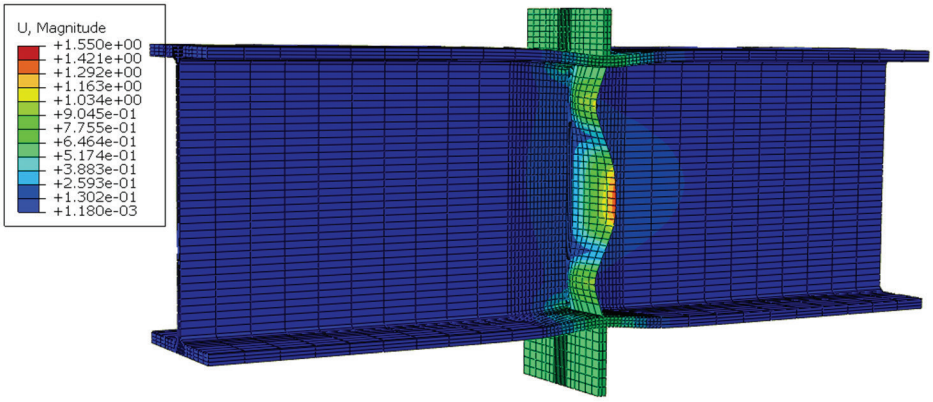

Fig. 13. Stiffener buckling that occurred for W24×131-DC-E0-¾.

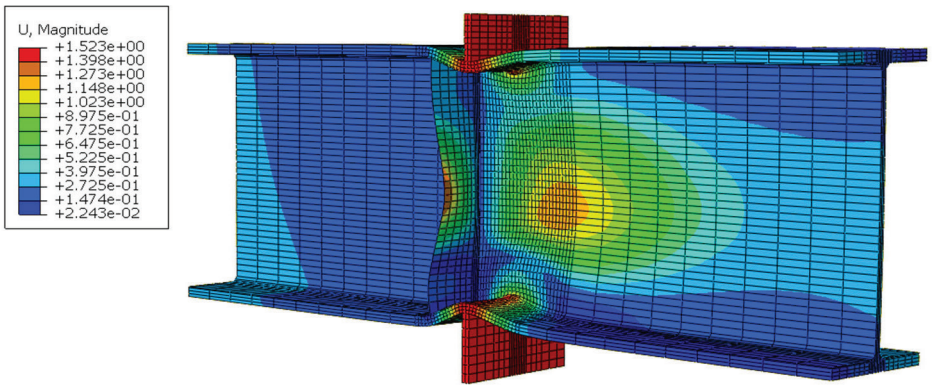

Fig. 14. Web compression buckling with stiffener buckling for W24×131 DC-E4-¾.

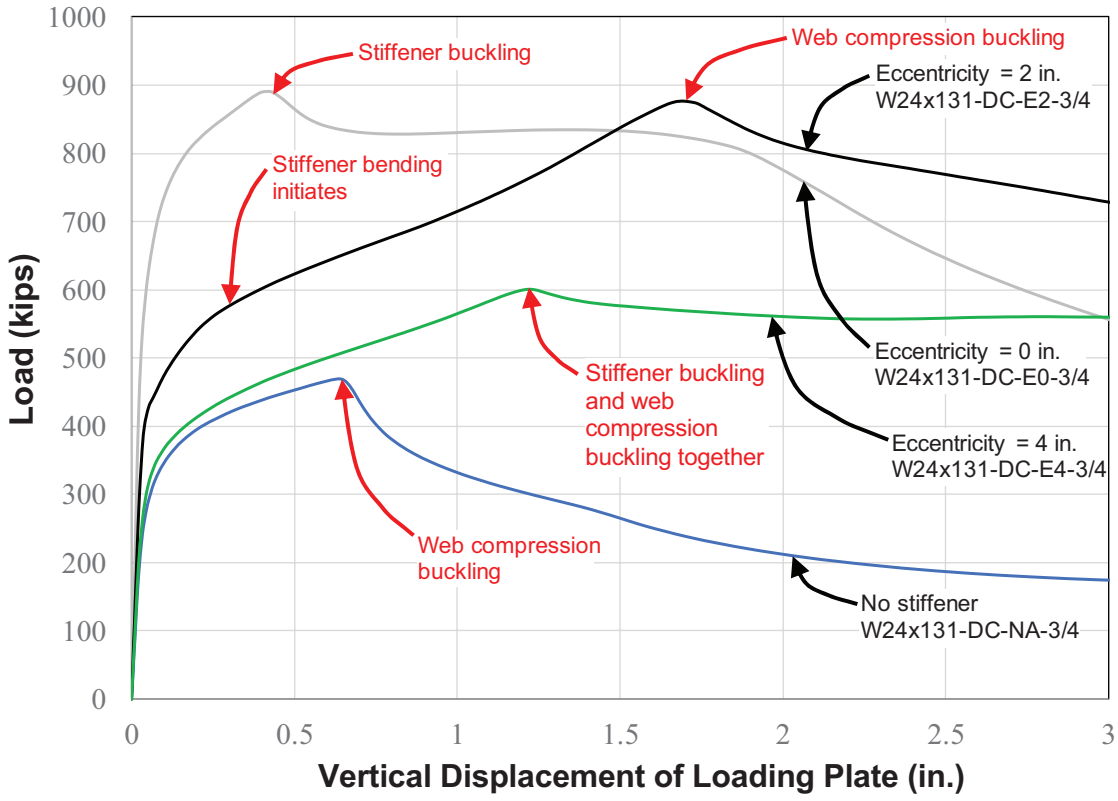

Fig. 15. Load-displacement results of W24×131 DC-¾ column specimens.

modeled with ¼-in. welds. Failure was assumed to occur in the top of the weld where it connects to the loading plate. Figure 17 shows a W24×131 column specimen modeled with ⅞-in. welds, and failure was assumed to occur at the bottom of the welds, where they connect to the column specimen flange. Note that in these figures, anything gray in the finite element models indicated an area where the Von Mises stress exceeded 82.4 ksi.

All column specimens modeled with ¼-in. welds reached an assumed failure load with a stress contour pattern similar to that shown in Figure 16. Also, larger column sections (e.g., W14×233 and W24×229) always reached an assumed failure load with contours similar to that shown in Figure 16, regardless of weld size. In limited conditions, the stress contours never exceeded the ultimate stress and, therefore, never demonstrated a failure in the weld. Rather, the column specimens exhibited significant displacements, and capacity was governed by the shear and flexural stresses that developed in the column specimen. This only occurred when ⅞-in. welds were modeled and stiffeners were at an eccentricity of 0 or 2 in.

In general, stress concentrations develop near the center of the weld along the length due to bending that occurred in the flanges. Near the center of the weld, the column section is stiffened by the fillet region and web adjacent to it, whereas near the edges of the weld, stiffness decreases because there is nothing adjacent below the flange. Therefore, less stress develops in the welds since the flanges locally displace vertically under the applied load. As the thickness of the flange increases and the slenderness of the flange decreases, the flange is less susceptible to develop local relative deformations. When stiffeners are present and adjacent to the weld, a load path exists to transfer force directly into the stiffeners, and the flanges are less prone to bend, allowing more force to develop at the connection since more uniform stresses develop in the weld.

For the single tension models, the influence of stiffener eccentricity on the maximum loads when failure of the welds was assumed to occur varied significantly for the different weld sizes. However, in all comparisons, as weld size increased and stiffener eccentricity decreased, the maximum load obtained when failure was assumed to occur

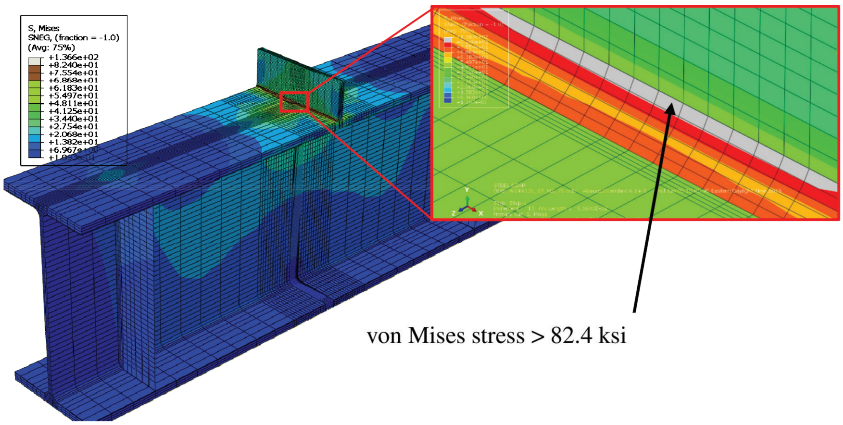

Fig. 16. Stress distribution assumed at "failure" for W24×131 ST-NA-¼.

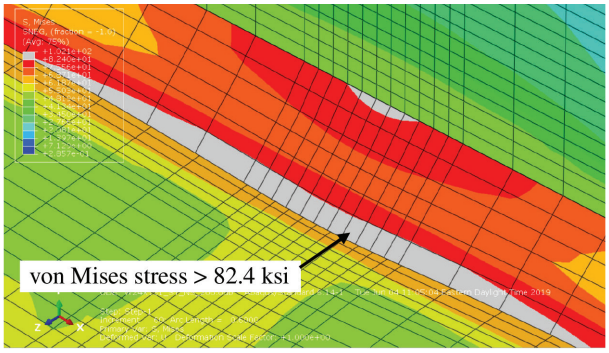

Fig. 17. Stress distribution at assumed "failure" for W24×131 ST-NA-⅞.

increased. Modeling larger sections with smaller weld sizes showed the influence of stiffener eccentricity is minimal because load-carrying capacities are all similar. Figure 18 shows the W24×229 column specimen modeled with ¼-in. welds and no stiffeners and at the assumed failure load. The stresses in the weld are fairly uniform across the width of the column. Analyzing the same column size with concentric stiffeners shows the weld stresses become slightly more uniform, but there is only a small change in the maximum load.

In general, as the column size decreased and the weld size increased, the influence of stiffener eccentricity became more pronounced because the capacity of the models became less governed by limitations in the weld strength itself. Rather, more localized deformations occurred in the flange causing nonuniform weld stresses. As stiffener eccentricity decreased, more uniform stresses occurred in the weld and allowed for achieving a greater capacity.

FINITE ELEMENT MODELS RESULTS AND DISCUSSION

Compression Models – Results and Discussion

Tables 3 and 4 show the theoretical nominal strengths (using AISC equations) and model results as they pertain to (1) achieved load capacity, listed as "maximum load" in the tables; (2) stiffener capacity, listed as "effective stiffener capacity" in the tables; and (3) the percentage of capacity provided by an eccentric stiffener compared to the concentric stiffener case, listed as "% concentric stiffener" (these three parameters are herein noted as "primary results" for single compression models and double compression models, respectively.) Tables 3 and 4 also provide general information for the finite element models, including the column size, the stiffener condition, and the stiffener thickness, *t*. The nominal strengths shown in the tables are for the applicable limit states using the AISC *Specification* (AISC, 2016), which includes web local yielding (WLY); web local crippling (WCR); and for double compression tests, web compression buckling (WCB).

For single compression models shown in Table 3, two larger column sizes, W14×233 and W24×229, were modeled with ¾-in. stiffeners. The double compression model results are only shown when utilizing ¾-in.-thick stiffeners in Table 4. Kowalkowski and Alvarez Rodilla (2019) described models implementing ⅜-in. stiffeners. The results with ⅜-in. stiffeners were inconsistent and did not relate well to the rest of the studies performed for the analytical investigations. Certain models utilizing ⅜-in. stiffeners behaved poorly as elastic buckling occurred in the stiffener before distribution of load into the web. In addition, a ⅜-in. stiffener thickness is small for compression conditions when utilizing AISC *Specification* Section J10.8 (AISC, 2016).

Note that evaluation of the concentrated load limit states in the AISC *Specification* (AISC, 2016) was not a primary focus of the research. However, the results presented in Tables 3 and 4, and for the single tension results shown later, demonstrate significant differences between the computed nominal capacities and the analytical results, and therefore question the accuracy of the equations in the AISC *Specification* (2016), particularly for the limit states of web compression buckling and flange bending.

The results in Table 3 demonstrate that the maximum loads obtained for single compression column specimens without stiffeners are close to the theoretical capacity for web local crippling when column specimens have more

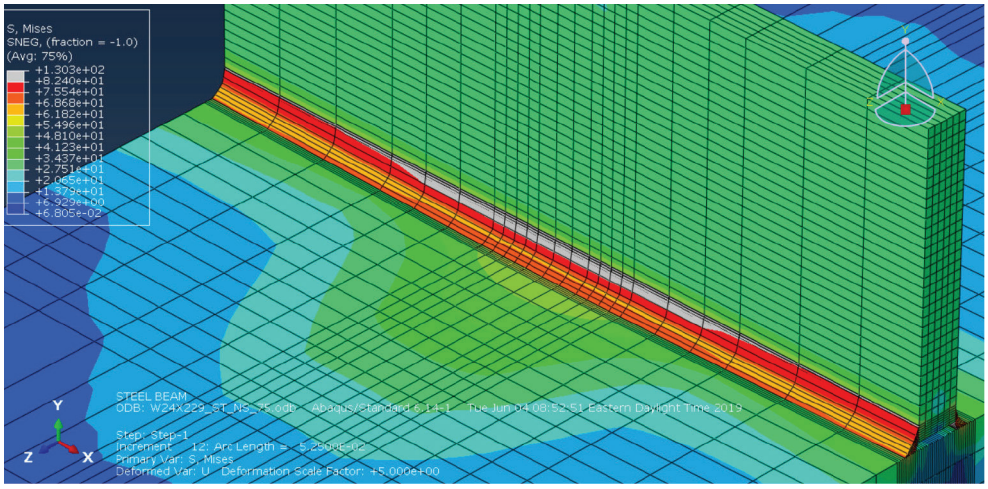

Fig. 18. Single tension model of W24×229 ST-NA-¼ at maximum assumed load.

Table 3. Primary Results for Single Compression Tests							
General Information			Nominal Strengths using 2016 AISC *Specification*		Primary Results		
Column Size	Stiffener Eccentricity (in.)	Stiffener *t* (in.)	WLY (kips)	WCR (kips)	Maximum Load (kips)	Effective Stiffener Capacity (kips)	% Concentric Stiffener
W24×131	NA	⅜	244	465	440	—	—
W24×131	0	⅜			676	236	—
W24×131	2	⅜			559	118	50.2
W24×131	4	⅜			503	62.5	26.5
W24×229	NA	⅜	571	1230	992	—	—
W24×229	0	⅜			1120	130	—
W24×229	2	⅜			1110	115	88.0
W24×229	4	⅜			1060	66.1	50.8
W24×229	NA	¾			992	—	—
W24×229	0	¾			1300	305	—
W24×229	2	¾			1200	210	68.8
W24×229	4	¾			1110	120	39.3
W14×68	NA	⅜	152	234	232	—	—
W14×68	0	⅜			336	104	—
W14×68	2	⅜			275	42.1	40.7
W14×68	4	⅜			235	2.90	2.80
W14×120	NA	⅜	249	456	404	—	—
W14×120	0	⅜			502	97.9	—
W14×120	2	⅜			465	61.0	62.3
W14×120	4	⅜			419	14.8	15.1
W14×176	NA	⅜	428	896	660	—	—
W14×176	0	⅜			754	94.5	—
W14×176	2	⅜			723	64.0	67.7
W14×176	4	⅜			693	33.9	35.9
W14×233	NA	⅜	508	1500	966	—	—
W14×233	0	⅜			1060	91.0	—
W14×233	2	⅜			1030	64.9	71.4
W14×233	4	⅜			1010	42.5	46.7
W14×233	NA	¾			966	—	—
W14×233	0	¾			1230	265	—
W14×233	2	¾			1120	152	57.6
W14×233	4	¾			1030	60.2	22.7

Table 4. Primary Results for Double Compression Tests								
General Info			Nominal Strengths using 2016 AISC *Specification*			Primary Results		
Column Size	Stiffener Eccentricity (in.)	Stiffener *t* (in.)	WLY (kips)	WCR (kips)	WCB (kips)	Maximum Load (kips)	Effective Stiffener Capacity (kips)	% Concentric Stiffener
W24×131	NA	NA	244	465	297	469	—	—
W24×131	0	¾				891	422	—
W24×131	2	¾				877	408	96.7
W24×131	4	¾				601	132	31.3
W24×229	NA	NA	571	1230	1190	1040	—	—
W24×229	0	¾				1480	437	—
W24×229	2	¾				1300	258	59.0
W24×229	4	¾				1290	253	57.8
W14×68	NA	NA	152	234	182	274	—	—
W14×68	0	¾				649	375	—
W14×68	2	¾				461	187	49.9
W14×68	4	¾				287	12.8	3.4
W14×120	NA	NA	249	456	520	476	—	—
W14×120	0	¾				854	378	—
W14×120	2	¾				777	301	79.7
W14×120	4	¾				593	117	31.0
W14×176	NA	NA	428	896	1450	850	—	—
W14×176	0	¾				1220	368	—
W14×176	2	¾				1160	311	84.4
W14×176	4	¾				995	145	39.4
W14×233	NA	NA	508	1500	2830	1280	—	—
W14×233	0	¾				1560	276	—
W14×233	2	¾				1670	388	140
W14×233	4	¾				1480	205	74.1

slender webs (W14×68 and W24×131). However, for the remaining column specimens, the maximum load was found between the theoretical capacities for web local yielding and web local crippling. The results in Table 4 indicate that for double compression specimens without stiffeners and with more slender webs (W14×68 and W24×131), the theoretical capacity for web compression buckling significantly underestimates the maximum load. In contrast, for column specimens with stockier webs (W14×120, W14×176, and W14×233), the capacity for web compression buckling overestimates the maximum load. Failure modes for stockier columns are best described as inelastic web compression buckling as described in Kowalkowski and Alvarez Rodilla (2019).

Comparisons between the maximum load obtained and web compression buckling are quite varied as demonstrated graphically in Figure 19. In Figure 19, CAP represents the maximum load capacity obtained in the finite element model for practical column sizes or experimentally for the sizes tested in the lab. The figure shows bar graphs to represent ratios of the theoretical limit states (WLY, WCB, and WCR) versus the maximum load capacity. Ratios less than 1.0 would indicate that the limit state equations are conservative with respect to design. Despite web compression buckling being the observed mode of failure in all analytical models (from the deformed shape), results in Figure 19 demonstrate that the maximum loads compare well to the limit state of web local crippling (ratio of WCR/CAP

always between 0.8 and 1.2). In addition, the maximum load is always consistently higher than the capacity for web local yielding. However, yielding was identified in all models, resulting in inelastic deformations that may be undesirable in the design of a beam-column joint.

Tables 3 and 4 show that the maximum load capacities for column specimens with stiffeners are always higher than the equivalent condition without stiffeners. However, for specimens with eccentric stiffeners, the "percent of concentric effective stiffener capacity" (shown as "% concentric stiffener" in the table) varies significantly, and the results are highly dependent on column size. As the column size increases, the percent of concentric effective stiffener capacity increases as well. For single compression tests, it was also observed that an increase in stiffener thickness increases the effective stiffener capacity regardless of the column size and the stiffener condition. The percent of concentric stiffener results are higher when ⅜-in. stiffeners are modeled in comparison to when ¾-in. stiffeners are modeled, even though the overall maximum loads obtained when ¾-in. stiffeners are modeled are always higher. Therefore, there are several parameters (various column properties and stiffener thickness) associated with identifying appropriate effective stiffener capacities of eccentric stiffeners. More details regarding the results and findings from the compression tests are provided in Kowalkowski and Alvarez Rodilla (2019).

Single Tension Models—Results and Discussion

All primary results of the single tension tests are provided in Tables 5, 6, and 7 for ¼-in., 9⁄16-in., and ⅞-in. welds, respectively. In the tables, the modified weld capacity for the finite element models assumes a uniform weld stress that can be obtained across the width as described in Kowalkowski and Alvarez Rodilla (2019). The tables show two different results: the "load results," which are equivalent to the results shown for single and double compression, and the "stiffness results," which are described herein. For the load results, the tables list the maximum load interpreted in each analysis (when weld failure is assumed to occur). For all cases with stiffeners, an analytical "effective stiffener capacity" is listed, which represents the difference between the maximum load obtained for that analysis and the result of the corresponding column specimen without stiffeners. The effective stiffener capacities of column specimens with eccentric stiffeners are shown as a percentage of the effective stiffener capacity of the corresponding analysis with concentric stiffeners. The tables show this percentage under the column labeled "% concentric stiffener capacity."

The process for determining when failure occurred in the weld was described earlier. However, the failure load was sensitive to how each increment of the finite element analysis was visually analyzed. Interpreting exactly when failure would occur was still questionable and small errors in this interpretation cause small errors in the primary results of this research. Due to the sensitivity of the results

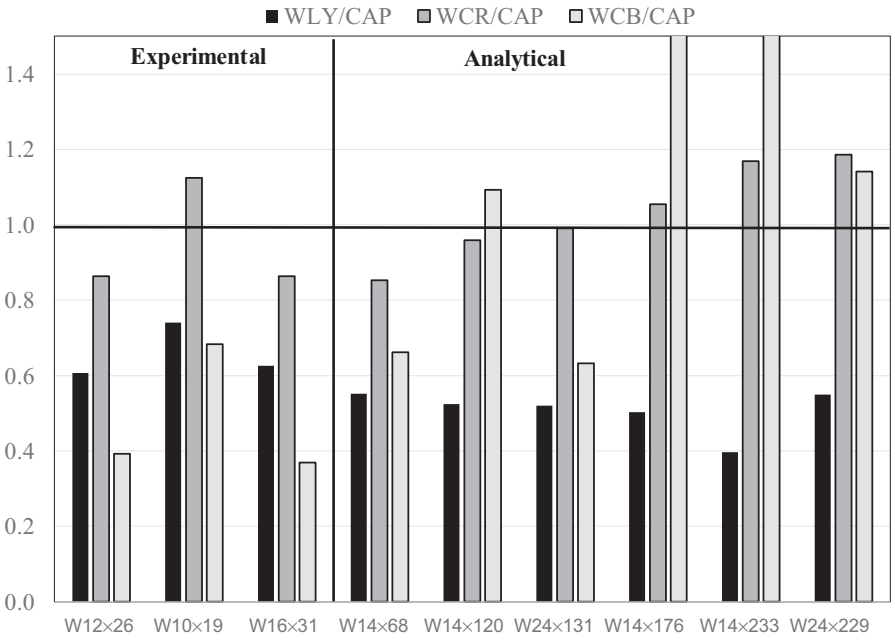

Fig. 19. Ratios of theoretical capacities vs. double compression test capacities.

Table 5. Primary Results of Single Tension Specimens Modeled with ¼-in. Welds								
			Load Results			Stiffness Results		
Column Size	Stiffener Condition	Modified Weld Capacity (kips)	Maximum Load (kips)	Effective Stiffener Capacity (kips)	% Concentric Stiffener Capacity	Stiffness (kips/in.)	Effective Stiffness (kips/in.)	% Concentric Stiffener Stiffness
W24×131	NA	260	216	—	—	4210	—	—
W24×131	E0	260	258	43.0	—	5510	1300	—
W24×131	E2	260	258	42.0	99.0	4900	692	53.3
W24×131	E4	260	235	20.0	47.0	4450	235	18.1
W24×229	NA	264	263	—	—	6800	—	—
W24×229	E0	264	264	0.50	—	7990	1190	—
W24×229	E2	264	263	0.20	30.0	7660	862	72.7
W24×229	E4	264	263	0.10	22.0	7230	426	35.9
W14×68	NA	201	159	—	—	2080	—	—
W14×68	E0	201	200	41.0	—	2320	244	—
W14×68	E2	201	191	31.0	76.0	2180	102	42.0
W14×68	E4	201	169	10.0	24.0	2100	23.0	9.60
W14×120	NA	296	221	—	—	3170	—	—
W14×120	E0	296	295	73.0	—	3610	437	—
W14×120	E2	296	291	69.0	94.0	3410	241	55.0
W14×120	E4	296	253	31.0	43.0	3250	82.0	18.8
W14×176	NA	316	284	—	—	4530	—	—
W14×176	E0	316	316	32.0	—	5110	579	—
W14×176	E2	316	314	31.0	96.0	4920	387	66.7
W14×176	E4	316	312	29.0	90.0	4700	173	29.8
W14×233	NA	320	318	—	—	5980	—	—
W14×233	E0	320	320	1.70	—	6660	682	—
W14×233	E2	320	319	1.50	87.0	6490	506	74.2
W14×233	E4	320	319	1.20	70.0	6240	265	38.9

with respect to the interpreted weld failure (e.g., very small effective stiffener capacities for W24×229 column specimen from Table 5), changes in the elastic stiffness were also evaluated. Herein, the "effective stiffener stiffness" represents the change in elastic stiffness when stiffeners are used in comparison to the elastic stiffness when stiffeners are not used. "Elastic stiffness" represents load divided by the displacement at the top of the loading plate. The displacement at the top of the loading plate considers flexural and shear deformations that occur in the column specimen, elastic elongation of the loading plate, and local deformations that occur in the column specimen from the concentrated load effect. If stiffeners are not present, more local deformations occur in the column specimen directly underneath the load due to the concentrated load effect. If concentric stiffeners are used, the local deformations are minimized, and therefore, a significantly higher elastic stiffness is expected. When eccentric stiffeners are used, the elastic stiffness results are between the corresponding values without stiffeners and concentric stiffeners. Therefore, an impression of how much of the applied load is shared by the stiffeners can be interpreted and compared to the concentric stiffener case.

In Tables 5, 6, and 7, the effective stiffener stiffness of column specimens with eccentric stiffeners is shown as a percentage of the effective stiffener stiffness of the corresponding model with concentric stiffeners. This is shown in the tables under the column labeled "% concentric stiffener

Table 6. Primary Results of Single Tension Specimens Modeled with 9/16-in. Welds								
			Load Results			Stiffness Results		
Column Size	Stiffener Condition	Modified Weld Capacity (kips)	Maximum Load (kips)	Effective Stiffener Capacity (kips)	% Concentric Stiffener Capacity	Stiffness (kips/in.)	Effective Stiffness (kips/in.)	% Concentric Stiffener Stiffness
W24×131	NA	584	402	—	—	5050	—	—
W24×131	E0	584	542	140	—	5980	939	—
W24×131	E2	584	513	111	79.1	5650	604	64.0
W24×131	E4	584	445	42.9	30.7	5270	221	24.0
W24×229	NA	593	590	—	—	8340	—	—
W24×229	E0	593	591	1.30	—	9350	1000	—
W24×229	E2	593	591	0.80	59.3	9110	765	76.0
W24×229	E4	593	590	0.70	50.3	8730	391	39.0
W14×68	NA	453	260	—	—	2260	—	—
W14×68	E0	453	325	65.2	—	2430	171	—
W14×68	E2	453	308	48.9	75.0	2360	102	60.0
W14×68	E4	453	275	15.5	23.7	2290	25.0	15.0
W14×120	NA	666	450	—	—	3500	—	—
W14×120	E0	666	621	172	—	3790	297	—
W14×120	E2	666	562	113	65.7	3700	205	69.0
W14×120	E4	666	485	35.7	20.8	3570	73	25.0
W14×176	NA	711	590	—	—	5050	—	—
W14×176	E0	711	700	109	—	5450	400	—
W14×176	E2	711	686	95.3	87.3	5350	293	73.0
W14×176	E4	711	652	61.8	56.7	5190	132	33.0
W14×233	NA	720	704	—	—	6750	—	—
W14×233	E0	720	717	12.3	—	7220	468	—
W14×233	E2	720	716	11.4	92.7	7120	364	78.0
W14×233	E4	720	715	10.4	84.9	6950	191	40.8

stiffness." As shown in the tables, there are clear trends in the result of percent of concentric stiffener stiffness. As column size increases and eccentricity decreases from 4 in. to 2 in., the percent of concentric stiffener stiffness increases. Therefore, the results of the elastic stiffness and effective elastic stiffness were found as beneficial when studying the effects of stiffener eccentricity as opposed to the maximum load.

The results in Tables 5, 6, and 7 demonstrate that the weld size and loading plate thickness significantly influence load carrying capacity within the model. The failure load always increased when the column size remained constant and only the weld size and loading plate thickness increased. Comparisons between the results and the limit states of flange bending and web local yielding are provided in Kowalkowski and Alvarez Rodilla (2019). The failure load results when using ¼-in. welds were often less than or close to the flange bending capacity and web local yielding capacities. However, incorporating ⅞-in. welds into the models significantly increased the analytical capacity in comparison to the limit state of flange bending and web local yielding. This observation demonstrates that the calculations for web local yielding and flange bending are not "true" capacities. However, weld failure is influenced

Table 7. Primary Results of ST Specimens Modeled with ⅞-in. Welds								
			Load Results			Stiffness Results		
Column Size	Stiffener Condition	Modified Weld Capacity (kips)	Maximum Load (kips)	Effective Stiffener Capacity (kips)	% Concentric Stiffener Capacity	Stiffness (kips/in.)	Effective Stiffness (kips/in.)	% Concentric Stiffener Stiffness
W24×131	NA	908	582	—	—	5470	—	—
W24×131	E0	908	772	190	—	6260	788	—
W24×131	E2	908	742	160	84.0	6130	655	83.0
W24×131	E4	908	666	84.3	44.0	5750	280	36.0
W24×229	NA	923	903	—	—	9040	—	—
W24×229	E0	923	916	12.6	—	9940	897	—
W24×229	E2	923	915	11.7	92.0	9800	766	85.0
W24×229	E4	923	913	9.8	77.0	9480	438	49.0
W14×68	NA	704	348	—	—	2390	—	—
W14×68	E0	704	436	88.1	—	2510	122	—
W14×68	E2	704	431	83.1	94.0	2500	113	93.0
W14×68	E4	704	400	51.6	59.0	2420	36.0	29.0
W14×120	NA	1040	613	—	—	3700	—	—
W14×120	E0	1040	678	65.1	—	3940	241	—
W14×120	E2	1040	674	61.1	94.0	3920	215	89.0
W14×120	E4	1040	661	48.2	74.0	3800	95.0	39.0
W14×176	NA	1110	855	—	—	5330	—	—
W14×176	E0	1110	994	139	—	5680	353	—
W14×176	E2	1110	979	124	89.0	5640	310	88.0
W14×176	E4	1110	930	75.0	54.0	5500	166	47.0
W14×233	NA	1120	1010	—	—	7190	—	—
W14×233	E0	1120	1100	82.6	—	7580	384	—
W14×233	E2	1120	1090	74.6	90.0	7530	338	88.0
W14×233	E4	1120	1060	50.9	62.0	7390	199	52.0

by the effects of flange bending. For instance, if concentric stiffeners are used, flange bending is minimized and higher loads are obtained. In addition, for a group of specimens of the same column size and weld thickness, the lowest failure load always resulted in the specimen without stiffeners, the second lowest in the specimen with stiffeners at a 4-in. eccentricity, the third with stiffeners at a 2-in. eccentricity, and the highest with concentric stiffeners. This research was limited to utilizing fillet welds, but similar trends in the results are expected if the column specimens were loaded with complete joint penetration welds. More research investigations are required to evaluate this assumption.

FORMULATION OF RECOMMENDATIONS BASED ON TEST RESULTS AND FINITE ELEMENT MODELING

Figure 20 represents a comprehensive output of the research to identify appropriate relationships between column section parameters and effective stiffener capacity that are valid or conservative for all test conditions (single tension, single compression, and double compression) and incorporates both experimental and analytical results. As described in Kowalkowski and Alvarez Rodilla (2019), relationships between the percent of concentric stiffener results and several column section properties were evaluated. These column section properties include the flange thickness, the

web slenderness (h/t_w), and the flange slenderness ($b_f/2t_f$). All of these properties contribute to the behavior and subsequent results within the study. However, the most critical and consistent property that influenced the results was the flange thickness, and therefore, final recommendations consider the flange thickness normalized with respect to the magnitude of eccentricity (e).

Figure 20 uses the eccentricity and flange thickness in the form of the e/t_f ratio and plots the results of this ratio versus. either the percent of concentric stiffener results in terms of elastic stiffness (analytical results only) or the percent of concentric stiffener results in terms of maximum capacity. Possible recommended design relationships are also shown in Figure 20. Single tension test results with ¼-in. welds were removed from the data sets in Figure 20 due to limitations of the weld strength, and the percent of concentric stiffener capacity results were sensitive to very small differences in maximum load obtained. Similarly, double compression results with ⅜-in. stiffeners were omitted for reasons described earlier.

Three possible design relationships between the e/t_f ratio and the percent of concentric stiffener results are shown in Figure 20. Data points compared include the experimental results of the study described in Part 1: Experimental Studies (Alvarez Rodilla and Kowalkowski, 2021), and results from the finite element models described in this paper. Three relationships between the data points were examined:

1. A straight-line linear expression, as shown by the gray line.
2. A more conservative parabolic equation (black line) similar to the straight-line equation and providing a maximum allowable e/t_f ratio of 5.0.
3. And the preferred parabolic equation that originates at 100% and provides a maximum e/t_f of 6.0 (red curve).

The third equation is preferred by the authors, but equations are shown for consideration of others to make design decisions. Both parabolic equations indicate that if the eccentricity is 0 in., the effective stiffener capacity is 100% that of the concentric stiffener case and are, therefore, logical. The development of the curves in Figure 20 is based on calibration to the current research. As such, no theoretical basis beyond observed data trends appears in the curves.

Reviewing the results in Figure 20 shows that only one data point falls significantly under the design relationships

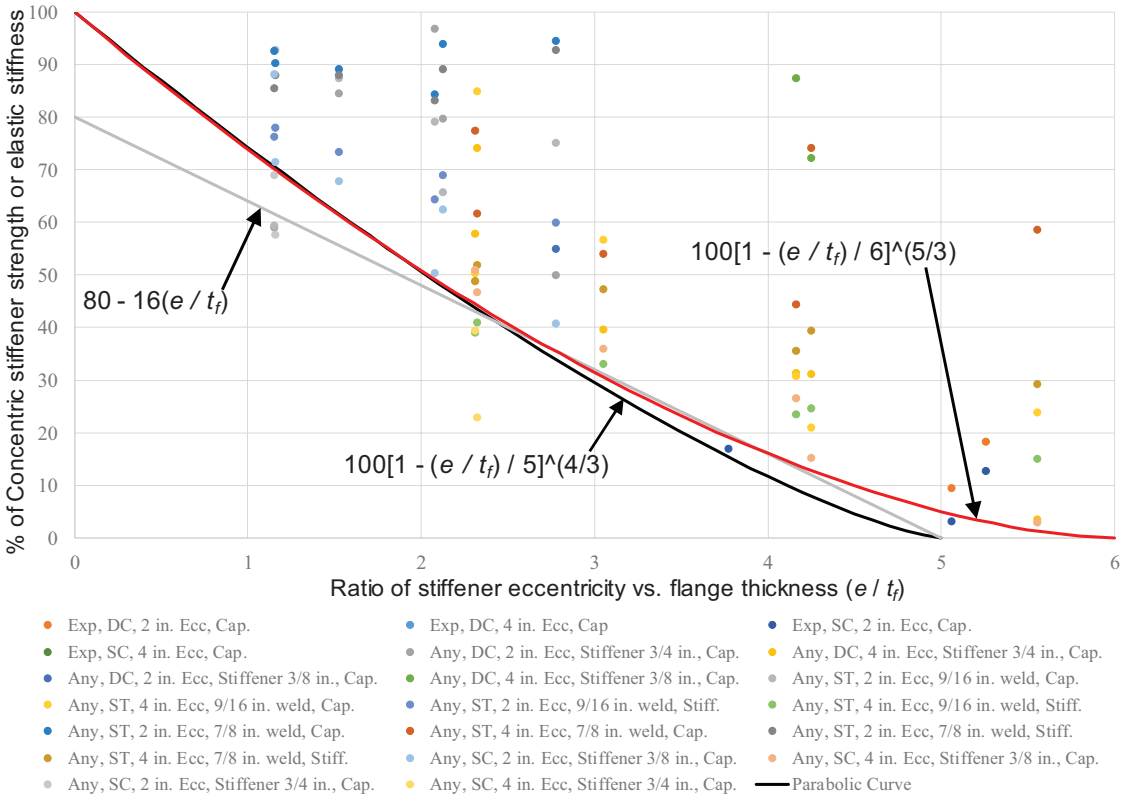

Fig. 20. All data used to define the relationship between e/t_f *and percent of concentric stiffener results.*

(at $e/t_f \approx 2.3$). This data point reflects the result of the analytical single compression test of the W24×229 column specimen modeled with ¾-in. stiffeners at an eccentricity of 4 in. This data point, based on careful review, is interpreted to be an outlier in the data, and all remaining comparisons fall above the recommended design relationships or very close to them.

CONCLUSIONS AND RECOMMENDATIONS

The following are the primary conclusions from the analytical investigations considering single compression, double compression, and single tension test results and the further studies presented in Kowalkowski and Alvarez Rodilla (2019).

- The equations in the AISC *Specification* (AISC, 2016) for the limit state of web local crippling compare favorably to the analytical finite element model results. Meanwhile, the equations for the limit state of web local yielding severely underestimate the capacity of column specimens subjected to concentrated loads.
- The equation for the limit state of web compression buckling is inconsistent compared to the capacity found in the finite element models considering double compression loading, even though this was the mode of failure identified in the finite element models for all column specimens without stiffeners.
- The recommended eccentric capacity calculations included in AISC Design Guide 13 (Carter, 1999) do not appear to properly identify the effective stiffener capacity of eccentric stiffeners for the cases considered in this research.
- This research shows that the effective stiffener capacity of eccentric stiffeners is dependent on several factors, including:
  1. The type of applied loading (single compression, double compression, or single tension).
  2. Column dimensions such as flange and web thickness, slenderness ratios, and overall cross-sectional size.
  3. Weld sizes, with respect to the single tension condition, for the component pulling on the column flange.
  4. Stiffener thickness and magnitude of eccentricity.
- The number of variables are many, but determining the effective stiffener capacity can conservatively be simplified using the flange thickness and magnitude of eccentricity.

From this research, recommendations for computing the final effective stiffener capacity, R_{n_eff}, are provided herein. The capacity assumes that a pair of full-depth transverse stiffeners are provided. Also, the effective stiffener capacity calculated utilizes the preferred parabolic function shown in Figure 20 (red line). The following design recommendations for stiffeners used within moment connections of beams connecting to column flanges are:

- When a column specimen is subjected to a single or double concentrated compression load, it is recommended that stiffeners pass the slenderness limit in Equation 1:

$$\lambda_s = \frac{b_s}{t_s} \le 0.56\sqrt{\frac{E}{F_{ystiff}}} \tag{1}$$

- For the following conditions, based on limitations and observations in this research, eccentric stiffeners shall have no effective stiffener capacity, $R_{n\_eff} = 0$, if any of the following criteria are met:
  - If the eccentricity, e, is greater than 4 in.
  - If the flange thickness, t_f, is less than 0.5 in.
  - If the ratio of e/t_f is greater than 6.0.
- Assuming the preceding conditions do not apply, the effective stiffener capacity of eccentric stiffeners is computed using Equation 2.

$$R_{n\_eff} = R_{n\_c}\left(1 - \frac{e/t_f}{6}\right)^{5/3} \tag{2}$$

where

R_{n_c} = stiffener capacity in the concentric case using acceptable methods, kips

e = actual stiffener eccentricity, in.

LIMITATIONS

The recommendations provided are limited to the largest cross section examined in this research and should be reviewed using additional section sizes and stiffener sizes and depths. Eccentricities greater than 4 in. could be evaluated for larger column sizes. Analysis should be performed with single tension tests, assuming that the loading plates are attached to the column using complete joint penetration welds.

ACKNOWLEDGMENTS

This research was sponsored by the American Institute of Steel Construction (AISC) and conducted using the laboratory facilities of Lawrence Technological University (LTU). The data compilation and report preparation were supported by the Department of Civil and Architectural Engineering and LTU, and all DIC data from Part 1: Experimental

Studies (Alvarez Rodilla and Kowalkowski, 2021) was processed in collaboration to the Department of Mechanical Engineering at LTU.

REFERENCES

ABAQUS (2014), *ABAQUS/Standard User's Manuals*, Version 6.14, Dassault Systems, 2014.

AISC (2017), *Steel Construction Manual*, 15th Ed., American Institute of Steel Construction, Chicago, Ill.

AISC (2016), *Specification for Structural Steel Buildings*, ANSI/AISC 360-16, American Institute of Steel Construction, Chicago, Ill.

Alvarez Rodilla, J. and Kowalkowski, K.J. (2021), "Determination of Capacities of Eccentric Stiffeners Part 1: Experimental Studies," *Engineering Journal*, AISC, Vol. 58, No. 2, pp. 79–98.

ASTM (2009), *Standard Test Methods for Tension Testing of Metallic Materials*, ASTM E8/E8M-09, ASTM International, West Conshohocken, Pa.

Bowman, M.D. and Quinn, B.P. (1994), "Examination of Fillet Weld Strength," *Engineering Journal*, AISC, Vol. 31, pp. 98–108.

Carter, C.J. (1999), *Stiffening of Wide-Flange Columns at Moment Connections: Wind and Seismic Applications*, Design Guide 13, AISC, Chicago, Ill.

Graham, J.D., Sherbourne, A.N., and Khabbaz, R.N. (1959), "Welded Interior Beam-to-Column Connections," Report for AISC, Chicago, Ill.

Kartal, M., Molak, R., Turski, M., Gungor, S., Fitzpatrick, M.E., and Edwards, L. (2007), "Determination of Weld Metal Mechanical Properties Utilizing Novel Tensile Testing Methods," *Applied Mechanics and Materials*, Vols. 7–8, pp. 127–132.

Kowalkowski, K.J. and Alvarez Rodilla, J. (2019), "Analysis and Design of Eccentric Stiffeners Part of Moment Connections to Column Flanges," Final Report for AISC, Chicago, Ill.

Norwood, J. (2018), "Effect of Continuity Plate Eccentricity on the Performance of Welded Beam-to-Column Connections," Master's Thesis, Department of Civil Engineering, University of Arkansas, Fayetteville, Ark.

Sherbourne, A.N. and Murthy, D.N.S. (1978), "Computer Simulation of Column Webs in Structural Steel Connections," *Computers and Structures*, Vol. 8., May, pp. 479–490.

Design by Advanced Elastic Analysis: An Investigation of Beam-Columns

YUNFEI WANG and RONALD D. ZIEMIAN

ABSTRACT

At the heart of the provisions for assessing structural stability within the AISC *Specification for Structural Steel Buildings* is the direct analysis method. The fundamental concept for this method is that the more behavior is explicitly modeled within the analysis, the simpler it is to define the AISC *Specification* design requirements. In other words, the direct analysis method consists of calculating strength demands and available strengths according to a range of well-defined and fairly detailed analysis requirements. This paper begins with an overview of two logical extensions to AISC's direct analysis method, both of which are now provided in AISC *Specification* Appendix 1, Design by Advanced Analysis. In establishing these approaches, many systems were investigated in previous research, and it was noted that systems with beam-columns subject to minor-axis bending may deserve additional attention. This paper presents a detailed study that investigates such members, as well as members subject to major-axis bending.

Keywords: direct analysis method, design by advanced analysis, design by advanced elastic analysis, beam-column, AISC, steel design.

INTRODUCTION

For the past 60 years, the effective length method (ELM) has been a widely employed stability design method (Ziemian, 2010). By scaling actual unbraced lengths to effective lengths when calculating the available strengths of compression members, the effective length *K*-factor is assumed to account for most factors known to impact the stability of structural systems, including geometric system imperfections; stiffness reduction due to inelasticity; and, to a much lesser degree, uncertainty in strength and stiffness (AISC, 2016b). In 2005, design by the direct analysis method (DM) first appeared in the AISC *Specification for Structural Steel Buildings* (AISC, 2005), hereafter referred to as the AISC *Specification*. In DM, the available strengths of compression members are based simply on the unbraced length ($K = 1$), as long as system imperfections (but not member imperfections) and stiffness reduction due to inelasticity are represented in the structural analysis. Since then, many in the structural design profession have moved from employing ELM to DM. As a result, DM was relocated in the 2010 AISC *Specification* (AISC, 2010) from Appendix 7 to Chapter C, while ELM was relocated from Chapter C to Appendix 7.

Yunfei Wang, Gilsanz Murray Steficek, New York, N.Y. Email: phoebe.wang@gmsllp.com

Ronald D. Ziemian, Bucknell University, Civil and Environmental Engineering Department, Lewisburg, Pa. Email: ziemian@bucknell.edu (corresponding)

Paper No. 2019-19

Both design methods rely on establishing the unbraced lengths of compression members, which in some cases may be difficult, if not impossible, to define. Examples include, but are not limited to, arches, tree columns, and Vierendeel trusses. In response to this predicament, AISC introduced the design by advanced elastic analysis method that appears in the 2016 AISC *Specification* in Appendix 1. In addition to the analysis modeling requirements of DM, the method further requires the direct modeling of member imperfections and, therefore the method is often represented by the acronym DMMI. In applying this approach, engineers can avoid the complexities of defining unbraced lengths, thereby being permitted to compute the nominal available strengths of compression members as their axial cross-sectional strengths. This paper reports on a study to complement previous studies on systems to evaluate the performance of DMMI (Nwe Nwe, 2014; Giesen-Loo, 2016), especially with an eye toward members that are subject to the combination of compression and minor-axis bending (Wang, 2018; Wang and Ziemian, 2019). Using AISC's design by advanced inelastic analysis method, which is based on employing a rigorous geometric and material nonlinear analysis with imperfections (GMNIA), the accuracy of DMMI is assessed and further compared with the more traditional ELM and DM design methods. Additionally, the significances of thermal residual stresses, which are a consequence of uneven cooling of rolled cross sections, and the axis of bending (minor versus major) for W- and HSS shapes are also explored.

The paper begins by providing an overview of AISC's ELM, DM, DMMI, and GMNIA methods, along with details of the analysis method and the interaction equation employed in each. Results of the study are then presented

primarily in tabular format, which are followed by discussions of the effects of residual stresses, axis of bending, and design method employed.

OVERVIEW OF DESIGN METHODS

In this study, the ends of simply supported columns of various slenderness ratios are subjected to a wide range of combinations of applied axial force and bending moments that are of equal magnitude and opposite direction (in the absence of axial force, such moments would produce a uniform moment distribution). In all cases, the members are assumed to be fully braced out-of-the-plane of bending. To assess the LRFD strength of beam-columns based on an elastic analysis, the following interaction equations are provided in the AISC *Specification* (from *Specification* Equations H1-1a and H1-1b):

$$\frac{P_u}{\phi P_n}+\frac{8}{9}\left(\frac{M_{ux}}{\phi M_{nx}}+\frac{M_{uy}}{\phi M_{ny}}\right)\le 1.0 \quad \text{for } P_u/\phi P_n \ge 0.2 \quad (1a)$$

$$\frac{P_u}{2\phi P_n}+\left(\frac{M_{ux}}{\phi M_{nx}}+\frac{M_{uy}}{\phi M_{ny}}\right)\le 1.0 \quad \text{for } P_u/\phi P_n < 0.2 \quad (1b)$$

where $\phi = 0.90$, P_u is the required axial strength, M_u is the required flexural strength, P_n is the nominal available axial strength, and M_n is the nominal available flexural strength about either the major x- or minor y-axis. The analysis for the required axial strength, P_u, and flexural strength, M_u, should consider second-order (geometric nonlinear) effects.

The following design methods, including ELM, DM, and DMMI, employ Equations 1a and 1b with terms defined by that specific method. In all cases, the controlling combinations of axial force and bending moment are determined for each of these elastic design methods by iteratively solving for the maximum value of M_u for a given value of P_u that will satisfy Equation 1. For reference, Figure 1 shows the deflected shape of the beam-column. Equilibrium on the deformed shape is given by:

$$M_u(x,P)+Pv(x)+M=0 \quad (2)$$

After substituting the moment-curvature relationship, $M_u(x,P)=EId^2v/dx^2$, Equation 2 becomes the governing differential equation:

$$EI\frac{d^2v}{dx^2}+Pv(x)=-M \quad (3)$$

where $v(x)$ is the total lateral deflection as a function of span length location x and equals the sum of an assumed geometric imperfection $v_0(x)=\delta_0\sin\frac{\pi x}{L}$ and deflection $v_{PM}(x)$ due to the applied combination of P and M.

Effective Length Method (ELM)

In computing the nominal axial strength, P_n, from the AISC column curve, the effective length factor of a simply supported beam-column is $K = 1$. In determining the required flexural strength, M_u, equilibrium equations are

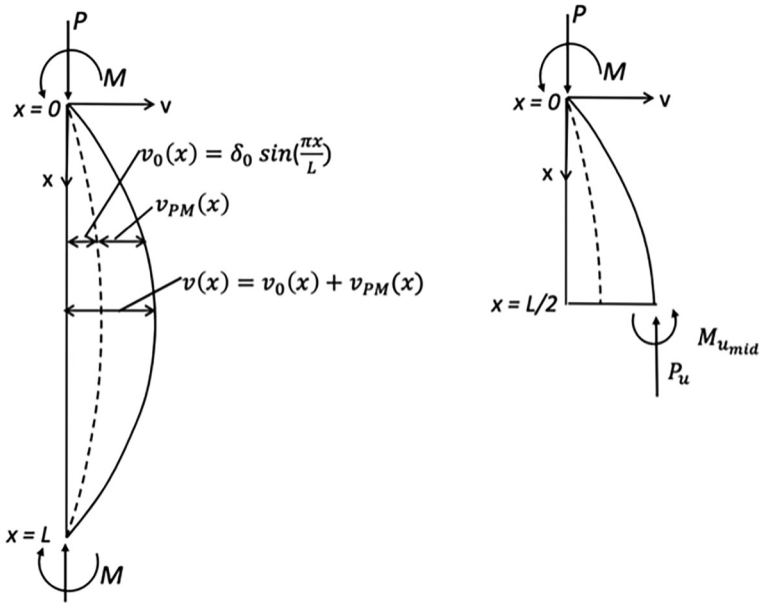

(a) Deflection diagram *(b) Free-body diagram at mid-height*

Fig. 1. Deflected shape of beam-column with second-order effects due to applied loading and geometric imperfection.

defined on the deflected shape to account for second-order effects. For a structural analysis associated with ELM, the beam-column is assumed geometrically straight, $v_0(x) = 0$, prior to any applied loading (the AISC column curve accounts for member out-of-straightness). As a result, the P-δ effect in this method need only account for the interaction between the applied axial load and bending moments and, thereby, is not influenced by the presence of an initial member imperfection.

In establishing the design adequacy of this member, the required moment, $M_u(x,P)$, is a maximum at midspan because $v_{PM}(x)$ takes on a maximum value when $x = L/2$. Thus, the interaction equation only needs to be checked at midspan, where the required strengths (terms in the numerators of Equation 1) are at a maximum. For an elastic analysis of a simply supported, originally perfectly straight, and prismatic member, the required flexural strength, M_u, at midspan, which includes moment amplification due to second-order effects, can be calculated as a function of the applied force P and moment M by the following "exact" equation (McGuire et al., 2000):

$$\left|M_{u_{mid}}\right| = \frac{M}{\cos\left(\frac{\pi}{2}\sqrt{\frac{P}{P_e}}\right)} \tag{4}$$

where P_e is the Euler buckling strength of the beam-column, and noting that shear deformation is neglected.

With $P_u = P$ at midspan, substitution of these terms for P_u and $M_u = \left|M_{u_{mid}}\right|$ in Equation 1a results in an interaction equation for ELM defined by:

$$\frac{P}{\phi P_n} + \frac{8}{9}\left[\frac{\frac{M}{\cos\left(\frac{\pi}{2}\sqrt{\frac{P}{P_e}}\right)}}{\phi M_n}\right] \le 1.0 \tag{5}$$

in which, specific to ELM,

$$P_n = F_{cr}A_g$$

$$P_e = \frac{\pi^2 EI}{L^2}$$

$$M_n = F_y Z$$

where F_{cr} is the critical buckling stress as defined by the AISC column curve, with $K = 1$ for the simply supported end conditions being investigated in this study; A_g is the gross area of the cross-section; E is the elastic modulus of the material; I is the moment of inertia; L is the unsupported length of the beam-column; F_y is the material yield stress; and Z is the plastic section modulus. In computing M_n, it is important to note that only members with compact sections are investigated, and any members subject to major-axis bending are assumed fully braced out-of-plane.

Direct Analysis Method (DM)

Although DM permits the use of the unbraced length ($K = 1$), this provides no advantage over ELM for the specific end support conditions of the single beam-column investigated in this study. In fact, DM is somewhat penalized in this case by its required use of a stiffness reduction factor within the structural analysis. Although the equilibrium analysis is of the same form as that given for ELM, the Euler buckling strength, P_e, used in the analysis of the member is modified to represent the inelastic buckling strength of the member. As a result, the interaction equation (Equation 1a) for DM can be written as Equation 5, except P_e is defined as the inelastic buckling strength. Hence, $P_n = F_{cr}A_g$, defined by the AISC column curve with no $0.8\tau_b$ stiffness reduction on E; $P_e = \pi^2(0.8\tau_b E)I/L^2$, which amplifies the moment; and $M_n = F_y Z$. The $0.8\tau_b$ stiffness reduction is not used in computing F_{cr} because the AISC column curve already has a stiffness reduction included. According to the AISC *Specification* (2016b) and given that all sections are compact, τ_b is calculated as:

$$\tau_b = 4\left(\frac{P}{P_y}\right)\left[1-\left(\frac{P}{P_y}\right)\right] \text{ for } \frac{P}{P_y} > 0.5 \tag{6a}$$

$$\tau_b = 1 \text{ for } \frac{P}{P_y} \le 0.5 \tag{6b}$$

where $P_y = F_y A_g$.

Design by Advanced Elastic Analysis Method (DMMI)

As described earlier, DMMI is an alternative design method that may be particularly useful for more complex structures in which the unbraced length is not discernible. By directly modeling member out-of-straightness and representing potential inelasticity through the use of the stiffness reduction strategy employed in DM, the nominal axial strength, P_n, of the member may be taken as its cross-section strength. The resulting increase in axial strength, P_n, that appears in the interaction equation is compensated for by a larger required flexural strength, M_u, which is obtained from an advanced elastic structural analysis that accounts for initial system and member imperfections, second-order (geometric nonlinear) effects, and stiffness reduction due to inelasticity.

In contrast to the preceding analysis for determining strengths for ELM and DM, the analysis for DMMI must also include the direct modeling of member out-of-straightness. In this study, the shape of the initial imperfection is assumed a sine wave with an amplitude at midspan of $\delta_0 = L/1000$ per the AISC *Code of Standard Practice for Steel*

Buildings and Bridges (AISC, 2016a). As such, the second-order P-δ effect needs to include both the impact of the applied axial force and bending moment as well as the initial imperfection.

The solution to the governing differential equation, Equation 3, has a solution at midspan that is given by:

$$v\left(\frac{L}{2}\right)=\frac{\delta_0}{1-\frac{P}{P_e}}+\frac{M}{P}\left[\frac{2\sin\left(\sqrt{\frac{P}{P_e}}\frac{\pi}{2}\right)-\sin\left(\sqrt{\frac{P}{P_e}}\pi\right)}{\sin\left(\sqrt{\frac{P}{P_e}}\pi\right)}\right] \quad (7)$$

With $v(L/2)$, equilibrium on the deformed shape at midspan will result in a required moment strength of:

$$\left|M_{u_{mid}}\right| = M + Pv\left(\frac{L}{2}\right) \quad (8)$$

This solution is more complex than Equation 4 because the initial imperfection is not zero and contributes to the second-order effects.

Similar to DM, a stiffness reduction factor of $0.8\tau_b$ should be applied to all the members of the system, which in this study means that all EI terms (within P_e) in the previous equations should be $0.8\tau_b EI$. With values of $P_u = P$ and $M_u = \left|M_{u_{mid}}\right|$ as defined previously, the interaction equation (Equation 1a) is expressed for DMMI as:

$$\frac{P}{\phi P_n}+\frac{8}{9}\left[\frac{M+Pv\left(\frac{L}{2}\right)}{\phi M_n}\right]\le 1.0 \quad (9)$$

in which, specific to DMMI, $v(L/2)$ is determined by Equation 7 with $\delta_0 = L/1000$ and P_e and τ_b as defined for DM, $P_n = F_y A_g$, and $M_n = F_y Z$.

Design by Advanced Inelastic Analysis Method (GMNIA)

Since 2010, the design by advanced inelastic analysis method has been provided in AISC *Specification* Appendix 1. Given that this design method is based on a geometric and materially nonlinear analysis that includes initial imperfections, it will be referenced by the acronym GMNIA. The second-order inelastic analysis routines used in this study are included in the finite element analysis software FE++ (Alemdar, 2001) for W-shapes and STRAND7 for HSS, where distributed plasticity models are employed. In FE++, each beam-column is modeled by eight line elements, thereby permitting a sine wave member out-of-straightness of $\delta_0 = L/1000$ to be directly modeled in the analysis. Residual stresses are represented by pre-stressing (compression or tension) the fibers that define the cross section. In STRAND7, however, shell elements are used to model the beam-columns, and similarly for FE++, member out-of-straightness and residual stresses are directly modeled. In both analysis programs, the applied axial force P and bending moments M are applied simultaneously, and an incremental-iterative arc-length solution scheme is employed until a limit point is achieved. Because of the relatively high accuracy of these analyses, the following error analyses of the preceding elastic design methods are based on the combinations of P and M that this inelastic design method would permit and still satisfy the provisions of AISC *Specification* Appendix 1.

It is well known that partial yielding of the cross section can have a significant effect on the stability of beam-columns. In cases where member out-of-straightness is not removed by processes, such as rotary straightening, this partial yielding can be accentuated by the presence of residual stresses. On the other hand, the use of such straightening processes can be shown to alleviate or even eliminate the presence of residual stresses (Ge and Yura, 2019). As a result, ultimate strength combinations were determined for cases in which residual stresses are and are not included in the analysis of elastic-perfectly plastic material models. When residual stresses are taken into account, the Galambos and Ketter (1959) residual stress distribution was employed for the W-shapes with a maximum compressive stress at the flange tips of $0.3F_y$. For the HSS-shapes, two residual stress patterns were considered. The Mathur (2011) residual stress pattern was employed to represent the highest expected residual stress pattern, with a maximum compressive strength of 20 ksi at the center of each face. A much lower and perhaps more realistic European Convention for Constructional Steelwork (ECCS, 1984) residual stress pattern with $0.2F_y$ at the center of each face was also studied. It is noted that the use of the Mathur pattern is considered conservative because it was developed for welded box columns. Additionally, the material elastic modulus, E, and yield stress, F_y, in the FE++ and STRAND7 analyses are reduced by a factor of 0.90, as required by AISC *Specification* Appendix 1.

NORMALIZED *P-M* INTERACTION CURVE AND ERROR CALCULATIONS

To compare the accuracy of each of the design methods, with special attention on DMMI, normalized *P-M* interaction curves of ELM, DM, DMMI, and GMNIA are first plotted. Data points are obtained by determining the maximum combination of axial load P and bending moments M that can be applied at the member ends such that the strength requirements of the design method would just be satisfied—that is, interaction Equation 1 equals 1.0. Calculation of error values in the curves are then computed using the GMNIA curve as a basis. To further allow the errors to be comparable for the wide range of member slenderness ratios

investigated, all axial forces and moments were normalized by the maximum GMNIA values, with P^{GMNIA} being the maximum axial strength when the applied moment is $M = 0$ and with M^{GMNIA} being the maximum moment strength when the applied axial force is $P = 0$ (which would equal $0.9F_yZ$ for all members in this study). As an example, Figure 2 shows the normalized *P-M* interaction curves and a plot of the radial errors for a W12×120 member with an $L/r = 90$ that is subjected to minor-axis bending and with residual stresses included. Similar results for other L/r ratios for this W12×120 are provided in Appendix 1.

Using radial lines at 10° increments measured clockwise from the normalized *P*-axis to the *M*-axis, the intersections of the radial lines and the *P-M* curves are determined. It is noted that values at intersection points that lay between computed data points are obtained from a parabolic interpolation between the adjacent three data points. The percent errors of the design methods are then established by comparing their radial *R*-distances from the origin to the interaction curves according to:

$$\text{Percent radial error} = \frac{R_{XXX} - R_{GMNIA}}{R_{GMNIA}} \times 100\% \qquad (10)$$

where R_{XXX} is the radial distance of the *P-M* curves for the elastic design methods (ELM, DM, and DMMI), and R_{GMNIA} is the radial distance to the GMNIA *P-M* curve. As a result, error plots at different radial angles, as shown in Figure 2(b), represent a comprehensive range of different combinations of applied axial force and moment. Points with positive percent errors are indicative of situations in which the elastic design method (ELM, DM, or DMMI) is unconservative when compared to a design strength determined by GMNIA.

The legend within the rightward radial error graph [Figure 2(b)] contains information important to this study. Working from the top downward, rows within this legend represent results for the ELM, DM, and DMMI methods, respectively. The first two numbers in each row represent the error of each design method with an angle, θ, that corresponds to where the DMMI error is at its maximum. The second two numbers correspond to the maximum error of each design method and the angle, θ, where this maximum occurs.

CROSS SECTIONS INVESTIGATED

As indicated in Table 1, this study investigated 65 wide-flange shapes of ASTM A992 steel (E = 29,000 ksi and F_y = 50 ksi) and 4 HSS-shapes of ASTM A500 steel (E = 29,000 ksi and F_y = 46 ksi). These shapes are all of the compact sections that appear in the column design portion of the AISC *Steel Construction Manual* (AISC, 2017), and, for the most part, the wide-flange shapes investigated have depth-to-width ratios less than 1.5.

RESULTS

Interaction curves and plots of percent radial errors that correspond to the four different design methods (ELM, DM, DMMI, and GMNIA) were prepared (see, e.g., Figure 2) for

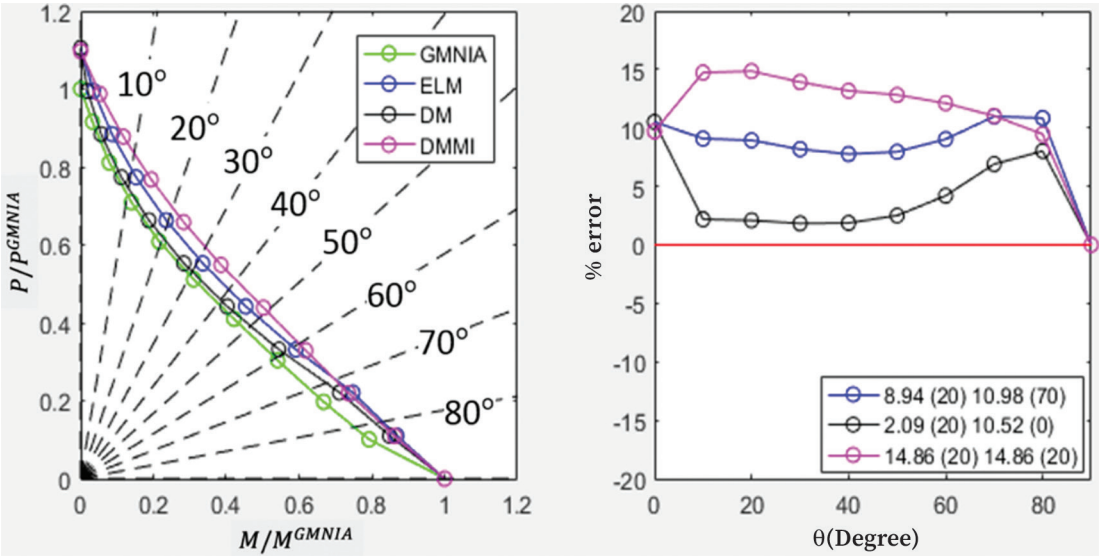

(a) Normalized P-M interaction curves for the four design methods

(b) Plots of percent radial errors

Fig. 2. For a W12×120 member with an L/r = 90 subject to minor-axis bending and with residual stresses included.

Table 1. Sections Studied							
W14	W14×730	W14×665	W14×605	W14×550	W14×500	W14×455	W14×426
	W14×398	W14×370	W14×342	W14×311	W14×282	W14×257	W14×233
	W14×211	W14×193	W14×176	W14×159	W14×145	W14×132	W14×120
	W14×109	W14×82	W14×74	W14×68	W14×61	W14×53	W14×48
W12	W12×336	W12×305	W12×279	W12×252	W12×230	W12×210	W12×190
	W12×170	W12×152	W12×136	W12×120	W12×106	W12×96	W12×87
	W12×79	W12×72	W12×58	W12×53	W12×50	W12×45	W12×40
W10	W10×112	W10×100	W10×88	W10×77	W10×68	W10×60	W10×54
	W10×49	W10×45	W10×39	W10×33			
W8	W8×67	W8×58	W8×48	W8×40	W8×35		
HSS	HSS12×12×½	HSS10×10×½	HSS8×8×½	HSS6×6×½			

all 65 W-shapes and 4 HSS-shapes over a range of member slenderness L/r ratios of 30, 60, 90, 120, and 150, with $r = \sqrt{I/A}$. With four cases, including minor- or major-axis bending for W-shapes and with or without residual stresses, this study evaluates 1,340 conditions, which are represented by a total of 58,960 analysis data points.

Wide-Flange Shapes

A summary of the results for all W-shapes is provided in Table 2, in which the maximum, average, and median of all of the individual member maximum percent radial errors are reported. In general, the percent radial errors reported for the three design methods are fairly similar. The largest percent radial errors are always for the DMMI method, and the smallest percent radial errors are for the DM method. Given that the ELM and DM methods are essentially the same, except that DM requires the analysis to include the stiffness reduction, $0.8\tau_b$, it is expected (and confirmed in Table 2) that DM will be more conservative (smaller radial errors) than ELM for all slenderness ratios. It is further noted that larger unconservative errors for DMMI for sections with residual stresses consistently occur when the applied loading combination is predominately axial force ($\theta = 10°$); in contrast, the larger unconservative errors for ELM and DM occur when the loading is primarily bending ($\theta = 80°$).

Hollow Structural Sections

The HSS-shape study does not include the parameter of bending axis because only square shapes are investigated. However, the effect of residual stress pattern is still investigated. A summary of the results for all HSS-sections is provided in Table 3. With the Mathur residual stress pattern, DMMI gives the largest percent radial errors among the three elastic design methods, a trend found consistent with W-shapes results. With the ECCS residual stress pattern, however, ELM gives the largest errors, while the errors of DMMI and DM are fairly close. It is worth noting that because the HSS shapes are modeled as square tubes without the curved corner geometry in STRAND7, the radius of gyration r of the STRAND7 model is slightly different from the AISC value, and consequently, the slenderness ratio L/r of HSS sections studied are close, but not exactly equal to 30, 60, 90, 120, and 150.

DISCUSSION

As would be expected, not including a residual stress distribution increases the design capacities of the beam-columns per the GMNIA design method. As a consequence, and given that the GMNIA results form the basis for the error analysis, the unconservative percent radial errors for all three of the elastic design methods (ELM, DM, and DMMI) are significantly reduced. A representative example of this is shown in Figure 3, where the performance of the DMMI design method is significantly improved with much better agreement (smaller radial errors) with GMNIA.

This increase in accuracy, however, is relatively pronounced where θ is small, which is a condition when the axial load is more significant than the bending moment, and is less obvious when θ is large, which is a combination of a larger bending moment and a smaller axial force. Of course, this is expected because it is well known that such residual stresses rarely affect the strength of a member subjected to a loading combination that is predominately bending (again noting that all members in this study are either subject to minor-axis bending or laterally braced when subject to major-axis flexure). The trend observed in Figure 3 is consistent for all shapes and design methods investigated in this study, regardless of the cross-sectional shapes, slenderness ratio, or the axis of bending investigated. In general,

Table 2. Summary of Percent Radial Errors of W-Shapes Studied for Minor- and Major-Axis Bending with and without Residual Stresses Included in the GMNIA Design					
		Minor-Axis, Residual Stresses	**Minor-Axis, No Residual Stresses**	**Major-Axis, Residual Stresses**	**Major-Axis, No Residual Stresses**
$L/r = 30$	DMMI	Max = 3.0% Ave = 2.2% Median = 2.2%	Max = 1.8% Ave = 0.5% Median = 0.4%	Max = 7.0% Ave = 6.5% Median = 6.6%	Max = 5.9% Ave = 5.0% Median = 5.0%
	ELM	Max = 3.2% Ave = 2.1% Median = 2.0%	Max= 2.5% Ave= 1.1% Median= 1.1%	Max = 6.9% Ave = 6.1% Median = 6.2%	Max = 5.8% Ave = 4.7% Median = 4.6%
	DM	Max = 2.6% Ave = 1.5% Median = 1.5%	Max = 1.9% Ave = 0.6% Median = 0.5%	Max = 6.0% Ave = 5.1% Median = 5.2%	Max = 4.9% Ave = 3.8% Median = 3.6%
$L/r = 60$	DMMI	Max = 14.8% Ave = 13.7% Median = 13.9%	Max = 7.3% Ave = 6.1% Median = 6.1%	Max = 10.5% Ave = 10.0% Median = 10.0%	Max = 7.5% Ave = 6.7% Median = 6.6%
	ELM	Max = 9.7% Ave = 8.4% Median = 8.4%	Max = 8.8% Ave = 7.5% Median = 7.6%	Max = 9.2% Ave = 8.5% Median = 8.6%	Max = 6.1% Ave = 5.2% Median = 5.3%
	DM	Max = 8.2% Ave = 7.3% Median = 7.3%	Max = 6.7% Ave = 5.5% Median = 5.5%	Max = 6.4% Ave = 5.7% Median = 5.8%	Max = 3.6% Ave = 2.9% Median = 3.0%
$L/r = 90$	DMMI	Max = 15.8% Ave = 14.8% Median = 14.8%	Max = 9.7% Ave = 8.2% Median = 8.2%	Max = 10.0% Ave = 9.2% Median = 9.2%	Max = 5.4% Ave = 4.7% Median = 4.7%
	ELM	Max = 13.0% Ave = 11.1% Median = 11.1%	Max = 11.3% Ave = 9.8% Median = 9.8%	Max = 7.6% Ave = 6.9% Median = 6.9%	Max = 4.5% Ave = 3.5% Median = 3.5%
	DM	Max = 11.2% Ave = 9.6% Median = 9.6%	Max = 8.2% Ave = 6.7% Median = 6.7%	Max = 3.9% Ave = 3.2% Median = 3.3%	Max = 1.5% Ave = 0.6% Median = 0.6%
$L/r = 120$	DMMI	Max = 15.3 % Ave = 14.2% Median = 14.1%	Max = 11.0% Ave = 9.6% Median = 9.6%	Max = 7.1% Ave =6.2% Median = 6.2%	Max = 2.9% Ave = 2.2% Median = 2.2%
	ELM	Max = 12.7% Ave = 11.3% Median = 11.3%	Max = 11.4% Ave = 9.9% Median = 9.9%	Max = 5.8% Ave = 4.6% Median = 4.6%	Max = 2.7% Ave = 1.8% Median = 1.8%
	DM*	Max = 9.5% Ave = 8.0% Median = 8.0%	Max = 8.1% Ave = 6.6% Median = 6.6%	Max = 2.6% Ave = 1.5% Median = 1.4%	Max = n/a* Ave = n/a Median = n/a
$L/r = 150$	DMMI	Max = 14.0% Ave = 12.6% Median = 12.6%	Max = 11.8% Ave = 10.4% Median = 10.4%	Max = 5.6% Ave = 4.8% Median = 4.7%	Max = 2.1% Ave = 1.2% Median = 1.2%
	ELM	Max = 12.4% Ave = 10.9% Median = 10.9%	Max = 11.2% Ave = 9.8% Median = 9.8%	Max = 4.4% Ave = 3.4% Median = 3.4%	Max = 1.4% Ave = 0.5% Median = 0.5%
	DM*	Max = 9.0% Ave = 7.6% Median = 7.6%	Max = 7.8% Ave = 6.4% Median = 6.4%	Max = 1.1% Ave = 0.2% Median = 0.1%	Max = n/a Ave = n/a Median = n/a
Note: No unconservative errors are observed as indicated by n/a					

Table 3. Summary of Percent Radial Errors of HSS Sections Studied with High and Low Residual Stresses Included in the GMNIA Design			
		High Residual Stress (Mathur)	**Low Residual Stress (ECCS)**
$L/r = 30$	DMMI	Max = 1.7% Ave = 1.4% Median = 1.4%	Max = 1.3% Ave = 0.7% Median = 1.0%
	ELM	Max = 1.6% Ave = 1.1% Median = 1.1%	Max = 1.3% Ave = 0.8% Median = 1.0%
	DM	Max = 1.6% Ave = 1.1% Median = 1.1%	Max = 1.3% Ave = 0.7% Median = 1.0%
$L/r = 60$	DMMI	Max = 10.0% Ave = 9.6% Median = 9.5%	Max = 2.4% Ave = 1.6% Median = 1.8%
	ELM	Max = 5.4% Ave = 4.3% Median = 4.1%	Max = 3.1% Ave = 2.6% Median = 2.4%
	DM	Max = 3.8% Ave = 3.3% Median = 3.3%	Max = 2.4% Ave = 1.6% Median = 1.8%
$L/r = 90$	DMMI	Max = 17.5% Ave = 16.2% Median = 16.2%	Max = 3.5% Ave = 2.9% Median = 2.9%
	ELM	Max = 14.6% Ave = 13.2% Median = 13.1%	Max = 4.8% Ave = 4.3% Median = 4.1%
	DM	Max = 14.6% Ave = 13.2% Median = 13.1%	Max = 3.5% Ave = 2.9% Median = 2.9%
$L/r = 120$	DMMI	Max = 14.8% Ave = 14.1% Median = 14.3%	Max = 5.7% Ave = 3.7% Median = 3.5%
	ELM	Max = 13.6% Ave = 11.8% Median = 11.8%	Max = 5.7% Ave = 5.2% Median = 5.1%
	DM	Max = 13.6% Ave = 11.6% Median = 11.8%	Max = 5.7% Ave = 3.7% Median = 3.5%
$L/r = 150$	DMMI	Max = 17.0% Ave = 15.9% Median = 15.7%	Max = 6.3% Ave = 4.0% Median = 4.1%
	ELM	Max = 11.7% Ave = 11.4% Median = 11.4%	Max = 5.7% Ave = 5.6% Median = 5.7%
	DM	Max = 8.3% Ave = 8.0% Median = 8.0%	Max = 5.7% Ave = 4.0% Median = 4.1%

the reduction in DMMI errors for sections without residual stresses is largest for W-shapes when the slenderness ratio is $L/r = 60$ for minor-axis bending and $L/r = 90$ for major-axis bending. In moving from high to low residual stresses, the reduction is largest when slenderness ratio of HSS-sections is $L/r = 90$. The change in error is the smallest at the extreme slenderness ratios investigated, including the least-slender ($L/r = 30$) and most-slender ($L/r = 150$) members for W-shapes, and when the beam-column is stocky ($L/r = 30$) for HSS-sections. It is further noted that the ELM and DM design methods can be significantly more conservative when residual stresses are not present.

From the W-shape results in this study, it can be observed that with the exception of more-stocky members ($L/r = 30$), the percent radial errors for all three design methods, especially DMMI, are reduced when members are subject to major-axis bending instead of minor-axis bending.

As further shown in Tables 2 and 3, all three elastic design methods will produce some unconservative errors when compared with GMNIA-based design in most of the cases studied. For the reasons given earlier, DM will always provide smaller percent radial errors when compared with ELM. It is important to note that this applies only for the simply supported member explored in this study—for systems comprised of members with effective length K-factors exceeding 1.0, this will not necessarily be the case (Martinez-Garcia and Ziemian, 2006).

The results for DMMI and ELM are not significantly different, with the largest differences occurring for W-shape members subject to minor-axis bending in the low- to mid-slenderness ($L/r = 60$ to 90), and for HSS-section member with $L/r = 60$.

SUMMARY AND CONCLUSION

This study evaluates three elastic design methods (ELM, DM, and DMMI) appearing in the 2016 AISC *Specification* by making comparisons with a fourth method (GMNIA) that is often considered the most "exact" because all destabilizing effects are explicitly modeled in the analysis. This latter method, design by advanced inelastic analysis, also appears in the AISC *Specification*. With 1,340 conditions studied that required a total of 58,960 analyses, simply supported beam-columns comprised of a fairly wide range of column W- and HSS- sections and slenderness ratios are investigated for conditions of minor- or major-axis flexure that include or exclude the presence of residual stresses. In all cases, members are assumed to be fully braced out-of-plane.

In general, all three elastic design methods provide fairly similar results. AISC's relatively new design by advanced elastic analysis method, termed DMMI in this

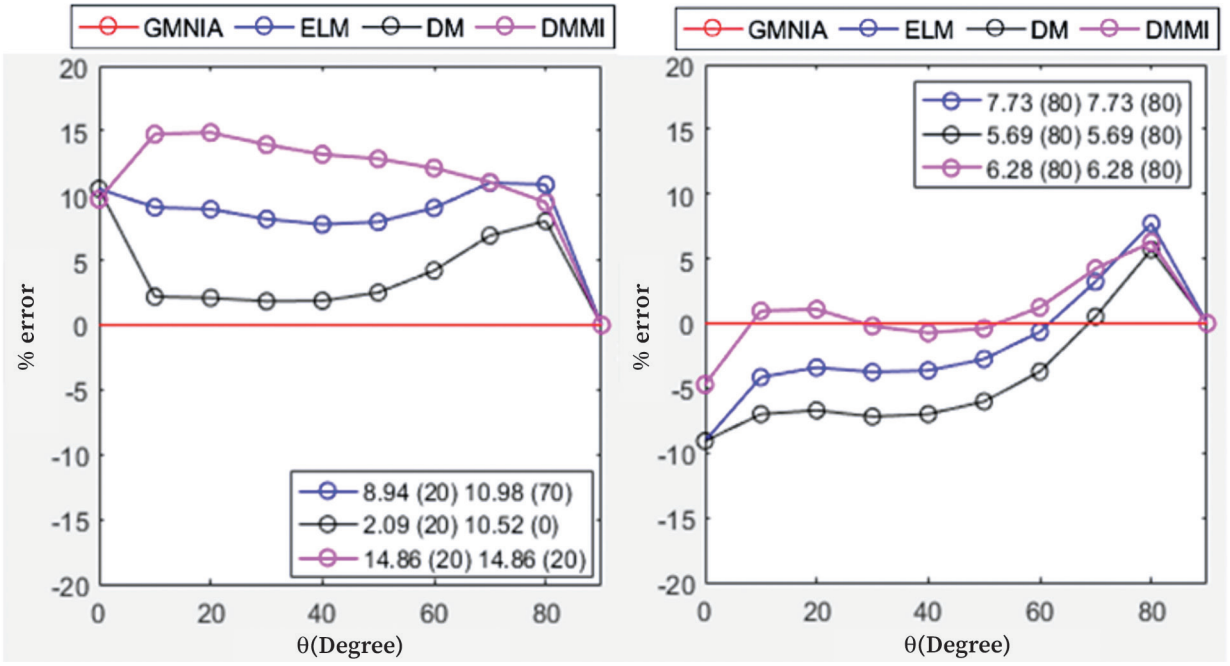

(a) Residual stresses included in the GMNIA-based design

(b) Residual stresses excluded in the GMNIA-based design

Fig. 3. Percent radial errors for a member of an L/r = *60 subjected to minor-axis bending comprised of a W12×120 section.*

study, consistently indicated more strength (1% to 5%) than AISC's effective length method. Conditions of major-axis bending for W-shapes significantly improved the performance of all three elastic design methods. Regardless of the axis of bending, results are always improved when residual stresses are lowered or eliminated, a condition that is quite common for HSS-shapes and often the consequence of rotary straightening W-shapes during the rolling process. Knowing that ELM has been an established design method that has performed well in the United States since the early 1960s, it is the authors' opinion that the unconservative errors for all three elastic design methods may not be reason for significant concern. Based on the many systems previously investigated by the second author in the development of AISC's design by advanced elastic analysis method (DMMI), the study presented in this paper has provided some well-served deserved investigations on beam-columns subject to minor-axis bending.

Noting that AISC's design by advanced elastic analysis method currently only permits that the axial strength P_n can be taken as the cross-section strength P_y, additional studies are needed to permit this approach to move to a full cross-section-based design method—in other words, move from requiring the flexural strength M_n to account for member length effects, such as lateral-torsional buckling, to being taken as cross-section strength M_p. Of course, such a revision will require that engineers have access to commercially available analysis software that directly models nonuniform torsion, and thereby permits the analysis to account for the rapid increase in moments as lateral-torsional and flexural-torsional buckling modes of failure are approached.

ACKNOWLEDGEMENTS

The authors gratefully acknowledge Gigi Rojahn for providing the STRAND7 data, which provided the HSS-section GMNIA results as a basis for comparison.

APPENDIX A

Plots of Interaction Curves and Percent Radial Error

As a complement to Figure 2, the remaining normalized *P-M* interaction curves and corresponding plots of percent radial errors that were studied for the specific case of a W12×120 member that includes residual stresses and subjected to minor-axis bending are provided in Figures A-1 through A-4.

APPENDIX B

Data for Plots of Percent Radial Errors

Tables B-1 through B-5 provide numerical values for the data points appearing in the percent radial error plots given in Figure 2 and Appendix A, and for similar plots for the presented example of a W12×120. These percent radial errors represent the minor- and major-axis bending cases for when residual stresses are either included or excluded. A positive error value indicates nonconservative error when compared to GMNIA results, and likewise, a negative error represents conservative error.

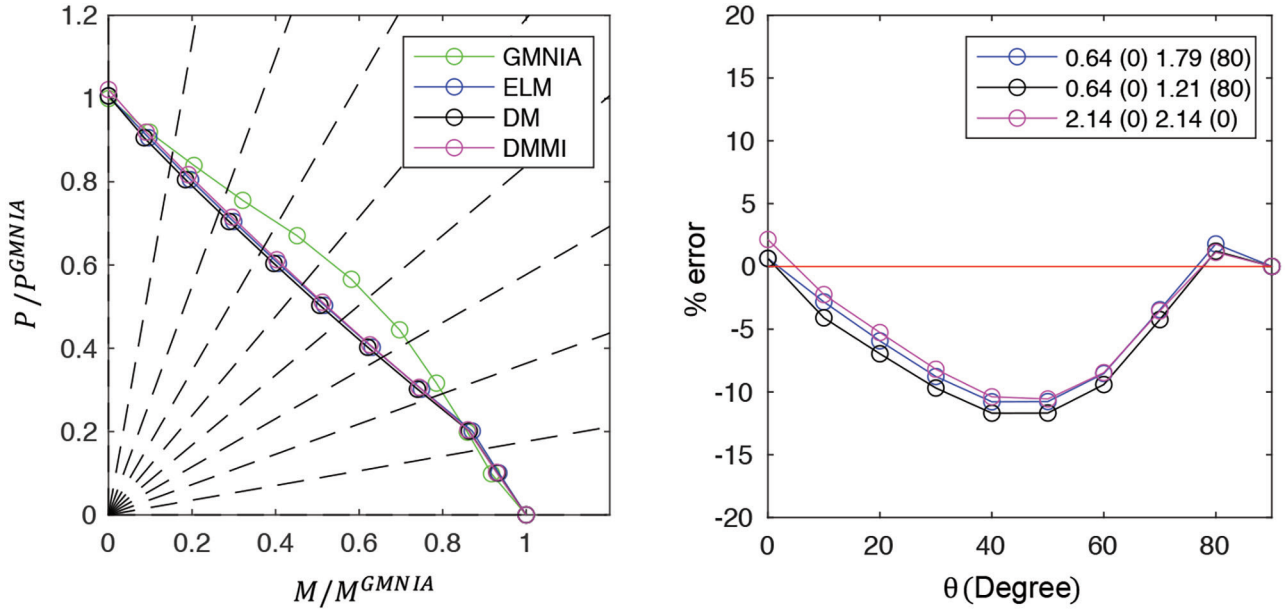

Fig. A-1. L/r = *30.*

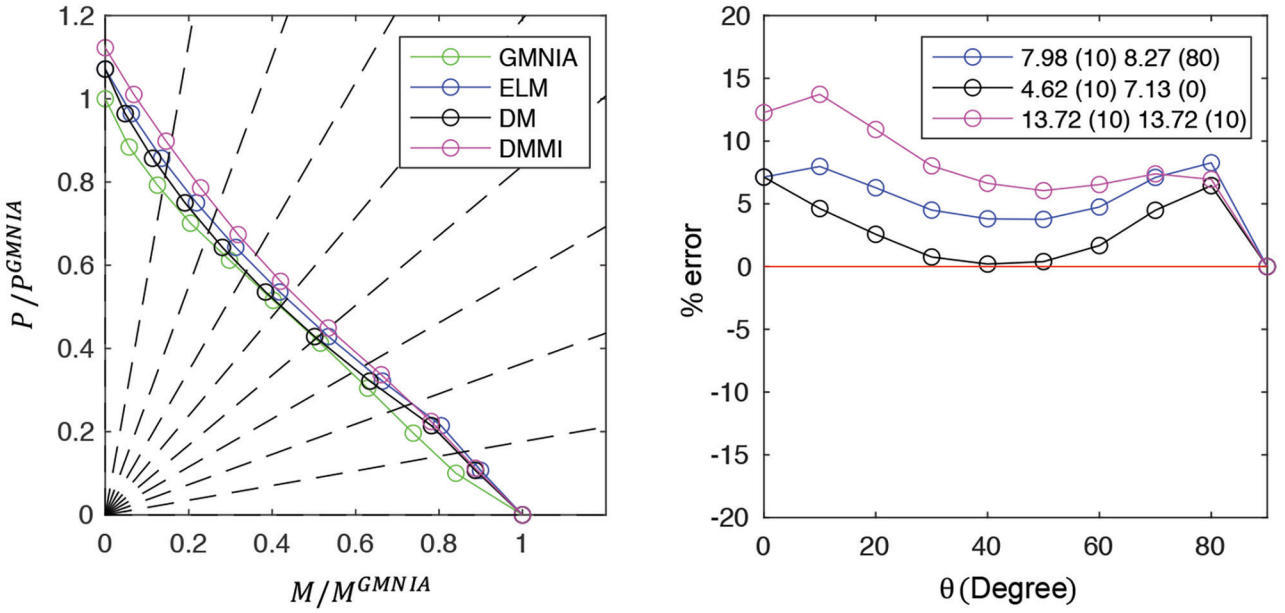

Fig. A-2. L/r = *60.*

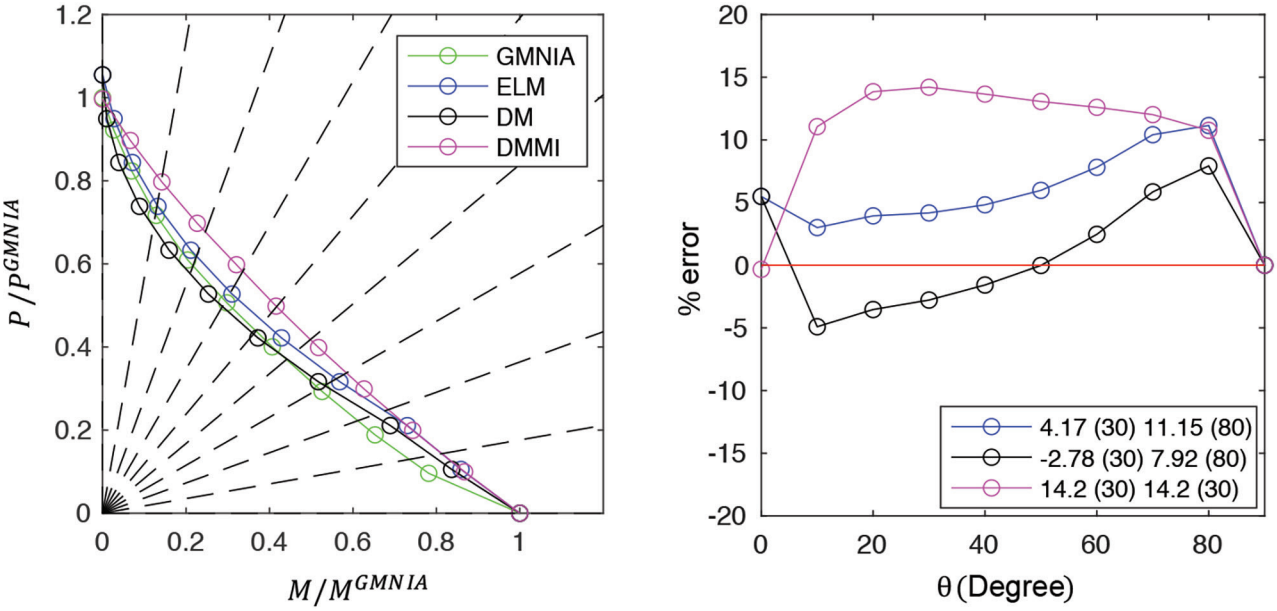

Fig. A-3. L/r = *120.*

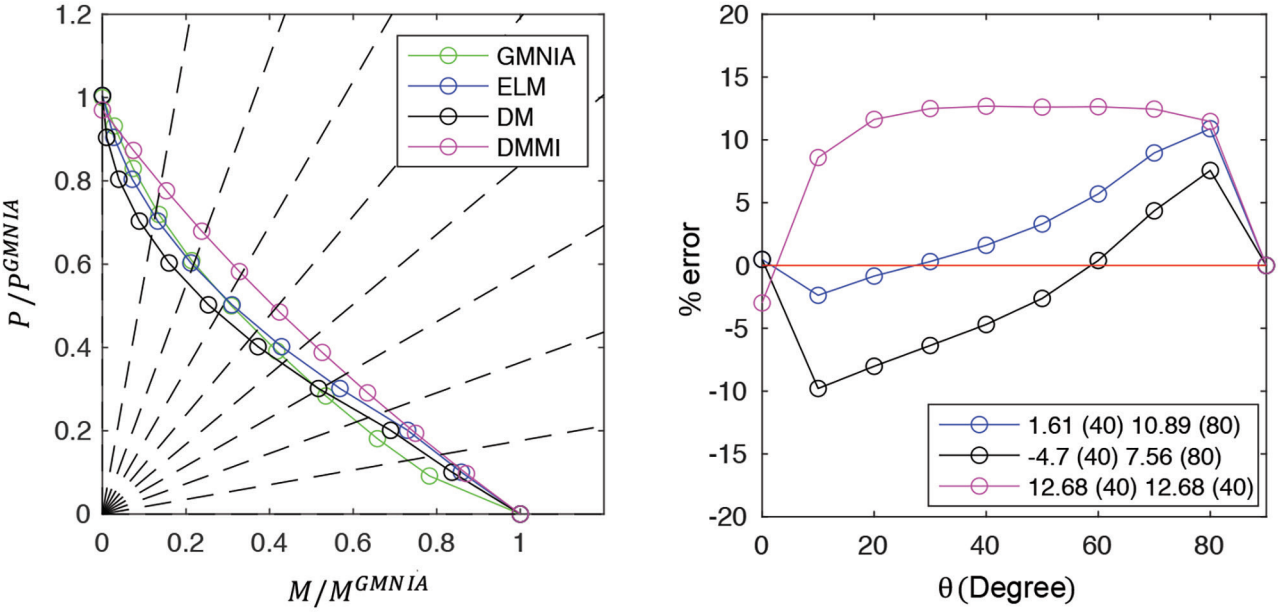

Fig. A-4. L/r = *150.*

Table B-1. $L/r = 30$ (values are percent radial errors)												
	Minor-Axis Bending with Residual Stresses			Minor-Axis Bending without Residual Stresses			Major-Axis Bending with Residual Stresses			Major-Axis Bending without Residual Stresses		
θ	DMMI	ELM	DM	DMMI	ELM	DM	DMMI	ELM	DM	DMMI	ELM	DM
0°	2.1	0.6	0.6	–6.0	–7.4	–7.4	2.1	–0.2	–0.2	–0.8	–3.1	–3.1
10°	–2.2	–2.8	–4.1	–6.7	–7.2	–8.4	3.8	2.6	1.3	–0.2	–1.4	–2.6
20°	–5.3	–5.9	–7.0	–6.9	–7.6	–8.6	5.1	3.8	2.7	2.4	1.2	0.1
30°	–8.2	–8.8	–9.7	–9.6	–10.2	–11.1	5.8	4.6	3.6	3.2	2.1	1.1
40°	–10.4	–10.8	–11.7	–12.1	–12.5	–13.4	6.2	5.4	4.3	3.7	2.9	1.8
50°	–10.6	–10.8	–11.7	–12.9	–13.2	–14.1	6.5	5.9	4.8	4.5	3.9	2.9
60°	–8.5	–8.5	–9.4	–11.1	–11.2	–12.1	6.3	6.0	5.0	5.0	4.6	3.6
70°	–3.5	–3.4	–4.2	–6.0	–5.9	–6.7	5.9	5.8	5.0	4.6	4.5	3.6
80°	1.1	1.8	1.2	0.4	1.1	0.4	2.9	3.4	2.8	2.2	2.8	2.2
90°	0	0.0	0.0	0.0	0.0	0.0	0.0	0.0	0.0	0.0	0.0	0.0

Table B-2. $L/r = 60$ (values are percent radial errors)												
	Minor-Axis Bending with Residual Stresses			Minor-Axis Bending without Residual Stresses			Major-Axis Bending with Residual Stresses			Major-Axis Bending without Residual Stresses		
θ	DMMI	ELM	DM	DMMI	ELM	DM	DMMI	ELM	DM	DMMI	ELM	DM
0°	12.3	7.1	7.1	–4.7	–9.1	–9.1	3.8	–2.6	–2.6	–6.6	–12.4	–12.4
10°	13.7	8.0	4.6	1.0	–4.2	–7.0	6.8	0.3	–2.7	0.4	–5.8	–8.5
20°	10.9	6.3	2.6	1.1	–3.4	–6.7	8.1	2.5	–1.0	–0.3	–5.6	–8.8
30°	8.0	4.5	0.8	–0.2	–3.8	–7.2	8.5	4.0	0.3	3.1	–1.3	–4.9
40°	6.6	3.8	0.2	–0.7	–3.6	–7.0	9.0	5.3	1.6	4.8	1.0	–2.5
50°	6.1	3.8	0.4	–0.4	–2.8	–6.0	9.8	6.8	3.3	5.2	2.2	–1.3
60°	6.5	4.7	1.7	1.2	–0.7	–3.7	10.5	8.1	4.9	6.3	3.8	0.6
70°	7.4	7.1	4.5	4.2	3.2	0.5	9.5	8.5	5.7	7.0	5.5	2.7
80°	6.9	8.3	6.4	6.3	7.7	5.7	5.1	6.3	4.3	3.7	4.9	2.9
90°	0	0.0	0.0	0.0	0.0	0.0	0.0	0.0	0.0	0.0	0.0	0.0

Table B-3. $L/r = 90$ (values are percent radial errors)												
	Minor-Axis Bending with Residual Stresses			Minor-Axis Bending without Residual Stresses			Major-Axis Bending with Residual Stresses			Major-Axis Bending without Residual Stresses		
θ	DMMI	ELM	DM	DMMI	ELM	DM	DMMI	ELM	DM	DMMI	ELM	DM
0°	9.7	10.5	10.5	–2.7	–2.0	–2.0	0.4	–1.0	–1.0	–5.7	–7.0	–7.0
10°	14.7	9.1	2.2	2.2	–2.8	–8.8	4.1	–2.1	–8.1	–0.6	–6.5	–12.3
20°	14.9	8.9	2.1	3.3	–2.1	–8.2	5.4	–0.9	–7.1	0.3	–5.8	–11.6
30°	13.9	8.2	1.8	3.7	–1.7	–7.4	6.6	0.5	–5.4	2.4	–3.6	–9.4
40°	13.2	7.8	1.9	4.2	–0.9	–6.5	8.0	2.1	–3.6	3.9	–1.8	–7.5
50°	12.8	8.0	2.5	5.1	0.4	–4.8	9.2	3.9	–1.5	4.3	–0.9	–6.1
60°	12.1	9.0	4.2	6.5	2.9	–1.8	9.4	5.4	0.5	4.8	0.7	–4.1
70°	11.0	11.0	6.9	7.6	6.7	2.5	8.0	6.9	2.7	4.4	2.8	–1.3
80°	9.5	10.8	8.0	8.2	9.7	6.7	4.8	6.1	3.2	2.2	3.5	0.6
90°	0	0.0	0.0	0.0	0.0	0.0	0.0	0.0	0.0	0.0	0.0	0.0

Table B-4. $L/r = 120$ (values are percent radial errors)												
	Minor-Axis Bending with Residual Stresses			Minor-Axis Bending without Residual Stresses			Major-Axis Bending with Residual Stresses			Major-Axis Bending without Residual Stresses		
θ	DMMI	ELM	DM	DMMI	ELM	DM	DMMI	ELM	DM	DMMI	ELM	DM
0°	–0.3	5.5	5.5	–5.6	–0.1	–0.1	–5.7	–1.4	–1.4	–7.1	–2.9	–2.9
10°	11.1	3.0	–4.9	0.9	–6.3	–13.4	1.0	–7.0	–14.0	–1.1	–9.0	–15.8
20°	13.8	3.9	–3.5	3.2	–5.7	–12.5	3.6	–6.0	–12.8	0.4	–8.8	–15.4
30°	14.2	4.2	–2.8	4.9	–4.5	–10.8	5.4	–4.6	–10.9	1.2	–8.4	–14.5
40°	13.7	4.8	–1.6	5.8	–2.7	–8.7	6.0	–3.0	–9.0	1.5	–7.2	–13.0
50°	13.1	6.0	0.0	6.7	–0.2	–5.9	6.3	–1.1	–6.8	2.3	–4.9	–10.4
60°	12.6	7.8	2.5	7.7	2.8	–2.4	6.2	0.9	–4.2	2.3	–2.9	–7.8
70°	12.0	10.4	5.9	8.7	6.8	2.3	5.6	3.4	–1.0	2.1	–0.2	–4.5
80°	10.8	11.1	7.9	9.4	9.8	6.5	4.2	4.4	1.2	1.6	1.9	–1.2
90°	0	0.0	0.0	0.0	0.0	0.0	0.0	0.0	0.0	0.0	0.0	0.0

Table B-5. $L/r = 150$ (values are percent radial errors)												
	Minor-Axis Bending with Residual Stresses			Minor-Axis Bending without Residual Stresses			Major-Axis Bending with Residual Stresses			Major-Axis Bending without Residual Stresses		
θ	DMMI	ELM	DM	DMMI	ELM	DM	DMMI	ELM	DM	DMMI	ELM	DM
0°	–3.0	0.5	0.5	–6.5	–3.2	–3.2	–7.4	–4.9	–4.9	–9.4	–7.0	–7.0
10°	8.6	–2.4	–9.8	–0.2	–10.2	–17.0	–0.8	–11.3	–18.0	–4.8	–14.9	–21.2
20°	11.6	–0.8	–8.0	2.4	–9.0	–15.6	1.6	–10.3	–16.8	–1.9	–13.3	–19.6
30°	12.5	0.3	–6.4	4.2	–7.2	–13.4	2.8	–8.9	–15.0	0.0	–11.4	–17.3
40°	12.7	1.6	–4.7	5.7	–4.8	–10.8	3.6	–7.1	–13.0	0.7	–9.8	–15.5
50°	12.6	3.3	–2.6	7.1	–2.0	–7.7	4.3	–4.9	–10.4	0.1	–8.8	–14.2
60°	12.6	5.7	0.4	8.5	1.5	–3.6	4.7	–2.4	–7.4	0.5	–6.4	–11.3
70°	12.5	9.0	4.4	9.7	6.0	1.5	4.7	0.8	–3.5	1.0	–2.9	–7.1
80°	11.5	10.9	7.6	10.2	9.6	6.2	3.9	3.3	0.1	1.3	0.7	–2.5
90°	0	0.0	0.0	0.0	0.0	0.0	0.0	0.0	0.0	0.0	0.0	0.0

REFERENCES

AISC (2005), *Specification for Structural Steel Buildings*, ANSI/AISC 360-05, American Institute of Steel Construction, Chicago, Ill.

AISC (2010), *Specification for Structural Steel Buildings*, ANSI/AISC 360-10, American Institute of Steel Construction, Chicago, Ill.

AISC (2016a), *Code of Standard Practice for Steel Buildings and Bridges*, ANSI/AISC 303-16, American Institute of Steel Construction, Chicago, Ill.

AISC (2016b), *Specification for Structural Steel Buildings*, ANSI/AISC 360-16, American Institute of Steel Construction, Chicago, Ill.

AISC (2017), *Steel Construction Manual*, 15th Ed., American Institute of Steel Construction, Chicago, Ill.

Alemdar, B.N. (2001), "Distributed Plasticity Analysis of Steel Building Structural Systems," PhD dissertation, Georgia Institute of Technology, Atlanta, Ga.

ECCS (1984), "Ultimate Limit State Calculation of Sway Frames with Rigid Joints," Publication No. 33, European Convention for Constructional Steelwork, Brussels, Belgium.

Galambos, T.V. and Ketter, R.L. (1959), "Columns under Combined Bending and Thrust," *Journal of the Engineering Mechanics Division*, ASCE, Vol. 85, No. EM2, pp. 135–152.

Ge, X. and Yura, J. (2019), "The Strength of Rotary-Straightened Steel Columns," *Proceedings of the Annual Stability Conference*, SSRC, St. Louis, Mo., pp. 425–442.

Giesen-Loo, E. (2016), "Design of Steel Structures by Advanced 2nd-Order Elastic Analysis—Background Studies," Honors Thesis, Bucknell University, Lewisburg, Pa.

Martinez-Garcia, J.M. and Ziemian, R.D. (2006), "Benchmark Studies to Compare Frame Stability Provisions," *Proceedings of the Annual Technical Session and Meeting*, SSRC, San Antonio, Texas, pp. 425–442.

Mathur, K. (2011), "Effects of Residual Stresses and Initial Imperfections on Earthquake Response of Steel Moment Frames," Master of Science Thesis, University of Illinois at Urbana-Champaign, Urbana, Ill.

McGuire, W., Gallagher, R., and Ziemian, R. (2000), *Matrix Structural Analysis*, John Wiley & Sons, Inc., New York, N.Y.

Nwe Nwe, M.T. (2014), "The Modified Direct Analysis Method: An Extension of the Direct Analysis Method," Honors Thesis, Bucknell University, Lewisburg, Pa.

Wang, Y. (2018), "Advanced Analysis of Beam-Columns Resisting Minor Axis Bending," Honors Thesis, Bucknell University, Lewisburg, Pa.

Wang, Y. and Ziemian, R.D. (2019), "Design by Advanced Elastic Analysis—An Investigation of Beam-Columns Resisting Minor-Axis Bending," *Proceedings of the Annual Stability Conference,* SSRC, St. Louis, Mo.

Ziemian, R.D. (ed.) (2010), *Guide to Stability Design Criteria for Metal Structures*, John Wiley & Sons, Inc., Hoboken, N.J.

Technical Note

Internal Second-Order Stiffness: A Refined Approach to the R_M Coefficient to Account for the Influence of P-δ on P-Δ

RAFAEL SABELLI and LAWRENCE GRIFFIS

ABSTRACT

One component of the B_2 amplifier method of addressing second-order effects is the R_M coefficient, which represents the influence of P-δ on P-Δ effects. This paper presents the background for R_M based on LeMessurier's paper, "A Practical Method of Second-Order Analysis: Part 2—Rigid Frames," (1977), and makes explicit the simplifications entailed in the AISC *Specification for Structural Steel Buildings* (AISC, 2016b) formulation for this coefficient. These simplifications, while providing for reliable strength design, can overestimate the P-δ effect for typical building applications, especially if applied to drift. A simple formula for R_M based on the work of LeMessurier permits a more precise estimate, which can be used as a component of both force and displacement amplifiers presented in this paper. This explicit approach to the R_M coefficient provides the basis for clear presentation of the relationships first-order and second-order stiffness (both internal and external), including the distinct effects of P-δ and P-Δ stiffness reductions on equilibrium at the second-order displacement.

Keywords: second-order analysis, stability.

INTRODUCTION

The AISC *Specification for Structural Steel Buildings* (AISC, 2016b), hereafter referred to as the AISC *Specification*, presents an approximate method for second-order analysis in Appendix 8, using a factor B_2 to amplify forces to account for P-δ and P-Δ effects. While the application of this method is clear in the *Specification*, the derivation is not presented, and the implicit simplifications made can easily be missed. This paper traces the connections between the source material [the landmark LeMessurier paper, "A Practical Method of Second-Order Analysis: Part 2—Rigid Frames," (1977)], and the method in the *Specification*. In the process, the relationship between the distinct amplifiers for force (B_2) and displacement (presented here as D_{AF}) is made explicit, and a refined formulation of R_M is presented.

The use of the refined formulation of R_M permits minor reduction in conservatism for typical building cases. Additionally, the availability of more accurate hand methods of calculating second-order effects empowers engineers to better understand and critically evaluate the results of computerized second-order analyses. The reconciliation of the B_2 amplifier with amplified displacements may be of use to engineers employing the amplifier method. Understanding the basis of the amplifier method is particularly helpful to students, as is understanding the relationships between first-order stiffness and internal and external second-order stiffness.

Rafael Sabelli, Director of Seismic Design, Walter P Moore, San Francisco, Calif. Email: rsabelli@walterpmoore.com (corresponding)

Lawrence Griffis, Senior Consultant, Walter P Moore, Austin, Texas Email: lgriffis@walterpmoore.com

Paper No. 2020-08

A REFINED R_M

Force Amplification

The amplifier-based method of second-order analysis, as presented in AISC *Specification* Appendix 8 (2016b), requires consideration of the influence of P-δ on P-Δ effects. This is represented by the coefficient R_M, which is incorporated into the AISC *Specification* equation for the force amplifier B_2. The B_2 amplifier is defined by *Specification* Equations A-8-6 and A-8-7, which can be combined and expressed as:

$$B_2 = \frac{1}{1 - \dfrac{P_{story}\Delta_1}{R_M HL}} \tag{1}$$

where

B_2 = force amplification factor for second-order effect
H = first-order shear, kips (N)
L = story height, in. (mm)

P_{story} = total gravity load, $P_{mf} + P_{lean}$, at LRFD level, kip (N)

P_{lean} = gravity load on non-moment-frame columns, kip (N)

P_{mf} = gravity load on moment-frame columns, kip (N)

R_M = stiffness-reduction coefficient to account for member P-δ influence on structure P-Δ

Δ_1 = first-order story drift corresponding to load H (Δ_H in the AISC *Specification*), in. (mm)

The AISC *Specification* LRFD/ASD adjustment factor α is omitted from the gravity-load definitions for brevity.

The R_M term in Equation 1 effectively reduces the lateral stiffness of the system from the first-order stiffness (H/Δ_1), and the reduced stiffness with P-δ included ($R_M H/\Delta_1$) is used to determine the P-Δ effect. (Note that in this study, the terms B_2 and R_M represent their functions as described in their definitions, rather than the formulas for these quantities in the AISC *Specification*. More accurate formulas for these quantities are presented later.)

The B_2 amplifier can be used to determine the overturning moment corresponding to equilibrium in the deformed condition (i.e., at the second-order drift Δ_2), as shown for a simple structure in Figure 1:

$$B_2 HL = HL + P_{story}\Delta_2 \tag{2}$$

where

Δ_2 = second-order story drift, in. (mm)

(This amplification also applies to the shear at the sloped top of the cantilever column, considering the vertical force P_{mf}.)

The B_2 amplifier can be expressed as a function of the second-order story drift Δ_2 by rearranging Equation 2:

$$B_2 = 1 + \frac{P_{story}\Delta_2}{HL} \tag{3}$$

The symbol F_{AF} can denote a force amplification factor ["FAF" in Equation A-6 in Griffis and White (2013)], which by definition is equal to B_2:

$$F_{AF} = B_2 \tag{4}$$

Displacement Amplification

A displacement amplification factor, D_{AF} ("DAF" in Equation A-7 in Griffis and White [2013]), can be defined as:

$$D_{AF} = \frac{\Delta_2}{\Delta_1} \tag{5}$$

Combining Equations 1, 3, and 5, the displacement amplifier D_{AF} can be related to B_2 and R_M:

$$D_{AF} = \frac{B_2}{R_M} \tag{6}$$

The R_M coefficient can be defined as the ratio of force to displacement amplification by rearranging Equation 6:

$$R_M = \frac{B_2}{D_{AF}} \tag{7}$$

$$R_M = \frac{B_2\Delta_1}{\Delta_2} \tag{8}$$

The accuracy of both the forces obtained with the amplifier B_2 in Equation 1 and the drifts computed using Equation 6 are dependent on the accuracy of the coefficient R_M. The AISC *Specification* (2016b) provides a conservative, approximate formula for R_M (*Specification* Equation A8-8):

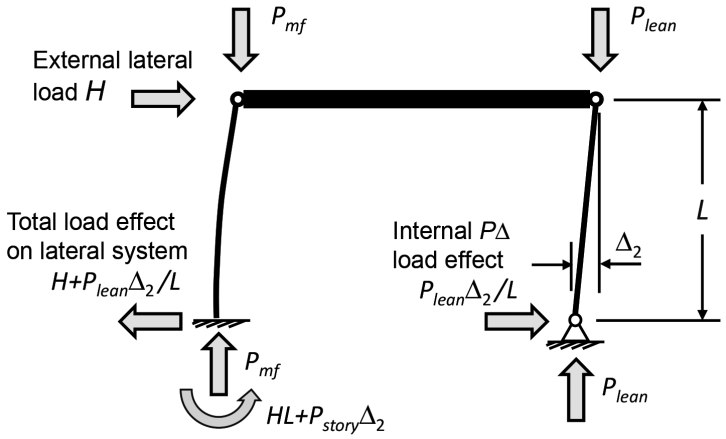

Fig. 1. Equilibrium diagram at second-order displacement.

$$R_M = 1 - 0.15\frac{P_{mf}}{P_{story}} \tag{9}$$

The AISC *Specification* Commentary explains that the minimum value of 0.85 (when $P_{mf}/P_{story} = 1.0$) represents a lower bound based on LeMessurier's work. While Equation 9 is suitably conservative for reliability in strength design, it can overestimate the P-δ effect on drift if used in Equation 6, especially for stiff systems, and a more precise expression of R_M may be obtained based on LeMessurier's work.

Column Flexural Stiffness Reduction Due to P-δ Effects

Equation 37 in LeMessurier's paper presents the force-amplification factor (A.F.), which has the same function as B_2. Changing terms in LeMessurier's equation to be consistent with those used earlier gives:

$$B_2 = \frac{1}{1 - \dfrac{P_{story}}{\dfrac{HL}{\Delta_1} - C_L P_{mf}}} \tag{10}$$

where

C_L = flexural stiffness-reduction coefficient for a moment-frame column due to P-δ effects

The coefficient C_L is potentially different for each column, varying with its deflected shape. For cantilever columns and for moment frames with points of inflection near column mid-height and beam mid-length, LeMessurier's Equations 60 and 58, respectively provide an approximation of C_L:

$$C_L \cong \frac{\dfrac{12}{\pi^2} - 1}{(1+G)^2} \tag{11}$$

where

$$G = \frac{\Sigma\dfrac{EI_{col}}{L_{col}}}{\Sigma\dfrac{EI_g}{L_g}} \tag{12}$$

and

E = modulus of elasticity, ksi (N/mm^2)
G = moment-frame relative flexural-stiffness parameter
I_{col} = column moment of inertia, in.^{4} (mm^4)
I_g = girder (beam) moment of inertia, in. (mm)
L_{col} = column height, in. (mm)
L_g = girder length, in. (mm)

The "–1" term in Equations 11 is the subtraction of the P-Δ effect on moment-frame columns, as this is accounted for in the effect of P_{story} in Equation 10. The largest possible value of C_L corresponds to the buckled shape of a rigid-base cantilever or fixed-fixed column with rigid beams at the top and bottom (for which $G = 0$):

$$C_L \le \frac{12}{\pi^2} - 1 \le 0.216 \tag{13}$$

As is shown later, conservatively taking the maximum value of C_L from Equation 13 for all columns is less conservative than Equation 9. For real buildings, however, beams framing into columns do not provide rigid restraint against column rotation, and Equation 11 facilitates determination of significantly lower values of C_L than the maximum value from Equation 13. It is possible to establish a maximum value of C_L based on a minimum value for the ratio G (Equation 12) corresponding to typical beam-column proportioning and frame dimensions, further reducing the calculated P-δ effects. (This beam flexibility must also be incorporated into the analysis. The total effect of beam flexibility is, of course, an increase in displacement and a decrease in strength.) For example, Cheong-Siat-Moy (1976) proposed optimal proportioning of frames for drift control, which corresponds to $G = 1.0$. Similarly, the AISC *Seismic Provisions* (2016a) contain proportioning requirements for beam and column strength for special moment frames that have some correlation to Equation 12. No minimum values for the ratio G are proposed here; engineers may wish to establish such limiting values on a project basis.

LeMessurier presents an equation for a second-order drift ratio (rather than for a displacement amplifier) in Equation 31. In the terms used here, that equation is:

$$\frac{\Delta_2}{L} = \frac{H}{\dfrac{HL}{\Delta_1} - P_{story} - C_L P_{mf}} \tag{14}$$

Following Griffis and White (2013), the displacement amplifier can be determined by combining Equations 5 and 14:

$$D_{AF} = \frac{1}{1 - \dfrac{\Delta_1 (P_{story} + C_L P_{mf})}{HL}} \tag{15}$$

When P_{mf} is zero (such as for a building without moment frames or with negligible axial load on the moment-frame columns), R_M is 1.0, and both amplifiers (F_{AF} and D_{AF}) simplify and become equal. Thus, the amplifier B_2 represents both force and displacement amplification if $R_M = 1.0$:

$$B_2 = \frac{1}{1 - \dfrac{P_{story}\Delta_1}{HL}} \text{ if } R_M = 1.0 \tag{16}$$

The Refined R_M Approach

Combining Equations 7, 10, and 15 gives an expression for R_M consistent with the amplifiers based on LeMessurier:

$$R_M = 1 - \frac{P_{mf}\Delta_1}{HL} C_L \tag{17}$$

Thus, the system stiffness-reduction effect of P-δ on P-Δ represented by R_M is a function of the first-order lateral stiffness (H/Δ_1). For systems with high lateral stiffness, the P-δ effect on P-Δ may be quite small.

Stability-Coefficient-Based Second-Order Amplifiers

The refined formulation of R_M (Equation 17) can be presented as a function of the stability coefficient θ [defined in ASCE/SEI 7 (2016)], which is often used as a measure of second-order effects. The ASCE 7 equation can be presented in terms consistent with those in this paper:

$$\theta = \frac{P_{story}\Delta_1}{HL} \tag{18}$$

where

θ = stability coefficient per ASCE/SEI 7, Section 12.8.7, Equation 12.8-16

Thus

$$R_M = 1 - \theta \frac{C_L P_{mf}}{P_{story}} \tag{19}$$

Incorporating Equation 18, Equations 10 and 15 can be expressed as functions of θ:

$$B_2 = 1 + \frac{1}{\frac{1}{\theta} - \left(1 + \frac{C_L P_{mf}}{P_{story}}\right)} \tag{20}$$

$$D_{AF} = \frac{1}{1 - \theta\left(1 + \frac{C_L P_{mf}}{P_{story}}\right)} \tag{21}$$

Table 1 presents values of force amplifiers (B_2), displacement amplifiers (D_{AF}), and coefficients R_M for a range of stability coefficient θ. Force amplifiers B_2 and coefficients R_M are computed using both AISC *Specification* equations (Equations 1 and 9) and the explicit equations presented in this paper (Equations 20 and 17) based on P_{mf}/P_{story} = 0.333 and 1.0. The displacement amplifiers (D_{AF}) are also based on those values of P_{mf}/P_{story} and use Equation 21. For comparison, values of the amplifier B_2 for $P_{mf} = 0$ (Equation 16) are also presented. Values in Table 1 are calculated utilizing the maximum value of C_L per Equation 13; this simplification allows their general use as the worst case but overestimates the P-δ effect for real buildings with nonrigid beams.

The AISC *Specification* B_2 is conservative for force amplification but is unconservative if used for drift amplification. The range between the explicitly calculated force and displacement amplifiers is very small for $\theta \le 0.25$. The *Specification* B_2 overestimates the force by 5% or less and could be used as an approximate amplifier for drift, underestimating that effect by no more than 2% in that range. Because the explicit values of R_M using Equation 17 are very close to 1.0 for the range of typical building practice ($B_2 \le 1.5$), the simplification of using B_2 (with the *Specification* value of R_M) as the displacement amplifier will result in less error than using the *Specification* value for R_M in Equation 6. Use of R_M from Equation 17 with Equations 1 and 5 will produce force and drift results closer to an explicit second-order analysis than will use of the *Specification* B_2.

The discrepancy between the AISC *Specification* and explicit amplifiers B_2 increases at larger values of the stability coefficient, and at very large values the explicit force amplifier B_2 (Equation 20) exceeds the *Specification* B_2 (Equation 1) using the *Specification* R_M (Equation 9). The *Specification* R_M matches the explicit R_M (Equation 17) at $\theta = 0.70$, for which B_2 ranges from 3.3 (for $P_{mf}/P_{story} = 0.0$) to 5.7 (for $P_{mf}/P_{story} = 1.0$). Such high second-order effects are not expected in practical building designs. ($B_2 \ge 5.0$, combined with stiffness reduction due to inelasticity, results in instability.) As such, the *Specification* equations produce a reliable upper bound for force amplification on real structures.

According to AISC *Specification* Section C2.1(b), P-δ effects on P-Δ can be ignored for systems meeting certain conditions. Among these conditions are that $P_{mf}/P_{story} \le 1/3$, and $\Delta_2/\Delta_1 \le 1.7$ (using the reduced stiffness of the Direct Analysis Method, which corresponds to 1.5 for a full-stiffness analysis). That range is shaded in Table 1. (The stability coefficient θ corresponds to a first-order analysis with unreduced stiffness.) The values in Table 1 confirm that negligible error in force amplification is expected in that range as a result of using $R_M = 1.0$.

In Table 1, a line is drawn beneath values of $\theta = 0.25$, which is the limit for this coefficient for seismic design in ASCE/SEI 7, Section 12.8.7 (ASCE, 2016). Within that range the smallest value of R_M is 0.95. Thus, for seismic design, the value of R_M could be determined using a value of 0.05 (or lower) in lieu of 0.15 in Equation 9, providing for greater economy. Similar revisions of Equation 9 are possible for other bounds on the design space, such as limiting B_2 or limiting P_{mf}/P_{story}.

SECOND-ORDER STIFFNESS REDUCTIONS

The refined definition or R_M in Equation 17 serves not only as the basis of more accurate force and displacement amplifiers; it also facilitates a more accurate expression of the

Table 1. Amplifiers and RM Values											
	$P_{mf} = 0$	$P_{mf} = 0.333\ P_{story}$					$P_{mf} = 1.00\ P_{story}$				
	Both	AISC *Specification*		Explicit			AISC *Specification*		Explicit		
	B_2	R_M	B_2	R_M	$B_2 = F_{AF}$	D_{AF}	R_M	B_2	R_M	$B_2 = F_{AF}$	D_{AF}
θ	EQ 16	EQ 9	EQ 1	EQ 19	EQ 20	EQ 21	EQ 9	EQ 1	EQ 19	EQ 20	EQ 21
0.05	1.05	0.95	1.06	1.00	1.05	1.06	0.85	1.06	0.99	1.05	1.06
0.10	1.11	0.95	1.12	0.99	1.11	1.12	0.85	1.13	0.98	1.11	1.14
0.15	1.18	0.95	1.19	0.99	1.18	1.19	0.85	1.21	0.97	1.18	1.22
0.20	1.25	0.95	1.27	0.99	1.25	1.27	0.85	1.31	0.96	1.26	1.32
0.25	1.33	0.95	1.36	0.98	1.34	1.37	0.85	1.42	0.95	1.36	1.44
0.30	1.43	0.95	1.46	0.98	1.44	1.47	0.85	1.55	0.94	1.47	1.57
0.35	1.54	0.95	1.58	0.97	1.56	1.60	0.85	1.70	0.92	1.61	1.74
0.40	1.67	0.95	1.73	0.97	1.70	1.75	0.85	1.89	0.91	1.78	1.95
0.45	1.82	0.95	1.90	0.97	1.87	1.93	0.85	2.13	0.90	1.99	2.21
0.50	2.00	0.95	2.11	0.96	2.08	2.16	0.85	2.43	0.89	2.28	2.55
0.60	2.50	0.95	2.71	0.96	2.68	2.80	0.85	3.40	0.87	3.22	3.70
0.70	3.33	0.95	3.80	0.95	3.80	4.01	0.85	5.67	0.85	5.70	6.72
0.80	5.00	0.95	6.33	0.94	6.62	7.02	0.85	17.00	0.83	30.2	36.6

P-δ effect and its role in the construction of the second-order stiffness.

Internal Second-Order Stiffness

Combining Equations 1 and 2 gives the following stiffness relationship:

$$\frac{H}{\Delta_2} = R_M \frac{H}{\Delta_1} - \frac{P_{story}}{L} \tag{22}$$

The three major terms in this equation may be considered to represent important system properties:

$\frac{H}{\Delta_2}$ = second-order stiffness, kip/in. (N/mm)

$\frac{H}{\Delta_1}$ = first-order stiffness, kip/in. (N/mm)

$\frac{P_{story}}{L}$ = *P*-Δ stiffness reduction, kip/in. (N/mm)

This *P*-Δ stiffness reduction is given the symbol $K_{P\Delta}$:

$$K_{P\Delta} = \frac{P_{story}}{L} \tag{23}$$

Equation 22 also includes the "internal second-order stiffness," the reduced lateral stiffness due to the *P*-δ effect of axial force on moment-frame columns (P_{mf}):

$R_M \frac{H}{\Delta_1}$ = internal second-order stiffness, kip/in. (N/mm)

This internal second-order stiffness corresponds to the internal force B_2H and the displacement Δ_2, as can be seen by combining Equation 8 with the definition above:

$$R_M \frac{H}{\Delta_1} = \frac{B_2 H}{\Delta_2} \tag{24}$$

Stiffness Equations Using *P*-Δ and *P*-δ Stiffness Reductions

The presence of the R_M term in Equation 22 appears to complicate the relationships between the first-order, second-order, and *P*-Δ stiffnesses. However, Equation 17 can be used to simplify the relationship. Applying the formulation of R_M from Equation 17 to the internal second-order stiffness results in:

$$R_M \frac{H}{\Delta_1} = \frac{H}{\Delta_1} - \frac{C_L P_{mf}}{L} \tag{25}$$

This last term is the stiffness-reduction effect of *P*-δ on the system, not including the *P*-Δ effect. It is termed the "*P*-δ stiffness reduction" and is given the symbol $K_{P\delta}$:

$$K_{P\delta} = \frac{C_L P_{mf}}{L} \tag{26}$$

Thus, the effect of P-δ on the system is not a multiplier on the first-order stiffness (as could be inferred from Equation 22). Instead, it can be described as a subtraction. The stiffness-sensitive formulation of R_M in Equation 17 simply reflects the fact that the importance of the reduction depends on its magnitude relative to the first-order stiffness.

The force and displacement amplifiers in Equations 10 and 15 can be presented in terms of first-order stiffness and the P-Δ, and P-δ stiffness reductions:

$$B_2 = \frac{H/\Delta_1 - K_{P\delta}}{H/\Delta_1 - (K_{P\Delta} + K_{P\delta})} \tag{27}$$

$$D_{AF} = \frac{1}{1 - \dfrac{K_{P\Delta} + K_{P\delta}}{H/\Delta_1}} \tag{28}$$

Combining Equations 22, 23, and 25 gives the external second-order stiffness:

$$\frac{H}{\Delta_2} = \frac{H}{\Delta_1} - (K_{P\Delta} + K_{P\delta}) \tag{29}$$

Equation 29 can be understood as signifying that the external stiffness in the presence of gravity loads is less than first-order stiffness due to the P-Δ and the P-δ stiffness reductions. Equation 29 can also be presented as:

$$\frac{H}{\Delta_1} = \frac{H}{\Delta_2} + K_{P\Delta} + K_{P\delta} \tag{30}$$

In this format, the equation signifies that the required first-order stiffness is the required external stiffness plus the P-Δ and the P-δ stiffness (applied as an addition, rather than as a reduction). This latter form has two important corollaries. First, if an engineer is designing a building to meet a drift limit, the magnitude of the gravity loads and their effect on the system stiffness requires a stiffer lateral system. Second, the required first-order stiffness may be determined in advance of design and analysis based on the drift limit, the geometry, and the external loading. Such a process is illustrated in Sabelli et al. (in review). This simple relationship also facilitates the use of hand methods to validate the results of computer analysis.

Note that the P-δ the stiffness reduction ($K_{P\delta}$) not only adds to the first-order stiffness required to meet a (second-order) drift limit in Equation 30. It also reduces the external stiffness (Equation 29) and thus increases the second-order drift Δ_2, indirectly contributing to the additional strength required by $K_{P\Delta}\Delta_2$ to resist the external force H.

As formulated in Equations 29 and 30, the first-order, second-order, P-Δ, and P-δ stiffness have a simple arithmetic relationship, which is diagrammed in Figure 2. The stiffnesses that correspond to the forces at the second-order drift Δ_2 are those in Equation 22: the external stiffness, which corresponds to the applied load H; the internal second-order stiffness, which corresponds to the total load effect B_2H; and the P-Δ stiffness reduction, which corresponds to the difference between the two. The first-order stiffness by definition corresponds to the first-order displacement Δ_1 resulting from the lateral load H. The other stiffnesses (the P-δ and total second-order stiffness reductions) are relevant in constructing the external stiffness but do not correspond directly to the load effect on the system.

As can be seen in Figure 2, the drift amplification from Δ_1 to Δ_2 does not produce a total load effect on the first-order stiffness line. Instead, the total load effect is somewhat less, falling on the internal second-order stiffness line. Thus, the drift amplifier is greater than the force amplifier when $K_{P\delta} > 0$ (and thus $R_M < 1.0$), consistent with Equation 6.

SUMMARY AND CONCLUSIONS

This paper presents the background for the AISC *Specification* factor R_M based on original work by LeMessurier (1977). It also presents a refined expression for R_M in Equation 17, which can be used to reduce conservatism resulting from simplifications in the AISC *Specification* (2016b) formulation of this quantity. The paper also presents the corresponding equation for B_2 in Equation 10; this is more accurate than the use of the *Specification* equation for R_M. A corresponding displacement amplifier (D_{AF}, presented in Equation 15) can be used to estimate second-order drift Δ_2 from the first-order drifts Δ_1. The refined formulation of R_M is used to present a clear relationship between the first-order, second-order, P-Δ, and P-δ stiffnesses.

The methods presented herein may be used by practicing engineers to reduce conservatism in design and to critically evaluate the results of computerized second-order analysis. The relationships developed may be beneficial to those learning the amplifier method and second-order effects more generally.

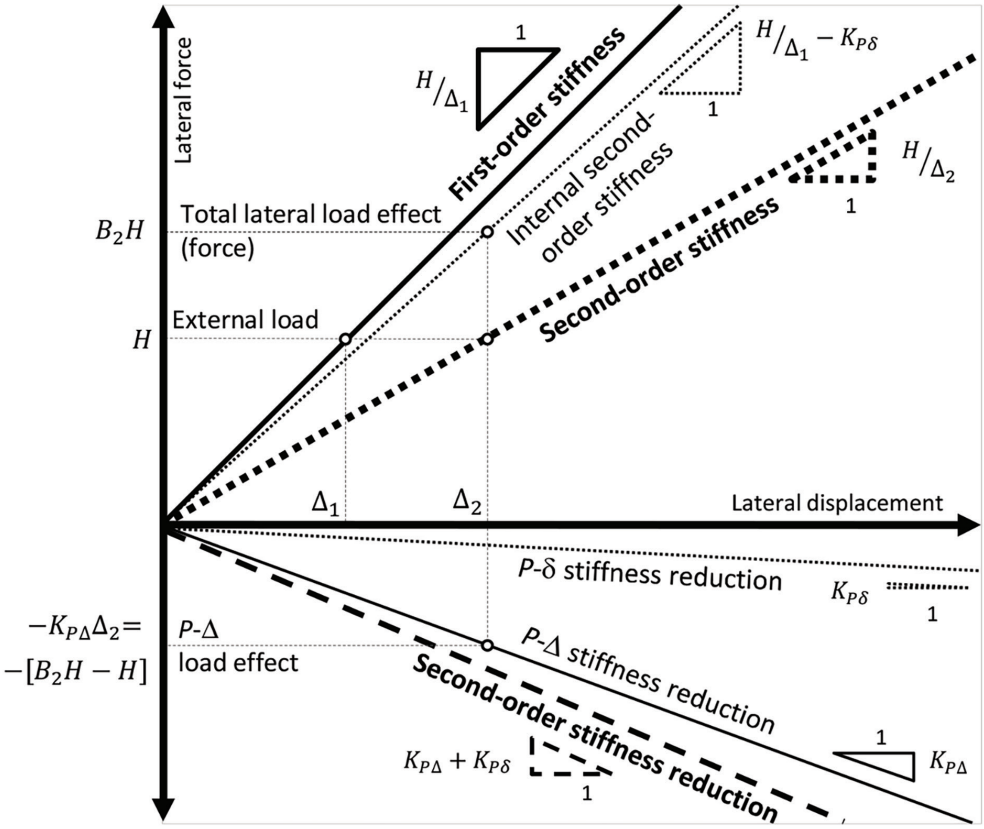

Fig. 2. First-order and second-order stiffness diagram.

REFERENCES

AISC (2016a), *Seismic Provisions for Structural Steel Buildings*, ANSI/AISC 341-16, American Institute of Steel Construction, Chicago, Ill.

AISC (2016b), *Specification for Structural Steel Buildings*, ANSI/AISC 360-16, American Institute of Steel Construction, Chicago, Ill.

ASCE (2016), *Minimum Design Loads and Associated Criteria for Buildings and Other Structures*, ASCE/SEI 7-16, American Society of Civil Engineers, Reston, Va.

Cheong-Siat-Moy, F. (1976), "Stiffness Design of Unbraced Steel Frames," *Engineering Journal*, AISC, Vol. 13, pp. 8–10.

Griffis, L.G. and White, D.W. (2013), *Stability Design of Steel Buildings*, Design Guide 28, AISC, Chicago, Ill.

LeMessurier, William J. (1977), "A Practical Method of Second Order Analysis: Part 2—Rigid Frames," *Engineering Journal*, AISC, Vol. 14, No. 2, pp. 49–67.

Sabelli, R., Griffis, L.G., and Geschwindner, L.F. (in press), "Determination of Second-Order Effects and Design for Stability Using the Drift Limit," *Engineering Journal*, AISC.

Steel Structures Research Update

Seismic Performance of Nonorthogonal Special Moment Frame Beam-to-Column Connections

JUDY LIU

INTRODUCTION

Ongoing research on the seismic behavior of nonorthogonal special moment frame beam-to-column connections is highlighted. Featured is a comprehensive experimental and computational study under way at the University of Arkansas and led by Dr. Gary Prinz, Associate Professor in Structural Engineering. The research team includes PhD students Hossein Kashefizadeh and Damaso Dominguez. Dr. Prinz's research interests include mechanics and simulation of ductile fracture, seismic design solutions for steel structures, and computer simulation of structures under dynamic loading. He received a National Science Foundation Faculty Early Career Development (CAREER) award to investigate a new micromechanics-based approach to ductile fracture simulation in additively manufactured steels for improved seismic structural fuse design. Dr. Prinz has also been awarded AISC's Milek Fellowship. The four-year Milek Fellowship is supporting this research on the seismic performance of skewed special moment frame (SMF) connections. The research team is partway through the third year of the four-year study. Selected results from the computational parametric study are highlighted along with a preview of the experimental investigation.

BACKGROUND AND MOTIVATION

Architectural flexibility and knowledge gaps for the seismic behavior of skewed SMF connections motivate this study. The architectural form and building envelope geometry of an SMF building might require a beam-to-column connection with a lateral beam skew angle, θ, as shown in Figure 1. However, only orthogonal configurations ($\theta = 0°$) are included in the AISC *Prequalified Connections for Special and Intermediate Steel Moment Frames for Seismic Applications* provisions (AISC, 2020). This limitation would preclude placement of an SMF connection such as a reduced beam section (RBS) or welded unreinforced flange–welded web (WUF-W) at such a location. Furthermore, research on skewed SMF connections under cyclic loading is limited and has not considered the influence of the composite floor slab. This research seeks to develop new knowledge and guidelines to improve architectural flexibility in SMF buildings.

Prior nonorthogonal SMF research focused on effects of skew angle and column axial load on the seismic performance of bare-steel RBS connections. The numerical investigations demonstrated adequate flexural capacity. Up to a 20° skew angle, increases in column twist and column flange yielding were minimal (Prinz and Richards, 2016; Desrochers et al., 2018). At a 30° skew angle, the torsional demands and yielding effects were more pronounced. The AISC *Prequalified Connection* Commentary cites Prinz and Richards (2016) with the acknowledgment that seismic performance of RBS connections with low skew angles (e.g., less than 5° to 10°) might be acceptable (AISC, 2020).

Prior studies on orthogonal SMF beam-to-column connections with composite slabs provided relevant results while highlighting potential issues for the behavior of nonorthogonal SMF connections. Increased moment capacity and delayed connection strength degradation under cyclic loading were observed for RBS connections with slabs (Zhang et al., 2004; Zhang and Ricles, 2006). Jones et al. (2002) demonstrated that the slab effects were more pronounced for shallow beam sections than for relatively deep beam sections. Dominguez and Prinz (2020) observed from the literature that for "skewed connections, increases in beam flexural strength through the addition of a concrete slab may have negative consequences, as increased beam-flange forces transmitted to the column may result in

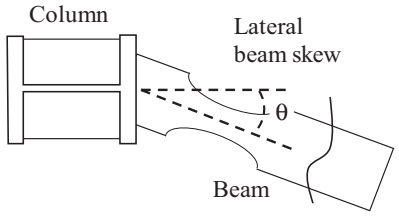

Fig. 1. Skewed reduced beam section (RBS) connection.

Judy Liu, PhD, Research Editor of the AISC Engineering Journal, Professor, Oregon State University, School of Civil and Construction Engineering, Corvallis, Ore. Email: judy.liu@oregonstate.edu

increased column twisting due to eccentricities between the beam-line and column centroid created by the skew."

RESEARCH OBJECTIVES AND PLAN

Building upon prior work on bare-steel skewed SMF connections and orthogonal connections with composite slabs, the primary research objectives are (1) to characterize the cyclic behavior of skewed SMF connections with composite slabs and (2) to develop comprehensive seismic design guidelines for skewed SMF connections. The research scope includes reduced beam section (RBS) and welded unreinforced flange–welded web (WUF-W) connections. Specifically, the research team is exploring "the effectiveness of RBS and WUF-W design procedures for limiting fractures near the beam-column connection welds of skewed SMF connections, as well as composite frame slab effects and the effects from column axial loads on column twisting/yielding." (Dominguez et al., 2020)

The team is achieving these research objectives through an integrated analytical-experimental investigation. Advanced finite element modeling is used for a parametric investigation into skewed SMF connection response to cyclic loading, as well as analyses to evaluate susceptibility to low-cycle fracture and dynamic system-level performance. Composite connection behavior is explored through the analytical parametric study. Experiments will include cyclic testing of bare-steel, skewed SMF connections, and detailed fracture investigations. The fracture investigations following testing will include nondestructive inspections within the beam-to-column weld regions (die penetrant, magnetic particle testing) to identify potential brittle fracture issues. Additionally, destructive weld-region sectioning and metallographic investigations will help identify crack formations (if any) within the beam-to-column weld regions.

ANALYTICAL INVESTIGATION

The comprehensive analytical investigation includes evaluation of skewed SMF connection response to cyclic loading, susceptibility to low-cycle fracture, and dynamic system-level performance. A six-story earthquake time-history simulation has been used to study system-level performance. For cyclic behavior of skewed SMF connections, the analysis matrix includes 64 double-sided RBS prequalification-type simulations, 48 double-sided WUF-W simulations, and 12 RBS connection with composite slab simulations. The low-cycle fracture susceptibility of the RBS and beam-to-column weld regions is being investigated with 124 submodels. Some results from the parametric study are highlighted.

Parametric Study

An in-depth computational investigation explored the behavior of skewed SMF connections with and without a composite slab. A three-story SMF subassembly was modeled with appropriate boundary conditions to capture the behavior at the middle pair of SMF connections (Figure 2). RBS and WUF-W connections were investigated, along with shallow, medium, and deep column configurations and beam-column skews ranging from 10° to 30° (Table 1). Column axial loads of 0, 10, 25, and 50% of the design compressive strength were considered. The different axial loads were investigated to isolate the effect of column axial load on column flange yielding because increased column twist resulting in column-flange yielding was observed in early analyses. Results for 12 composite models were compared to those for nine bare-steel RBS models. Three of the 12 composite models used a higher compressive strength. Additional details can be found in Dominguez and Prinz (2020).

Modeling Approach, Loading, and Validation

The modeling of the steel and concrete components, boundary conditions, and loading provided realistic representation of the cyclic behavior of skewed SMF connections subjected to cyclic loading. Shell elements used for the steel sections captured local buckling and aided local connection stress and strain measurements. The floor slabs, modeled with solid elements and embedded truss elements for the reinforcing bars, utilized the existing concrete cracking constitutive models in ABAQUS (HKS, 2014). Shear studs were modeled using embedded beam elements. As shown in Figure 2, a three-story frame assembly was modeled to focus on the behavior of the middle-story connection. Dominguez and Prinz (2020) explain that this was done "in order to simulate realistic torsional boundary conditions within the columns of the skewed frame geometries" and to remove the connections of interest from boundary support effects. Figure 3 shows the cyclic loading protocol as specified by the AISC *Seismic Provisions* for SMF connection prequalification (AISC, 2016). The cyclic loading was applied as displacements at the beam ends in the model, which represented the beam mid-span inflection points in an SMF. The modeling approach was validated against cyclic tests of RBS connections (Jones et al., 2002). Additional details can be found in Dominguez and Prinz (2020).

Table 1. Beam, Column, and Connection Configurations for Parametric Study						
No. of Models	**Connection**	**Column Section**	**Beam Section**	**Beam Skew Angles (degrees)**	**Column Axial Load (% capacity)**	**Concrete* Compressive Strength (ksi)**
10	RBS	W14×193	W24×76	0, 10, 20, 30	0–50	4, 6
4	RBS	W18×143	W24×76	0, 10, 20, 30	0–50	Not applicable
7	RBS	W24×131	W24×76	0, 10, 20, 30	0–50	4
7	RBS	W33×291	W36×150	0, 10, 20, 30	0–50	4
4	WUF-W	W14×257	W24×76	0, 10, 20, 30	0–50	Not applicable
4	WUF-W	W24×162	W24×76	0, 10, 20, 30	0–50	Not applicable
4	WUF-W	W33×354	W36×150	0, 10, 20, 30	0–50	Not applicable
* For 10°, 20°, and 30° skew angle models only.						

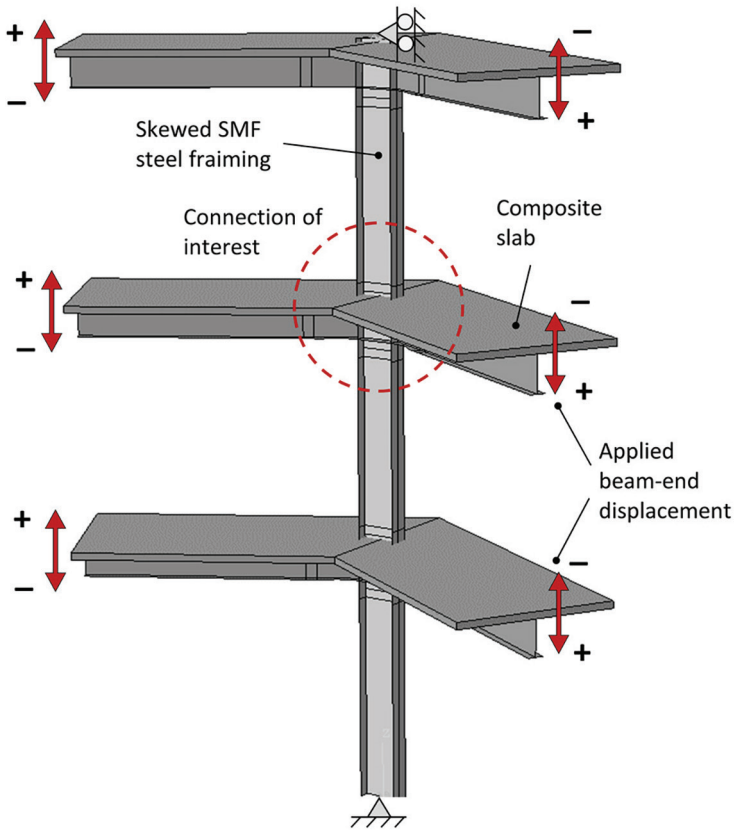

Fig. 2. SMF subassembly for parametric study.

Effects of the Composite Floor Slab

Results from the parametric study included insights into the effects of the concrete slab on moment capacity and column twist. Figure 4 compares moment-rotation responses for bare-steel and composite sections at 10° and 30° skew for shallow (W14×193) and deep (W33×291) columns. The presence of the composite slab did not result in any discernable increase in the connection negative moment capacity. A limited increase was observed for the positive moment capacity when the concrete slab was in compression. More significant was the delay in the post-peak degradation for the composite sections. Dominguez and Prinz (2020) observed that the "improved moment degradation behavior under the positive moment cycles is likely due to increased confinement of the beam top-flange delaying the onset of flange local buckling." For both bare-steel and composite sections, loss of moment capacity occurred more rapidly with an increase in skew angle. However, all connections satisfied the criterion of at least 0.04 radian of drift before 20% reduction in plastic moment capacity (AISC, 2016). Meanwhile, the composite slab reduced column twist until large skews; an increase in column twist was observed at 30° skew. The increase was attributed to the larger flexural demands from the beam combined with the larger eccentricity between the beam-line and the column centroid. Additional details and results, include the effect of the composite floor slab on connection plastic strain demands, can be found in Dominguez and Prinz (2020).

FUTURE WORK

Future work includes the experimental investigation and development of seismic design guidelines for skewed SMF connections. A total of 12 connection assemblies will be experimentally tested, providing a comprehensive data set for estimating demands in skewed RBS moment connections during cyclic loading. These 12 connection assemblies represent skewed geometries at three different angles (10°, 20°, and 30°) and two column depths (typical W14× column sections and deeper W18× column sections) with replicates for each (Table 2). The two column sections will be used to explore web depth effects on column twisting and flange-tip yielding. All test specimens will use a W24×76 beam, which has a flange width-thickness ratio that narrowly satisfies compactness requirements. The columns for the one-sided connection assemblies will be supported at each end (Figure 5), the beams will be laterally braced, and the cyclic loading protocol will be applied at the beam end (Figure 6).

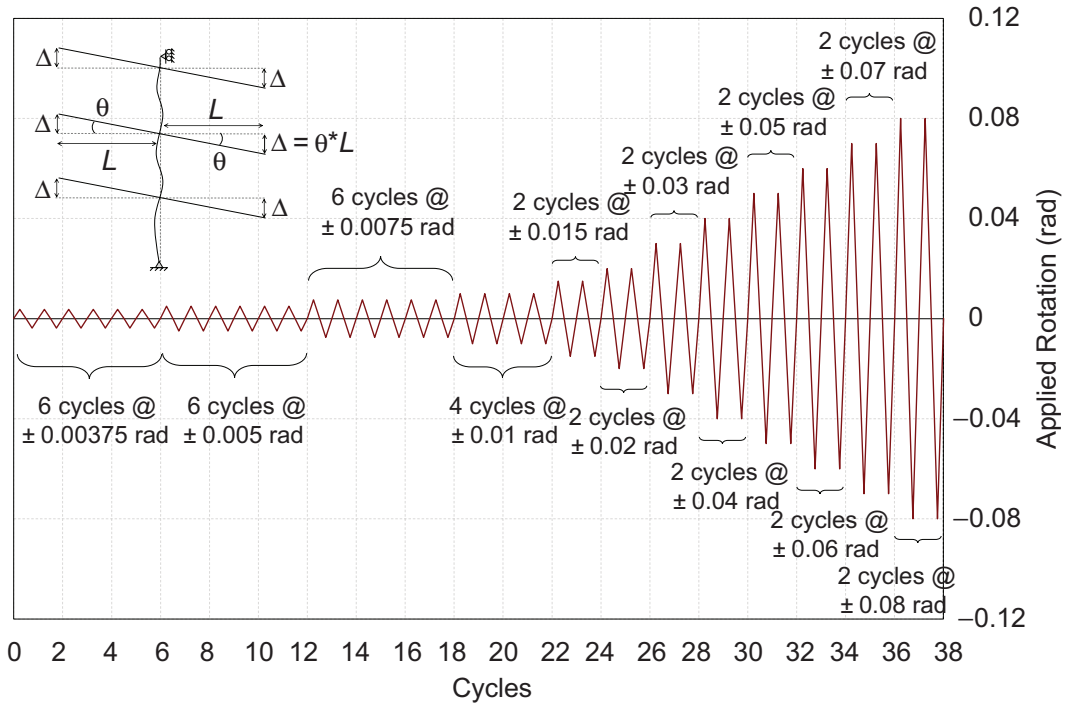

Fig. 3. Cyclic loading protocol for parametric study.

Table 2. Experimental Test Matrix				
Test No.	**Test ID**	**Skew (degrees)**	**Column Section**	**Beam Section**
½	SC-1	10	W14×132	W24×76
¾	SC-2	20	W14×132	W24×76
5⁄6	SC-3	30	W14×132	W24×76
7⁄8	DC-1	10	W18×86	W24×76
9⁄10	DC-2	20	W18×86	W24×76
11⁄12	DC-3	30	W18×86	W24×76

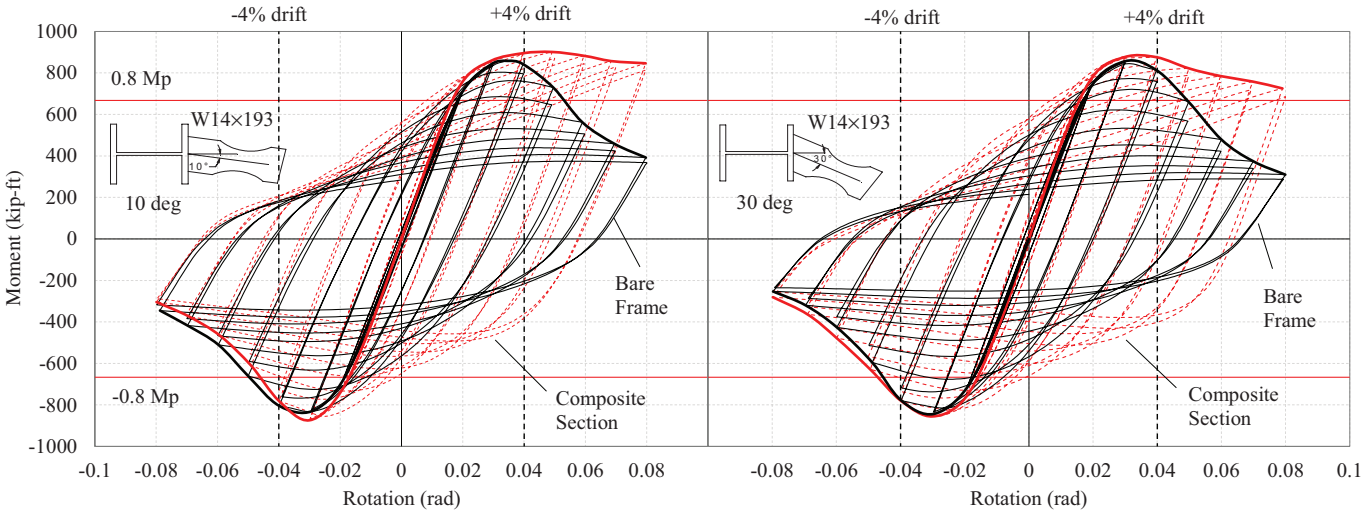

(a) shallow columns

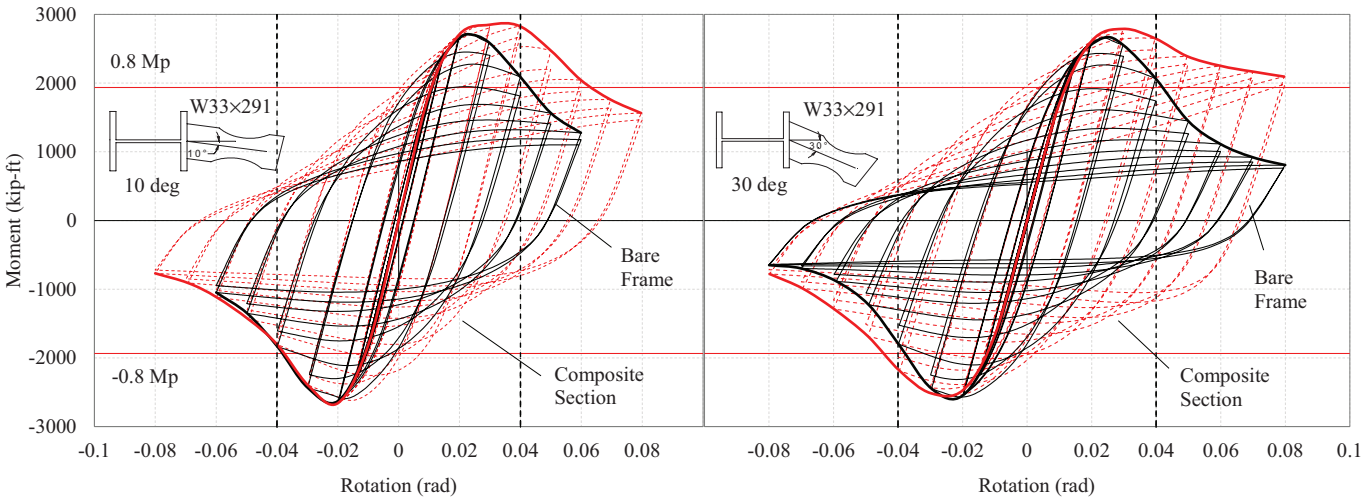

(b) deep columns

Fig. 4. Moment-rotation response for bare-steel and composite sections at 10° and 30° skew.

Fig. 5. Specimen in test frame.

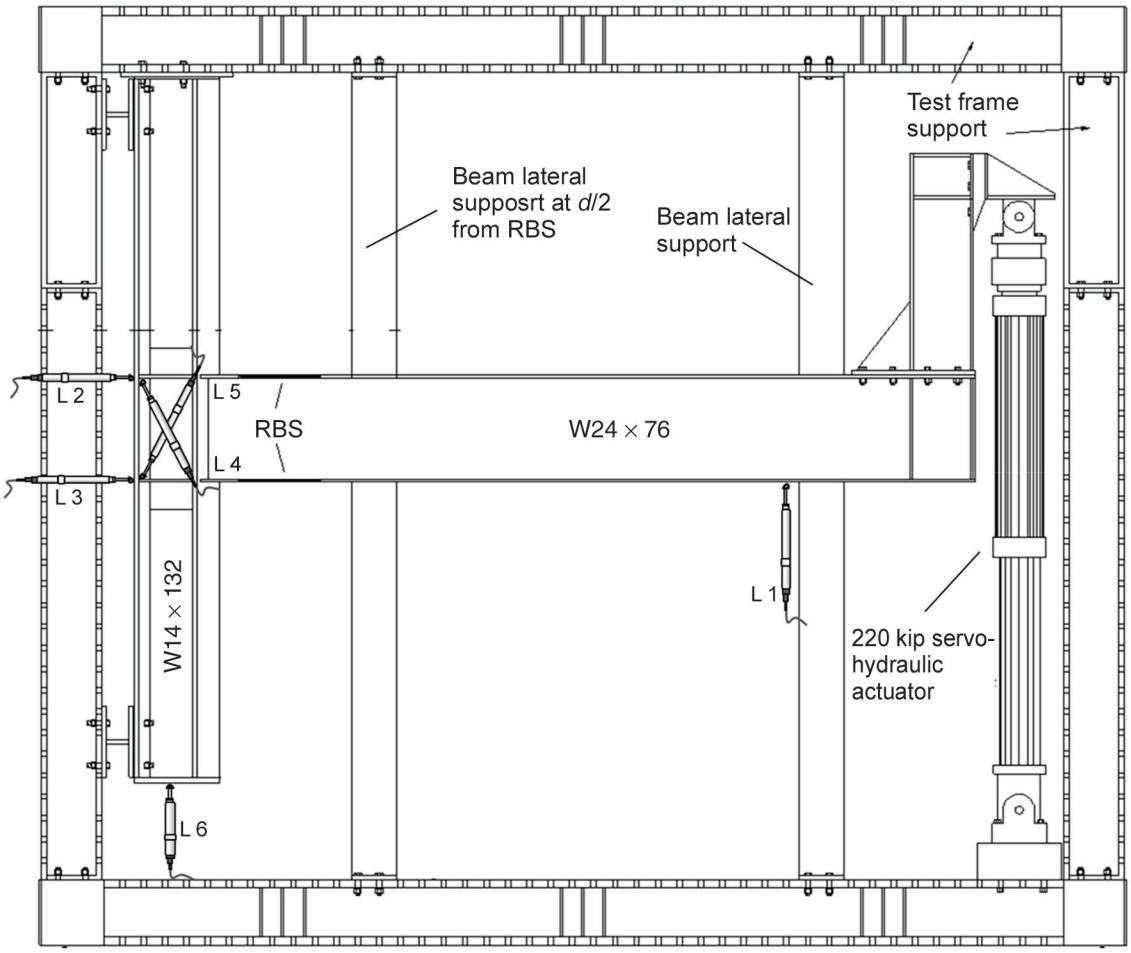

Fig. 6. Schematic of experimental setup.

ACKNOWLEDGMENTS

Thank you to Dr. Gary Prinz for his many contributions to this article. The work of PhD students Hossein Kashefizadeh and Damaso Dominguez is also recognized. The research is sponsored by the American Institute of Steel Construction (AISC); Tom Schlafly and Devin Huber have served as project managers. The researchers would like to thank AISC Research Oversight Committee members Tom Kuznik (Herrick Steel), Tom Sabol (Engelkirk), and Chia-Ming Uang (UCSD). Any findings or recommendations are those of the researchers and do not necessarily reflect the views of the sponsor.

REFERENCES

AISC (2016), *Seismic Provisions for Structural Steel Buildings*, ANSI/AISC 341-16, American Institute of Steel Construction, Chicago, Ill.

AISC (2020), *Prequalified Connections for Special and Intermediate Steel Moment Frames for Seismic Applications*, including Supplement No. 2, ANSI/AISC 358s2-20, Chicago, Ill.

Desrochers, C., Prinz, G.S., and Richards, P.W. (2018), "Column Axial Load Effects on the Performance of Skewed SMF RBS Connections," *Journal of Constructional Steel Research*, Vol. 150, pp. 505–513.

Dominguez, D., Kashefizadeh, M.-H., and Prinz, G.S. (2020), *Steel Seismic Systems with Architectural Flexibility: Seismic Performance of Non-Orthogonal SMF Beam-to-Column Connections*, Steel Structures Research Laboratory (SSRL), Department of Civil Engineering, University of Arkansas, March 2020, SSRL Interim Annual Report No. 2.

Dominguez, D. and Prinz, G.S. (2020), "Cyclic Behavior of Laterally Skewed Special Moment Frame Connections having Composite Concrete Slabs," *Steel Construction—Design and Research*, accepted for publication December 2020.

HKS (2014), "ABAQUS Standard Users Manual," Version 6.14. Hibbitt, Karlsson, and Sorensen, Inc.

Jones, S.L., Fry, G.T., and Engelhardt, M.D. (2002), "Experimental Evaluation of Cyclically Loaded Reduced Beam Section Moment Connections," *Journal of Structural Engineering,* Vol. 128, No. 4, pp. 441–451.

Prinz, G.S. and Richards, P.W. (2016), "Demands on Reduced Beam Section Connections with Out-of-Plane Skew," *Journal of Structural Engineering,* 10.1061/(ASCE)ST.1943-41X.0001360,04015095.

Zhang, X. and Ricles, J.M. (2006), "Seismic Behavior of Reduced Beam Section Moment Connections to Deep Columns," *Journal of Structural Engineering*, Vol. 132, No. 3, pp. 358–367.

Zhang, X., Ricles, J.M., Lu, L.W., and Fisher, J.W. (2004), "Analytical and Experimental Studies on Seismic Behavior of Deep Column-to-Beam Welded Reduced Beam Section Moment Connections," *Proceedings of the 13th World Conference on Earthquake Engineering,* Vancouver, B.C., Canada.